UNIL | Université de Lausanne

Unicentre
CH-1015 Lausanne
http://serval.unil.ch

Year : 2018

Molecular and Metabolic Characterization of Mitochondria Mediated Tumourigenesis in Prostate Cancer

Chen Jingjing

Chen Jingjing, 2018, Molecular and Metabolic Characterization of Mitochondria Mediated Tumourigenesis in Prostate Cancer

Originally published at : Thesis, University of Lausanne

Posted at the University of Lausanne Open Archive http://serval.unil.ch
Document URN : urn:nbn:ch:serval-BIB_E5396394C8843

Droits d'auteur
L'Université de Lausanne attire expressément l'attention des utilisateurs sur le fait que tous les documents publiés dans l'Archive SERVAL sont protégés par le droit d'auteur, conformément à la loi fédérale sur le droit d'auteur et les droits voisins (LDA). A ce titre, il est indispensable d'obtenir le consentement préalable de l'auteur et/ou de l'éditeur avant toute utilisation d'une oeuvre ou d'une partie d'une oeuvre ne relevant pas d'une utilisation à des fins personnelles au sens de la LDA (art. 19, al. 1 lettre a). A défaut, tout contrevenant s'expose aux sanctions prévues par cette loi. Nous déclinons toute responsabilité en la matière.

Copyright
The University of Lausanne expressly draws the attention of users to the fact that all documents published in the SERVAL Archive are protected by copyright in accordance with federal law on copyright and similar rights (LDA). Accordingly it is indispensable to obtain prior consent from the author and/or publisher before any use of a work or part of a work for purposes other than personal use within the meaning of LDA (art. 19, para. 1 letter a). Failure to do so will expose offenders to the sanctions laid down by this law. We accept no liability in this respect.

UNIL | Université de Lausanne
Faculté de biologie
et de médecine

Molecular and Metabolic Characterization of Mitochondria Mediated Tumourigenesis in Prostate Cancer

Thèse de doctorat ès sciences de la vie (PhD)

présentée à la

Faculté de biologie et de médecine
de l'Université de Lausanne

par

Jingjing Chen

Maître de la Science de Deuxième université médicale militaire, Shanghai

Jury

Prof. Hans Acha-Orbea, Président
Prof. Andrea Alimonti, Directeur de thèse
Prof. Elisa Oricchio, expert
Prof. Fabio Grassi, expert

Lausanne 2018

UNIL | Université de Lausanne
Faculté de biologie
et de médecine

Ecole Doctorale

Doctorat ès sciences de la vie

Imprimatur

Vu le rapport présenté par le jury d'examen, composé de

Président· e	Monsieur Prof. Hans **Acha-Orbea**
Directeur· rice de thèse	Monsieur Prof. Andrea **Alimonti**
Rapporteur· e	Monsieur Prof. Hans **Acha-Orbea**
Experts· es	Madame Prof. Elisa **Oricchio**
	Monsieur Dr Fabio **Grassi**

le Conseil de Faculté autorise l'impression de la thèse de

Monsieur Jingjing Chen

Master of Medical Science Second Military Medical University, Chine

intitulée

Molecular and metabolic characterization of mitochondria mediated tumourigenesis in prostate cancer

Lausanne, le 7 mars 2018

pour le Doyen
de la Faculté de biologie et de médecine

Prof. Hans Acha-Orbea

Acknowledgement

This work was completed under the intensive supports and guidance of PhD advisor Prof. Andrea Alimonti for giving me the opportunity to work on cancer metabolism in prostate cancers. I would like to thank my committee members: Prof. Hans Acha-Orbea, Prof. Fabio Grassi, Prof. Elisa Oricchio and Prof. Arkaitz Carracedo for their suggestion and support.

I also would like to thank my dear lab mates and colleagues: Ilaria Guccini, Diletta Di Mitri, Daniela Brina, Ajinkya Revandkar, Abdullah Alajati, Emiliano Pasquini, Sandra Pinton and Manuela Sarti for their valuable help and friendship. I enjoyed working with them and learned from every one of them. A huge thanks to a very special colleague and friend: Ms. Ornella Guerra for all the support and help.

I would like to thank my beloved family for their support, encouragement, endless love and belief in me.

Abstract

The mechanisms by which mitochondrial metabolism supports cancer anabolism are still unclear. Here, we unexpectedly find that genetic and pharmacological inactivation of Pyruvate Dehydrogenase A1 (PDHA1), a subunit of pyruvate dehydrogenase complex (PDC) inhibits prostate cancer development in different mouse and human xenograft tumour models by affecting lipid biosynthesis. Mechanistically, we show that in prostate cancer, PDC localizes in both mitochondria and nucleus. While nuclear PDC controls the expression of Sterol regulatory element-binding transcription factor (SREBF) target genes by mediating histone acetylation, mitochondrial PDC provides cytosolic citrate for lipid synthesis in a coordinated effort to sustain anabolism. In line with these evidence, we find that PDHA1 and the PDC activator, Pyruvate dehydrogenase phosphatase 1 (PDP1), are frequently amplified and overexpressed at both gene and protein level in prostate tumours. Taken together, these findings demonstrate that both mitochondrial and nuclear PDC sustain prostate tumourigenesis by controlling lipid biosynthesis thereby pointing at this complex as a novel target for cancer therapy.

Résumé

Les mécanismes associés à la fonction mitochondriale ont participé au métabolisme anabolique qui a causé le cancer sont encore peu clair. Nous avons découvert que l'inactivation de la pyruvate déshydrogénase A1 (PDHA1), une sous-unité du complexe pyruvate déshydrogénase (PDC), par des moyens génétiques et pharmacologiques, inhibe le développement du cancer de la prostate dans différents murins et humains de xénogreffe modèles. Cet effet est à la modulation de la biosynthèse des lipides. Le PDC est localisé dans la fois dans la mitochondrie et dans le noyau. Le PDC nucléaire contrôle l'expression de gènes cibles du facteur de transcription Sterol regulating element-binding (SREBF) en médiant l'acétylation des histones, tandis que le PDC mitochondrial fourni du citrate, un intermédiaire métabolique nécessaire à la biosynthèse des lipides. Ainsi, le PDC nucléaire et le PDC mitochondrial facilitent le métabolisme anabolique de façon coordonnée. De même, PDHA1 et activateur de PDC, pyruvate déshydrogénase phosphatase 1 (PDP1), sont fréquemment amplifiés et surexprimés au niveau génétique et protéique dans les tumeurs de la prostate. Dans l'ensemble, nos résultats démontrent que les complexes PDC nucléaires et mitochondriaux supportent le processus de tumorigenèse dans le cas du cancer de la prostate en promouvant la biosynthèse des lipides. Nos observations placent les complexes PDC comme une nouvelle cible thérapeutique pour le traitement du cancer.

List of Abbreviations

SRC SRC Proto-Oncogene, Non-Receptor Tyrosine Kinase
TCA cycle tricarboxylic acid cycle
NAD$^+$ β-Nicotinamide adenine dinucleotide
NADH β-Nicotinamide adenine dinucleotide, reduced
PDC pyruvate dehydrogenases complex
acetyl coA acetyl coenzyme A
MTS mitochondrial-targeting sequences
Pdha1 Pyruvate Dehydrogenase E1 Alpha 1 Subunit
PDPs Pyruvate dehydrogenase phosphatase
Pdks pyruvate dehydrogenase kinases
Dlat Dihydrolipoamide S-Acetyltransferase
Dld Dihydrolipoamide Dehydrogenase
MEF Mouse Embryonic Fibroblasts
AKT AKT Serine/Threonine Kinase
Vdac1 Voltage-dependent anion channel 1
ATP Adenosine triphosphate
SREBF Sterol responsive element binding factor
Acly ATP Citrate Lyase
Sqle Squalene Epoxidase
ACSS2 Acyl-coenzyme A synthetase short-chain family member 2
ChIP Chromatin immunoprecipitation
E2F1 E2F Transcription Factor 1
CCND1 Cyclin D1
NES nuclear export signal
NLS nuclear localization signal
3-FP 3-fluoropyruvate
NSCLC non-small lung cells cancer
Cer Ceramide
ChE Cholesteryl ester
DG Diradylglycerolipids
LPC lysophosphatidylcholine
LPE lysophosphatidylethanolamine
LPG lysylphosphatidylglycerol
LPI lysophosphatidylinositol
LPS lysophosphatidylserine
LdMeP lysodimethylphosphatidylethanolamine
MG Monoradylglycerolipids
OAHFA (O-acyl)-omega-hydroxy fatty acids
PA phosphatidic acid
PC phosphatidylcholine
PE phosphatidylethanolamine
PG Phosphatidylglycerol
PI phosphatidylinositol
PMe phosphomonoesters

PS phosphatidylserine
SM Sphingomyelin
TG Triglyceride
dMePE dimethylphosphatidylethanolamine
ATCC American Type Culture Collection
FBS fetal bovine serum
RIPA buffer Radioimmunoprecipitation assay buffer
GEP Gene expression profiling
GSEA Gene Set Enrichment Analysis
GEO Gene Expression Omnibus
FITC fluorescein isothiocyanate
ANOVA Analysis of variance
PLS-DA Partial Least Squares-Discriminant Analysis
VIP Variable Importance in Projection
MD molecular dynamics
TPP Thiamine pyrophosphate
GAFF general amber force field
SA Surface area

Contents

1. List of Figures

2. List of Tables

3. Introduction

3.1 Cancer metabolism

Cancer metabolism is one of the oldest fields of study in cancer biology, preceding the discovery of oncogenes and tumor suppressors by some 50 years. The initial observations by Otto Warburg and his contemporaries during the early twentieth century suggested that core cellular metabolism was skewed during the process of malignant transformation[1], however, the oncogene revolution since the discovery of the first oncogene, SRC (a proto-oncogene tyrosine-protein kinase)[2] and the emerge of genetic technology in the latter half of the century shifted the focus of research in cancer biology towards the specific mutations and alterations in signalling pathways responsible for tumorigenesis. Although it was initially thought that a set of mutations in specific oncogenes and tumour suppressors was sufficient to drive tumorigenesis, the spontaneous accumulation of such mutations in otherwise healthy tissue[3] indicates that cell transformation is a process beyond this initial simplistic view. It has been shown that during transformation cancer cells undergo profound metabolic changes, given the advent of a variety of techniques to assess the cellular metabolome, including activation of glycolysis, altered utilization of amino acids, and dysregulation of mitochondrial function[4]. The metabolic studies in cancer also revealed multiple mechanisms for tumorigenesis or cancer progression driven by environmental factors such as high-fat diet and bioavailability of certain nutrients[5-8]. Discoveries during the past two decades, and the successful clinical implementation of imaging approaches based on the metabolic phenotype of some tumours have once again highlighted that changes to metabolic processes are required for cells to escape from their defined roles as integrated parts of a tissue and organ system, and become an independent clone of cells that manifests itself as malignant disease.

The most common approach to investigating and understanding tumour metabolism has been focusing on a set of absolute requirements for cell survival and proliferation that malignant cells must satisfy in order to persist within their environment. These requirements can be described in several ways, but a common framework is to focus on three aspects: the generation of energy to fuel biochemical reactions; the generation of biochemical building blocks required for cell growth and division via biosynthetic pathways; and the maintenance of biochemical homeostasis, ensuring that conditions such as redox potential are maintained within a range that allows cellular biochemical processes to continue[9]. In order to develop into an aggressive malignant disease, tumour cells must fulfil these requirements, along with the other well-defined hallmarks of cancer[10]. Proliferating cells tend to express glucose transporters and glycolytic enzymes out of proportion to the machinery required to oxidize pyruvate[11], consistent with preferential conversion of glucose to lactate without loss of respiration. This distinction is important because intermediates generated by the tricarboxylic acid (TCA) cycle are precursors for lipids, amino acids, and nucleotides. These precursors complement precursor metabolites from glycolysis and other pathways and are necessary to support proliferation[12]. Fuels besides glucose also contribute to core metabolic functions of cancer cells: energy formation, biomass reassemble, and redox control. Glutamine is a prominent example[13]; however, recent work has revealed that a diversity of nutrients and pathways support these functions. The expanding metabolic repertoire of cancer cells has been reviewed extensively, with acetate and other fatty acids, lactate, branched chain amino acids, serine, and glycine representing some of the nutrients that are needed to fuel different cancers[14-15].

Pathways downstream of oncogenes and tumour suppressors regulate cancer cell metabolism. Genomic alterations can also result in copy-number gains and losses of genes encoding metabolic enzymes, and this may induce vulnerabilities[16-18]. However, the extent to which metabolic preferences are hard-wired by the tumour genotype is less clear because many non-genetic factors also influence tumour metabolism. As in all tissues, tumor metabolism is dictated by a variety of intrinsic and extrinsic factors. We need to understand how these factors are integrated to create metabolic dependencies. We were interested in studying PDC in prostate cancer because mitochondrial metabolism has been shown to be enhanced in certain types of tumours and certain stage of cancers to support tumour growth[19-21]. Cancer cells in culture have a different metabolic phenotype than tumours. Whereas many cancer cell lines quantitatively convert glucose to lactate, glucose oxidation is prevalent in tumours[19, 22-24]. Cultured lung cancer cells use glutamine to supply TCA cycle carbon, whereas lung tumours in mice prefer glucose as a TCA cycle fuel[22-23, 25]. These differences translate into altered vulnerabilities, as lung cancer cell lines require glutaminase for proliferation whereas tumors derived from these same cells do not; the converse is true for enzymes involved in glucose oxidation[22]. The environment can also affect the efficacy of drugs targeting metabolism. Metformin and other biguanides are mitochondrial complex I inhibitors that slow tumor growth by preventing complex I-mediated NAD^+ regeneration[26]. Thus, alternative NAD^+ regeneration pathways decrease complex I dependence and promote metformin resistance[27]. Lipid depletion potentiates the effect of acetyl-coA carboxylase inhibitors in culture, but the same drugs impair lung tumor growth *in vivo* despite the presumed availability of fatty acids[28]. Tumors vary in the fraction of actively proliferating cells, which influences metabolic dependency[29].

3.2 PDC and cancer

Changes in mitochondrial metabolism generally provide a growth advantage in an environment that support cell proliferation[19-23, 30-33]. Given that this metabolic reprogramming is tissue specific, cancer cells might need to activate different gene networks including well-characterized oncogenes and tumour suppressors or more recently determined oncogenic enzymes in metabolic pathways depending on their tissue of origin[34-36]. The pyruvate dehydrogenases complex (PDC) is gatekeeper protein complex that catalyses the conversion of acetyl coenzyme A (acetyl coA) thereby regulating the mitochondrial metabolism. Intriguingly, normal prostate epithelial cells exhibit a “truncated” TCA cycle due to inhibition of aconitase needed for the production and secretion of a high quantity of citrate into the seminal fluid[37-39]. In a series of experiments carried out by a member of our team, we found that PDHA1, a member of the PDC complex, is overexpressed in prostate cancer cells.

Mitochondria function as cellular energy generators, producing the fuel required to drive biological processes. The response of cells to mitochondrial activity or dysfunction regulates their survival, growth, proliferation, and differentiation. Several proteins that contain mitochondrial-targeting sequences (MTS) also reside in the nucleus and there is increasing evidence that the nuclear translocation of mitochondrial proteins represents a novel pathway by which mitochondria signal their status to the cell. The human pyruvate dehydrogenase complex (PDC) appears to translocate directly from the mitochondrial matrix to the nucleus[40]. This is supported by the observation that nuclear PDC components lack their MTS, implying prior processing in the mitochondrial matrix[40-41]. PDC links cytoplasmic glycolytic metabolism to mitochondrial oxidative phosphorylation by converting pyruvate to the tricarboxylic acid (TCA) cycle substrate acetyl co-enzyme A (-CoA)[42]. It performs the same enzymatic function in the nucleus, providing a pool of acetyl-CoA that is used as a cofactor for histone acetylation[40]. Nuclear PDC levels are cell cycle dependent and increase in response to growth signals or the inhibition of oxidative phosphorylation[40]. Therefore, PDC coordinates mitochondrial metabolism with nuclear gene expression to regulate cell growth.

Another theme that emerges from this focus is that the network of metabolic reactions, often considered separate from other cellular networks, is in fact closely integrated with key oncogenic signalling pathways, oncogenic mutational patterns and epigenetic regulators. Epigenetic reprogramming is a hallmark of many malignancies, and links between epigenetics and metabolism are emerging. Epigenetic alterations can affect the metabolic profile of tumour cells, and also how the appropriate flow of metabolites is required to make the epigenetic modifications so often observed in cancer[43]. Interestingly, changes in metabolism are frequently associated with epigenetic alterations through transcriptional or post-translational modifications, rather than irreversible genomic events. It is therefore possible that a specific metabolic landscape would enable epigenetic flexibility to control gene expression[40, 44-45].

In our study in prostate cancer, PDC localizes in both mitochondria and nucleus. Nuclear PDC functions in regulating histone acetylation specifically on the promoters of lipid synthesis genes and thus their expression and participation in lipid synthesis to support the cancer cell proliferation. This epigenetically promotion of the expression of lipid synthesis genes renders cancer cells aberrant lipid synthesis activity rather than that in normal prostate epithelial cells to support high-speed proliferation. This study demonstrates the role of mitochondrial and nuclear

PDH complex functions in regulating glucose influx of TCA cycle and controlling the diversion of TCA cycle intermediates. Contrast to classic 'Warburg effect' where cancers rely predominantly on glycolysis and catabolic TCA cycle gets restrained, tumours could achieve another 'anabolism oriented' reprogramming/axis by upregulating PDC and promoting PDC nuclear translocation. Nuclear PDC controls the transitory process in TCA cycle by allowing the short-lived entry and exit of carbon pool in mitochondria to fuel citrate synthesis and lipogenesis. Taking advantage of this diversion caused by nuclear PDC, the tumour cells reduce carbon consumption in TCA cycle thereby benefiting proliferation. PDC inactivation arrests nuclear PDC active cancers by abrogating both glucose influx and potential anaplerosis pathways from reductive carboxylation and glutaminolysis.

Cancer cells have to survive under adverse environment *in vivo* such as lacking sufficient availability of oxygen and nutrient because of their outrageous growth, which would compromise mitochondrial function[46-47]. This would be the *in vivo* driver for the cancer cells to develop extra mechanism by which mitochondrial enzymes such as PDC, translocate into nucleus regulate and change gene expression to make the cancer cells adaptive to hostile environment[40]. These facts revealed the mechanisms by which cancer cells become more additive to compartmentalized PDC activity and vulnerable to PDC inhibition than their normal counterparts. We find that PDC inhibition by genetic or pharmacological approach, affects specifically in lipogenesis pathways in these cells and therefore induces strong growth arrests in different mouse and human xenograft tumour models without inducing global adverse effects.

4. Results

4.1 *Pdha1* knockout induces tumour suppression in mice and human prostate tumours.

Mitochondrial metabolism is a source of energy and metabolic intermediates that serve various purposes, from redox homeostasis to anabolism or epigenetics[1]. There is an emerging association between increased mitochondrial metabolism and cancer pathogenesis and progression, but the molecular means underlying this biological process are still unknown[1-10]. The pyruvate dehydrogenase complex (PDC) is a gatekeeper multi-protein complex that catalyzes the conversion of pyruvate to acetyl coenzyme A (acetyl coA) thereby regulating the mitochondrial activity. This complex includes a major component, PDHA1, that can be dephosphorylated by the Pyruvate dehydrogenase phospatase (PDPs) Pdp1 and Pdp2 and phosphorylated by the pyruvate dehydrogenase kinases (Pdks)[11-13]. While dephosphorylation of PDHA1 activates the PDC, phosphorylation blocks its activity. In turn, we postulated that by impairing the function of PDHA1 and the PDC we would hamper mitochondrial metabolism and ascertain its consequences in prostate cancer biology.

We thus inactivated *Pdha1*, in *Pten*-null prostate conditional (*Pten*$^{pc-/-}$) mice that develop high-grade intra-epithelial prostate tumours at an early age and invasive prostate cancer at late age[14-16]. The presence of Cre recombinase, the recombination of the *Pten* exon 4 and 5 and *Pdha1* exon 8, in *Pten*$^{pc-/-}$; *Pdha1*$^{pc-/Y}$ prostates were verified by genotyping[14,17,18] (Supplementary Fig. 1a). Notably, *Pten*$^{pc-/-}$ mice develop tumours characterized by increased mRNA and/or protein levels of both Pdha1, Dlat, Dld and Pdp1, but not Pdp2 or Pdks, and an increased PDC activity as compared to normal prostates (Fig. 1a, b, Supplementary Fig. 1b and uncropped blots in Supplementary Fig. 12). Inactivation of *Pdha1* in *Pten*$^{pc-/-}$ tumours abrogated PDC activity and induced a strong growth inhibition in all the prostate glands of mice of different ages (Fig. 1c). This was associated with a strong reduction in cell proliferation as shown by the decreased Ki-67 staining and number of glands affected by invasive prostate cancer (Fig. 1d-f and Supplementary Fig. 1c). The strong arrest in proliferation in *Pten*$^{pc-/-}$; *Pdha1*$^{pc-/Y}$ tumours and *Pten*$^{-/-}$; *Pdha1*$^{-/Y}$ MEFs occurred independently of senescence[19] and apoptosis, that decreased when compared to controls (Supplementary Fig. 1d-i). Notably, *Pdha1* inactivation induced growth arrest exclusively in *Pten*$^{-/-}$ MEFs, without altering the growth of *Pten*^{wt} MEFs (Supplementary Fig. 1g). Moreover, *Pdha1* deletion in *Pten* null tumours and MEFs did not affect the levels of pAkt at Ser 473 and the total amount of mitochondria as indicated by the protein levels of Voltage-dependent anion channel 1 (Vdac1) [5] (Fig. 1a, Supplementary Fig. 1j and uncropped blots in Supplementary Fig. 13).

Next, we assessed the status of both *PDHA1* and *PDP1* in human prostate cancers. Bioinformatics analysis revealed that both PDHA1 and PDP1 are frequently amplified at the gene level and over-expressed in human prostate tumours. Interestingly, *PDP1* was found amplified (3/3 available datasets) and overexpressed (9/11 datasets) in primary prostate tumours when compared to normal prostate tissues whereas *PDHA1* was found amplified (2/3 datasets) and overexpressed (7/13 datasets) (Supplementary Fig. 2a-e) in metastatic when compared to primary tumours. We also stained PDHA1, phospho-PDHA1 and PDP1 on a tissue microarray (TMA) consisting of 128 prostate carcinoma and normal prostate samples. Immunohistochemistry analyses revealed that both PDHA1 and PDP1 are frequently over-expressed in human prostate tumours and their expression increases in tumours with high Gleason score (Supplementary Fig. 3a-c). On the contrary, phospho-PDHA1 staining was found upregulated only in a small portion of cases with a low Gleason score (Supplementary Fig. 3a,d). Interestingly the majority of cases having either high PDP1 or PDHA1 staining were negative for phospho-PDHA1 (Supplementary Fig. 3e). Three out of four prostate cancer cell lines exhibited increased PDC activity compared to non-transformed PNT2C2 prostate cells (Supplementary Fig. 3f). This was associated with increased protein levels of both PDHA1 and PDP1 and enhanced mitochondrial oxygen consumption dependent on both glucose and glutamine utilization (Supplementary Fig. 3f-i and uncropped blots in Supplementary Fig. 14). Taken together these data demonstrate that in prostate tumours and in cancer cell lines the PDC is active.

We next inactivated *PDHA1* in prostate cancer cells by means of different *PDHA1* shRNAs. In agreement with the results in the mouse model, we found that inactivation of PDC resulted in inhibition of cellular proliferation independently of apoptosis (Fig. 1g and Supplementary Fig. 3j,k and uncropped blots in Supplementary Fig. 12). We also detected, decreased mitochondrial respiration in cells infected with sh*PDHA1* when compared to control (Supplementary Fig. 3l). Spheres forming ability in LNCaP, 22Rv1, and PC3 was also impaired upon *PDHA1* inactivation (Fig. 1h-j, Supplementary Fig. 3m and uncropped blots in Supplementary Fig. 14). 22Rv1 and PC3 prostate cancer cells, infected with sh*PDHA1* also formed smaller tumours *in vivo* than controls (Fig. 1k, l and uncropped blots in Supplementary Fig. 12).

***Pdha1* inactivation decreases mitochondrial intermediates.**

Next, we performed metabolomics analysis in WT, *Pdha1*$^{pc-/Y}$, *Pten*$^{pc-/-}$ and *Pten*$^{pc-/-}$; *Pdha1*$^{pc-/Y}$ prostates. *Pten*$^{pc-/-}$ tumours presented signs of increased TCA cycle as measured by increased, citrate, α-ketoglutarate, acetyl CoA, ATP production and NADH levels (Supplementary Fig. 4a-d, Supplementary Table 4 and Supplementary Note). Increased extracellular lactate levels in *Pten* null MEFs also suggested increased glycolytic flux in these cells when compared to control (Supplementary Fig. 4e and Supplementary Note). *Pdha1* inactivation in *Pten* null tumours and

MEFs resulted in decreased TCA cycle intermediates such as citrate and α-ketoglutarate and affected NADH/NAD$^+$ ratio, ATP and acetyl-CoA levels (Supplementary Fig. 4a-f, Supplementary Table 4 and Supplementary Note). However, glycolysis and lactate production were not consistently affected (Supplementary Fig. 4a, e), in agreement with previous findings in different models[20-22]. Of note, oxaloacetate levels significantly increased in compound mutant mice, in line with a block in the cycle due to loss of acetyl-CoA production downstream PDC (Supplementary Fig. 4a, d and Supplementary Table 4). To determine whether *Pdha1* inactivation induces changes in central carbon metabolism we measured stationary flux[5,20] through TCA cycle in prostate epithelial cells derived from transgenic mice of different genotypes, using ^{13}C-stable isotope labeled glucose, glutamine, and palmitate respectively. This analysis showed increased glucose and glutamine incorporation into citrate, fumarate, and malate in *Pten*$^{pc-/-}$ cells when compared to normal prostate epithelial cells. Glucose incorporation into citrate in *Pten*$^{pc-/-}$; *Pdha1*$^{pc-/Y}$ tumor cells, decreased (~70%) when compared to *Pten*$^{pc-/-}$ cells. Importantly, PDC inactivation led to compensatory oxidative glutaminolysis and to the production of acetyl-CoA from fatty acid β-oxidation for the reactivation of the TCA (reflected in a 30% increased citrate labeling from palmitate). This compensation, however, did not overcome the decreased citrate synthesis (Supplementary Fig. 4a and Supplementary Table 4). Surprisingly, glutaminolysis compensated the oxidative reactions after α-ketoglutarate to fumarate and malate until aspartate synthesis in TCA cycle. However, glutamine carbon pool was blocked from the reactions for citrate production probably due to the decreased expression of *Idh1* in *Pten*$^{pc-/-}$; *Pdha1*$^{pc-/Y}$ when compared to *Pten*$^{pc-/-}$ tumour cells (Supplementary Fig. 5d,g and Supplementary Table 5-7). Finally, the Pyruvate carboxylase activity did not change in response to *PDHA1* loss since the M+3 aspartate did not increase in *Pten*$^{pc-/-}$; *Pdha1*$^{pc-/Y}$ when compared to *Pten*$^{pc-/-}$ tumour cells

(Supplementary Fig. 4g and and Supplementary Table 5). Taken together, these data demonstrate that PDC inactivation reduces production of TCA intermediates and energetic yield in prostate tumours.

4.2 *Pdha1* knockdown induces tumour suppression by abrogating lipogenesis.

Pdha1 has been long defined as a mitochondrial metabolism regulator. However, recent evidence demonstrates that the PDC controls the nuclear pool of acetyl-CoA thereby promoting histone acetylation and regulating gene expression[23,24]. In line with this evidence, we detected a strong nuclear localization of PDHA1 in *Pten*$^{\text{pc-/-}}$ tumours and PDC activity in both the cytosol and nucleus of these tumour cells (see insets in Fig. 1d, Supplementary Figs. 1c and 5a,b and uncropped blots in Supplementary Fig. 14). We also detected Pdha1, Dlat and Dld in the nuclear fractions of *Pten*$^{\text{pc-/-}}$ tumor cells (Supplementary Fig. 5c and uncropped blots in Supplementary Fig. 14). Transcriptomics followed by GSEA analysis in *Pten*$^{\text{pc-/-}}$ and *Pten*$^{\text{pc-/-}}$; *Pdha1*$^{\text{pc-/Y}}$ tumours demonstrated that fatty acid synthesis, cholesterol biogenesis and genes controlled by the sterol responsive element binding factor (SREBF)[25-28] were the most downregulated pathways in *Pten*$^{\text{pc-/-}}$; *Pdha1*$^{\text{pc-/Y}}$ tumours (Fig. 2a). Inactivation of *Pdha1* in *Pten*$^{\text{pc-/-}}$ tumours and sh*PDHA1* human prostate cancer cells decreased Histone H3 Lysine 9 acetylation (H3K9Ac) thereby potentially affecting gene expression (Fig. 2b,c and uncropped blots in Supplementary Fig. 12). Notably, two rate-limiting enzymes engaging fatty acid synthesis and cholesterol biogenesis, ATP Citrate Lyase (Acly)[29,30] and Squalene Epoxidase (Sqle) [31,32] were strongly decreased in both *Pten*$^{\text{pc-/-}}$; *Pdha1*$^{\text{pc-/Y}}$ tumours and sh*PDHA1* human prostate cancer cell lines at both protein and gene expression levels (Fig. 2b-f). Downregulation of ACLY in these cells was not associated with the upregulation of Acyl-coenzyme A synthetase short-chain family member 2 (ACSS2)[33,34] (Fig. 2d,e). Genes that divert TCA cycle and glutamine intermediates into the lipid metabolisms[22,35,36] were also downregulated by *PDHA1* inactivation in both mouse and human prostate tumour cells (Supplementary Fig. 5d-f). Importantly, acetate supplementation[30] in the culture media of 22Rv1 and PC3 infected with sh*PDHA1*, restored global H3K9Ac, SQLE and ACLY levels (Fig. 2c). Chromatin immunoprecipitation (ChIP) analysis demonstrated that H3K9Ac and the binding of SREBF1 on the promoters of *ACLY* and *SQLE* decreased in response to *the PDHA1* knockdown in human prostate cancer cells and this was restored by acetate supplementation (Supplementary Fig. 5h, i and Fig. 2g,h). Acetate supplementation restored cell growth in both *Pten*$^{-/-}$; *Pdha1*$^{-/Y}$ MEFs and *shPDHA1* 22Rv1 and PC3 cells (Fig. 2i-k). Of note, we did not detect any changes in H3K9Ac on the promoter of two cell cycle regulators, E2F Transcription Factor 1 (*E2F1*) and Cyclin D1 (*CCND1*), demonstrating the specificity of the epigenetic regulation of PDC in cancer cells (Supplementary Fig. 5j,k). Interestingly, ACLY over-expression in prostate cell lines infected with sh*PDHA1* rescued the growth arrest induced by loss of *PDHA1* only in cells supplemented with citrate (Supplementary Fig. 5l-n and uncropped blots in Supplementary Fig. 14) in agreement with previous data[30].

We next performed a direct measurement of lipid species in mouse prostate tumours and human prostate cancer cell lines depleted of *PDHA1*. Of note, the majority of lipid species, including cholesterol ester were decreased in *Pten*$^{pc-/-}$; *Pdha1*$^{pc-/Y}$ when compared to *Pten*$^{pc-/-}$ tumours and in *shPDHA1* 22Rv1 and PC3 cells when compared to control cells (Supplementary Fig. 6, Supplementary Table 8-11 and Supplementary Note). ^{14}C tracking experiments in sh-*PDHA1* 22Rv1 and PC3 cells demonstrated that glucose and glutamine incorporation into lipids and cholesterol (Supplementary Fig. 7a-e and Supplementary Note) were strongly affected when compared to controls whereas glucose and glutamine incorporation into proteins, remained unchanged (Supplementary Fig. 7f,g and Supplementary Note). *PDHA1* knockdown did not affect glucose uptake but induced a slight increase of glutamine uptake (Supplementary Fig. 7h, i and Supplementary Note). In agreement with these findings lipid droplets, a known readout of lipid production[5,37], were strongly reduced in both mouse and human xenograft tumours upon *PDHA1* inactivation (Fig. 3a-d and Supplementary Fig. 7j-o). To assess whether lipid metabolism is affected by *PDHA1* inactivation, we cultured sh-*PDHA1* 22Rv1 and PC3 cells in both the presence and absence of fatty acids and we found that fatty acids fully rescued the growth arrest induced by the *PDHA1* knockdown. This was associated with the restoration of lipid droplets in the same cells (Fig. 3e,f and Supplementary Note). Rescue of proliferation upon fatty acid supplementation occurs independently by H3K9 acetylation and reactivation of the expression of ACLY and SQLE (Supplementary Fig. 7p and uncropped blots in Supplementary Fig. 15). This data suggests that fatty acids were directly incorporated into lipids. Collectively, these data demonstrate that PDC activity is required for the proliferation of mouse and human prostate tumour cells and that inactivation of PDC drives tumour growth inhibition by affecting histone acetylation and the expression of genes controlling lipid metabolism.

4.3 Nuclear PDC regulates the expression of lipid biosynthesis genes independently of mitochondrial PDC.

Cellular compartmentalization allows cells to carry out different metabolic reactions at the same time, and pathological protein compartmentalization is associated with cancer[38]. We, therefore, dissected the role of nuclear and cytosolic PDC in prostate cancer, by expressing nuclear export signal (NES) and/or nuclear localization signal (NLS) fused PDHA1 vectors in prostate cancer cell lines previously infected with (shRNA) and without PDHA1 (sh*PDHA1*) (Fig. 4a, uncropped blots in Supplementary Fig. 13 and Supplementary Fig. 8a). NES-PDHA1 and NLS-PDHA1 constructs were engineered as sh*PDHA1* resistant vectors. Expressions of these vectors in 22Rv1 cells did not affect SREBF1 maturation and nuclear translocation (Supplementary Fig. 8a). Restoration of NLS-PDHA1 in sh-*PDHA1* cells recovered H3K9Ac and the expression of fatty acid synthesis genes (Fig. 4b-d, Supplementary Fig. 8b for the full panel and uncropped blots in Supplementary Fig. 13,15), but did not rescue citrate levels, lipids content and cell growth both *in vitro* and *in vivo* (Fig. 4e-h and Supplementary Fig. 8c-g). In contrast, overexpression of both NES-PDHA1 and NLS-PDHA1 restored lipid synthesis genes, citrate levels, lipids content and cell growth (Fig. 4b-h and Supplementary Fig. 8b-g). Interestingly, the selective ACLY inhibitor, SB-204990 partially decreased H3K9 acetylation in prostate cancer cells with high PDC activity and SB-204990 did not further increase the growth arrest in prostate cancer cells infected with a shRNA against *PDHA1* (Supplementary Fig. 8h-j and uncropped blots in Supplementary Fig. 15). These data demonstrate that PDC can directly contribute to histone acetylation, independently by the regulation of ACLY[30]. These experiments reveal that nuclear PDC regulates the expression of lipid synthesis gene in an autonomous manner and both nuclear and cytosolic PDHA1 are needed for the proliferation of prostate cancer cells.

4.4 Nuclear PDC regulates fatty acid synthesis in presence of mitochondrial citrate.

Consistently with these findings, we proved that overexpression of NLS-PDHA1 rescued growth arrest and lipid synthesis in cells cultured in the presence of citrate (Fig. 5a, b and Supplementary Fig. 9a for the whole panel). To validate these findings using an additional system, we overexpressed PDK1 in prostate cancer cells. Previous evidence demonstrates that PDK1 overexpression suppresses mitochondrial metabolism decreasing the intracellular levels of citrate without halting the nuclear function of PDC[23,39-41]. In line with this evidence overexpression of PDK did not promote phosphorylation of nuclear PDHA1 (Supplementary Fig. 9b and uncropped blots in Supplementary Fig. 15). Overexpression of PDK1 in 22Rv1 cells decreased citrate levels and slightly suppresses cancer cell proliferation both *in vitro* and *in vivo* (Fig. 5c-e and Supplementary Fig. 8c-e). However, it did not decrease histone acetylation and expression of fatty acid synthesis genes (Fig. 5f, uncropped blots in Supplementary Fig. 13 and Supplementary Fig. 9b). In contrast, concomitant inactivation of *PDHA1* and overexpression of PDK1 decreased citrate level, histone acetylation and lipids content thereby suppressing tumourigenesis of a greater extent than in cells infected with PDK1 alone (Fig. 5c-f and Supplementary Fig. 9c-e). Taken together, these results demonstrate that both mitochondrial and nuclear PDC is required for prostate tumour growth.

4.5 Pharmacological inhibition of PDHA1 arrests mouse and human prostate tumours.

Given that prostate cancer relies on PDC for proliferation we assessed whether pharmacological inhibition of PDHA1 could also block tumourigenesis in *Pten*$^{pc-/-}$ tumours and human xenograft models of prostate cancer. We reasoned that a compound that could affect both the mitochondrial and nuclear function of PDC could be effective in blocking prostate cancer. To this extent, we took advantage of 3-fluoropyruvate (3-FP), a competitive inhibitor of the PDHA1[42-45]. Computer simulations confirmed that 3-FP and pyruvate bind to PDHA1 with similar affinity (Supplementary Fig. 10a, b and Supplementary Note). To assess the specificity of 3-FP for the PDC, cell lysates treated with 3-FP were incubated in presence or absence of pyruvate. 3-FP decreased the activity of PDC and this was reversed by adding pyruvate in a dose dependent manner to the reaction buffer (Supplementary Fig. 10c). 3-FP administered by intraperitoneal injection in *Pten*$^{pc-/-}$ mice inhibited the PDC activity *in vivo* in absence of systemic toxicity and induced a strong decrease of tumour cells proliferation as demonstrated by the reduced tumour size, tumour invasiveness and Ki-67 staining (Supplementary Fig. 10d-j). Importantly, 3-FP inhibited PDC both in the nucleus and the cytosol of prostate tumour cells and decreased H3K9Ac, Acly and Sqle levels *in vivo* at both protein and mRNA levels (Supplementary Fig. 10k-m and uncropped blots in Supplementary Fig. 15). Metabolomics analysis via LC-MS/MS[46] confirmed that 3-FP strongly affected pyruvate metabolism and TCA cycle (Supplementary Fig. 11a). Finally, lipids droplet staining showed a decreased percentage of the number, size and intensity of lipid bodies in *Pten*$^{\text{pc-/-}}$ tumours treated with 3-FP (Supplementary Fig. 11b-e). 3-FP treatment blocked the proliferation of different human prostate cancer cells and this was associated with a decreased PDC activity (Supplementary Fig. 11f, g). Finally, 3-FP treatment decreased the proliferation of different human prostate cancer xenografts (LNCaP, 22Rv1 and PC3) promoting long-lasting anti-tumour responses *in vivo* (Supplementary Fig. 11h-j). Taken together these data suggest that pharmacological inactivation of PDC hampers prostate cancer progression.

5. Discussion

Whether the PDC acts as an oncogene or tumour suppressor in cancer is still under debate[19,22,23,39,40,47-49]. A previous report shows that reduction in PDC activity through overexpression of PDK1 in melanoma cells promote tumour cell proliferation by enhancing glycolysis and reductive carboxylation[19]. In this and other models, activation of PDC by dichloroacetate promoted tumour suppression[19,47]. Our data provide a new angle and demonstrate that the subunits of the PDC such as PDHA1 and PDP1 are amplified and overexpressed at both gene and protein levels and that the PDC is active in prostate cancer. In line with this evidence, we demonstrate that inactivation of *PDHA1* hampers prostate cancer progression *in vivo* in both mouse and human prostate cancer models. These findings are in agreement with recent studies demonstrating that tumor cells, *in vivo,* increased glucose oxidation via PDC. *PDHA1* inactivation in non-small lung cells cancer (NSCLC) xenografts resulted in a decreased tumor formation capacity. An increased TCA cycle via PDC was also observed in poorly perfused tumours areas of patients affected by NSCLC[9,10,50]. These data, together with our data in prostate cancer, challenged the notion that tumours switch from glucose derived oxidative metabolism to aerobic glycolysis to support their growth[6]. However, the mechanisms by which tumour cells *in vivo* become addicted to PDC-mediated mitochondrial metabolisms still remain unknown. As suggested by previous studies this may be explained by the genetic background of the tumours, a difference in tissue requirements or in the composition of the tumour microenvironment[10]. Intriguingly normal prostate epithelial cells exhibit a "truncated" TCA cycle due to inhibition of aconitase needed for the production and secretion of a high quantity of citrate into the seminal fluid[51-53]. Therefore, it is not surprising that prostate cancer relies on mitochondrial metabolism more than other tumour types.

Our results reveal that in order to support prostate cancer growth the PDC must be functional in both mitochondria and the nucleus of cancer cells. Mitochondrial PDC function is not sufficient to support lipid biosynthesis in tumour cells since nuclear PDC regulates the transcription of the enzymes that convert cytosolic citrate into acetyl-coA and fatty acids (Supplementary Fig. 11k, l). This compartmentalization allows the mitochondrial production of citrate in the cytosol and the expression of enzymes required for *de novo* lipid biosynthesis. Prior studies demonstrate that prostate cancer also benefits of enhanced glycolytic metabolism. However, these aggressive glycolytic tumour cells retain an active glucose-derived lipid biosynthesis[54], thus in line with the results presented herein.

Our findings also hold important implications for cancer therapy and pave the way for the targeting of the nuclear function of PDC to eradicate prostate cancer. This may be achieved in the future as shown in this paper by using pyruvate analogs or alternatively by developing small molecule inhibitors of PDHA1.

Chen et al_Figure 1

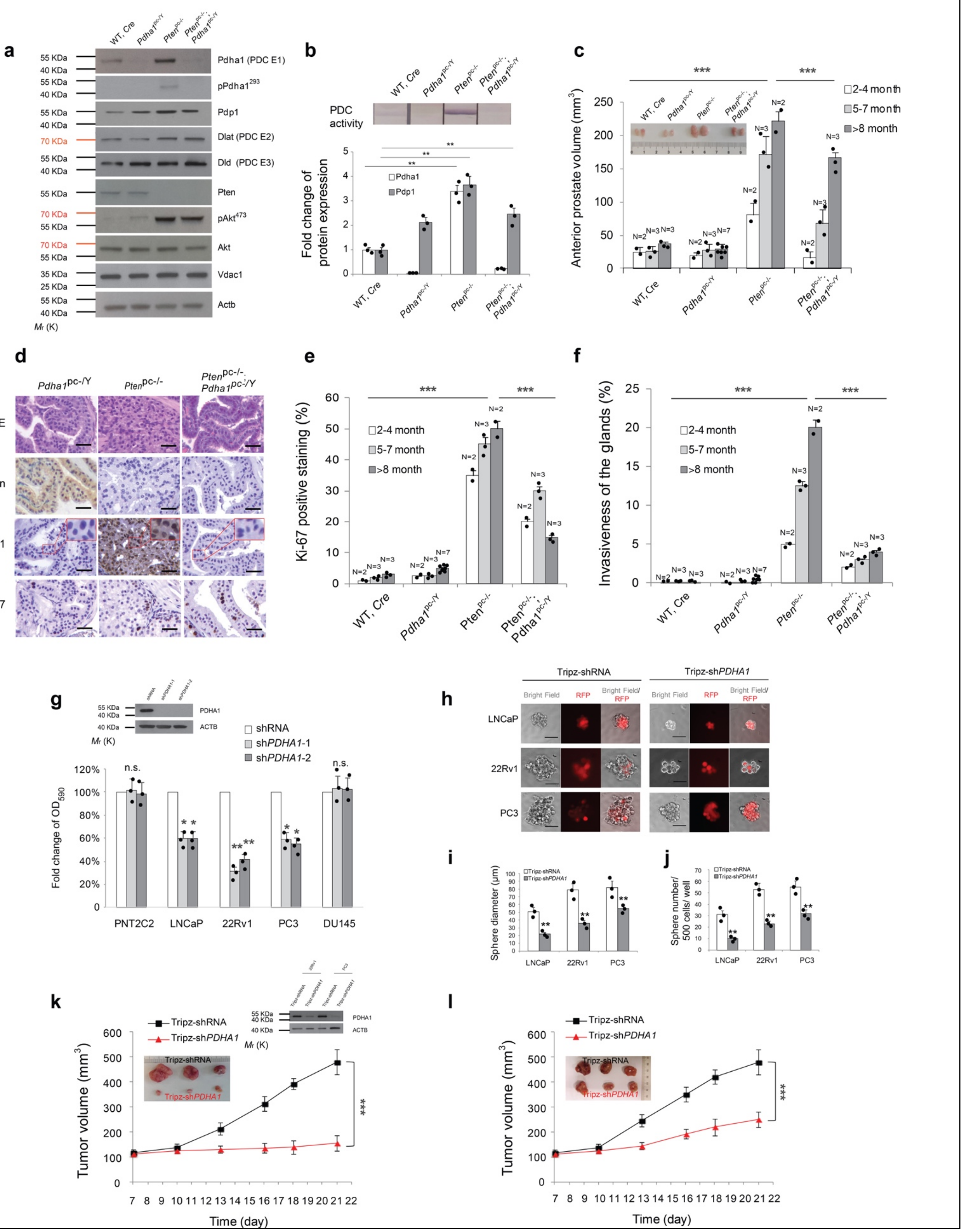

Figure 1

***Pdha1* knockout induces tumour suppression in mice and human prostate tumours.**

(**a**) Western blot analysis of indicated proteins in wild type, *Pdha1*$^{\text{pc-/Y}}$, *Pten*$^{\text{pc-/-}}$ and *Pten*$^{\text{pc-/-}}$; *Pdha1*$^{\text{pc-/Y}}$ prostates and tumours (n=3, independent prostate samples). Uncropped images are in Supplementary Figure 12. (**b**) Upper panel, PDC activity measurement in wild type, *Pdha1*$^{\text{pc-/Y}}$, *Pten*$^{\text{pc-/-}}$ and *Pten*$^{\text{pc-/-}}$; *Pdha1*$^{\text{pc-/Y}}$ prostates and tumours (n=3, independent prostate samples). Lower panel, Quantification of indicated proteins normalized to wild type tissues in indicated prostate tumours in (**a**) (n=3, independent prostate samples). (**c**) Comparison of anterior prostate (AP) lobe volumes (mm^3, 2 independent lobes per animal are presented) from male of indicated ages and genotypes between wild type, *Pdha1*$^{\text{pc-/Y}}$, *Pten*$^{\text{pc-/-}}$ and *Pten*$^{\text{pc-/-}}$; *Pdha1*$^{\text{pc-/Y}}$ prostate and tumours (N, the number of mice of indicated ages). Inset is the representative image of anterior prostate lobes in the panel. (**d**) Representative micrographs in histopathological analysis (haematoxylin/eosin staining and indicated proteins) of anterior prostates (AP) in *Pdha1*$^{\text{pc-/Y}}$, *Pten*$^{\text{pc-/-}}$ and *Pten*$^{\text{pc-/-}}$; *Pdha1*$^{\text{pc-/Y}}$ prostate tissues from 12 weeks old male mice (n=3) (Scale bar represents 50 μm, insets are regions shown in higher magnification, see also Supplementary Fig. 1c for all the genotypes and images of lower magnification). (**e,f**) Quantification of the percentage of Ki-67 positive cells (**e**) and invasive prostate glands (**f**) in prostates from mice of indicated genotypes at different ages (N, number of mice of indicated ages). (**g**) Relative cell number quantification by crystal violet staining in the indicated prostate cancer cell lines infected with sh*PDHA1* or scramble control. Data is normalized to shRNA control. PDHA1 inhibition validated by western blot analysis using two different sh*PDHA1* was shown in the inset of the panel. Uncropped images are in Supplementary Figure 12. (n=3, independent cell cultures). (**h**) Spheroid Formation Assays in LNCaP, 22Rv1 and PC3 cells infected with doxycycline-induced Tripz-sh*PDHA1* or scramble control (n=3, independent cell cultures). Scale bar represents 50 μm. (**i,j**) Quantification of spheroid diameter (**i**) and spheroid number per 500 cells (**j**) in LNCaP, 22Rv1 and PC3 cells infected with doxycycline-induced Tripz-sh*PDHA1* or scramble Tripz-shRNA control (n=3, independent cell cultures). (**k,l**) Evaluation of tumour formation in xenotransplantation experiments of 22Rv1 (**k**) and PC3 (**l**) cells infected with indicated sh*PDHA1* or scramble shRNA control. The knockdown of *PDHA1* in 22Rv1 and PC3 xenograft tumours is validated by western blot in the inset of panel (**k**). Uncropped images are in Supplementary Figure 12. (n=6 animals; 12 independent tumour samples). Error bars indicate s.e.m. **$P < 0.01$; ***$P < 0.001$. n.s, not significant.

Chen et al_Fig. 2

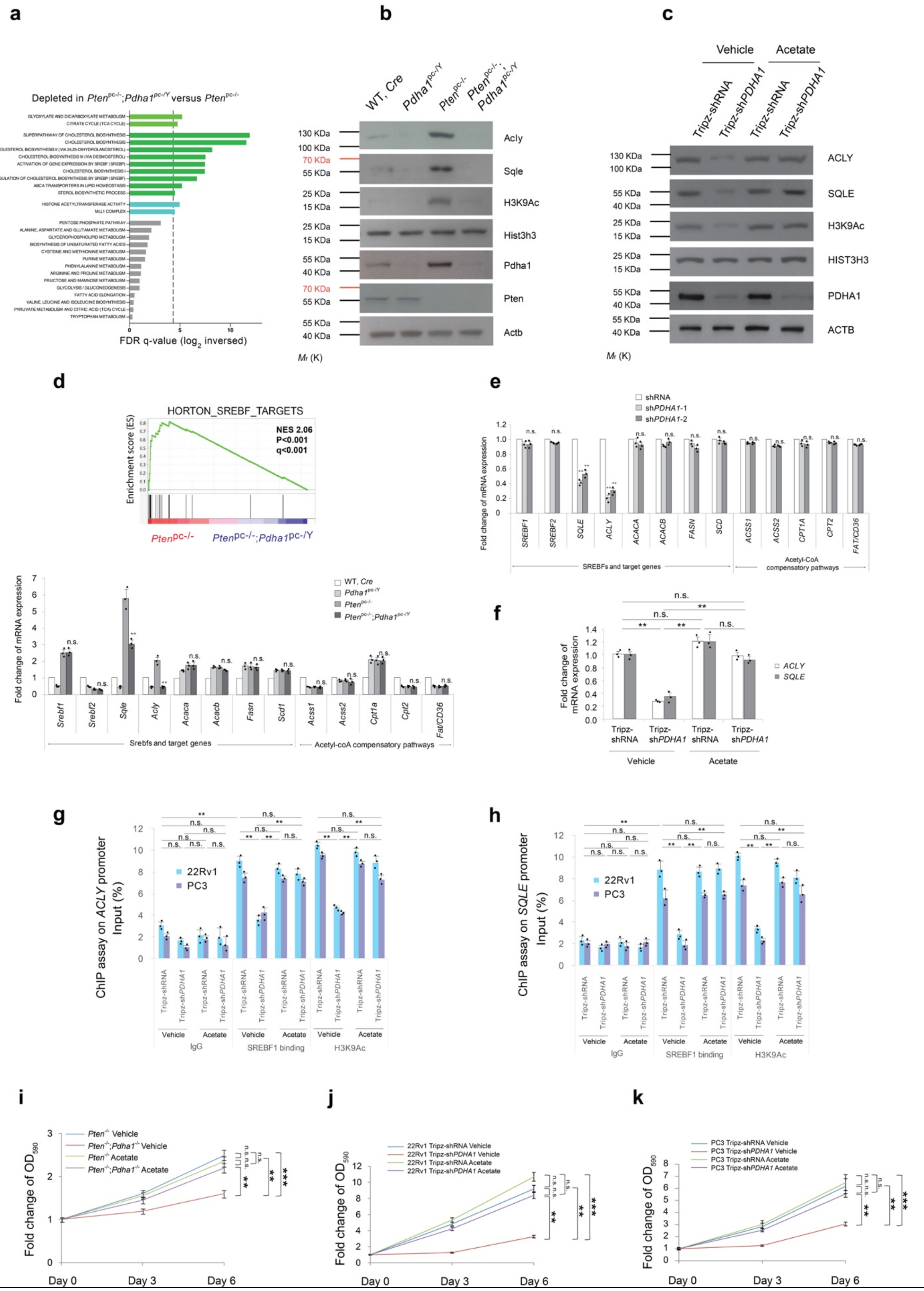

Figure 2

***Pdha1* inactivation induces tumour suppression by down-regulating lipogenic genes.**

(**a**) Gene expression profile analysis based on metabolic pathway datasets (GOCC, Gene Ontology Cellular Component; KEGG, Kyoto Encyclopaedia of Genes and Genomes; GOBO, Gene expression-based Outcome; GOMF, Gene Ontology Molecular Function; HumanCyc; Reactome) in *Pten*$^{\mathrm{pc-/-}}$; *Pdha1*$^{\mathrm{pc-/Y}}$ tumours versus *Pten*$^{\mathrm{pc-/-}}$ tumours. Dotted line indicates P=0.05 (n=3). (**b**) Western blot analysis of indicated proteins in wild type, *Pdha1*$^{\mathrm{pc-/Y}}$, *Pten*$^{\mathrm{pc-/-}}$ and *Pten*$^{\mathrm{pc-/-}}$; *Pdha1*$^{\mathrm{pc-/Y}}$ prostates and tumours. Uncropped images are in Supplementary Figure 12. (n=3, independent prostate samples). (**c**) Western blot analysis of indicated proteins in 22Rv1 cells infected with doxycycline-induced Tripz-sh*PDHA1* or scramble control and treated with 100 μM acetate or vehicle over a 6-day period. Uncropped images are in Supplementary Figure 12. (n=3, independent cell cultures). (**d**) Upper panel, GSEA of SREBF target genes in *Pten*$^{\mathrm{pc-/-}}$; *Pdha1*$^{\mathrm{pc-/Y}}$ versus *Pten*$^{\mathrm{pc-/-}}$ prostate tumours. Normalized enriched scores (NES) are presented. Data are mean ± standard deviation (s.d.). Lower panel, quantitative real time-PCR analysis of mRNA expression of indicated SREBFs and target genes and genes in acetyl CoA compensatory pathways in mouse prostate and tumours the indicated genotypes (n=3). (**e**) Quantitative real time-PCR analysis of mRNA expression of indicated SREBFs and target genes and genes in acetyl coA compensatory pathways in 22Rv1 cells infected with sh*PDHA1* and scramble shRNA control (n=3, independent cell cultures). (**f**) Quantitative RT-PCR analysis of *ACLY* and *SQLE* in 22Rv1 cells infected with doxycycline-induced Tripz-sh*PDHA1* or scramble control and treated with acetate (100 μM) or vehicle for 6 days (n=3, independent cell cultures). (**g,h**) Chromatin immunoprecipitation analysis showing the binding of SREBF1 and H3K9Ac on the promoters of *ACLY* (**g**) and *SQLE* (**h**) in 22Rv1 and PC3 cells infected with doxycycline-induced Tripz-sh*PDHA1* or scramble control and treated with 100 μM acetate or vehicle over a 6-day period (n=3, independent cell cultures). (**i-k**) Relative cell number quantification by crystal violet staining of *Pten*$^{-/-}$ and *Pten*$^{-/-;}$ *Pdha1*$^{-/Y}$ MEFs (**i**) and human cancer cells 22Rv1 and PC3 cells infected with doxycycline-induced Tripz-sh*PDHA1* or scramble control. (**j,k**) and treated with acetate (100 μM) or vehicle over a 6-day period (n=3, independent cell cultures). Error bars indicate s.e.m. $^{*}P < 0.05$; $^{**}P < 0.01$; $^{***}P < 0.001$. n.s, not significant.

Chen et al_Fig. 3

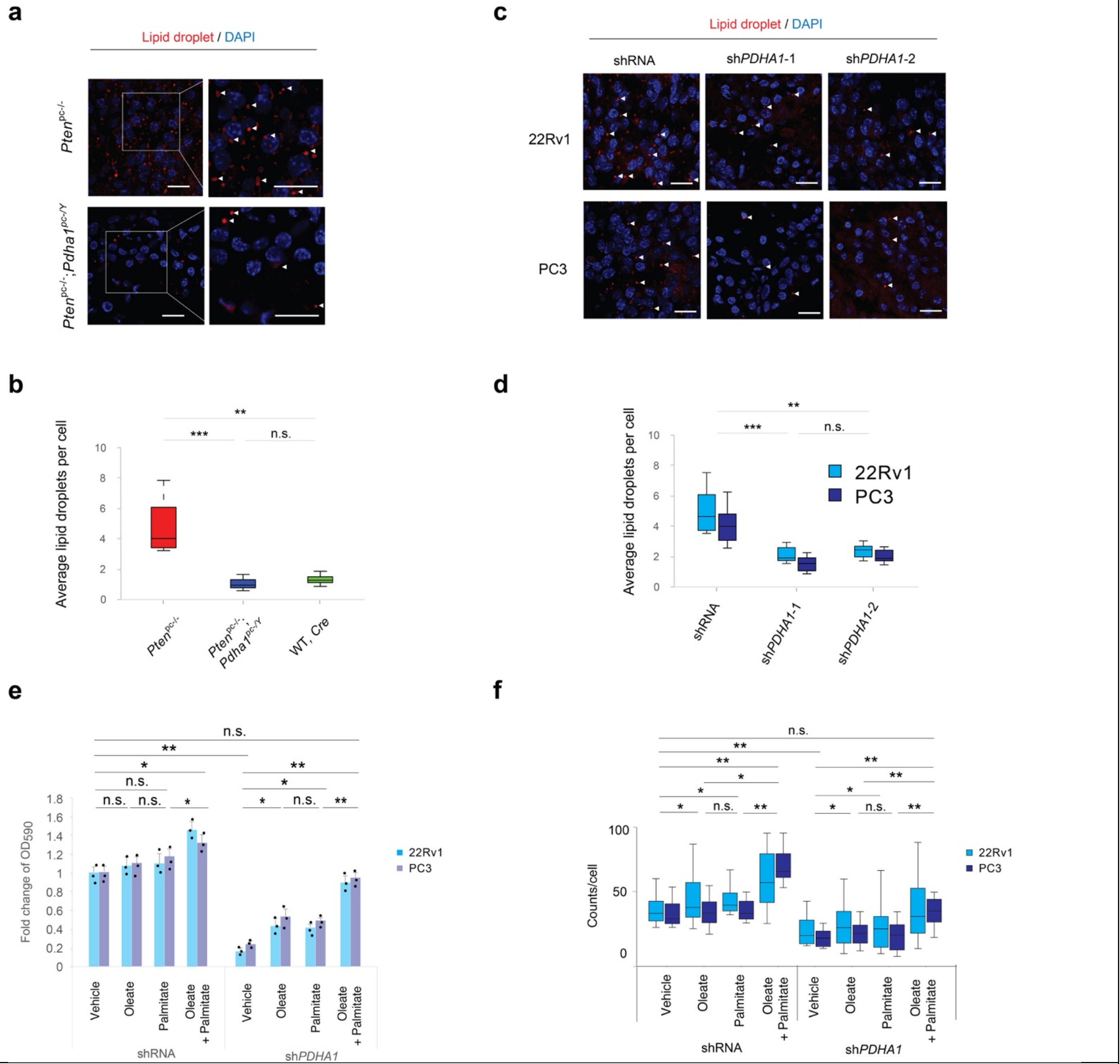

Figure 3

***Pdha1* knockdown induces tumour suppression by abrogating lipogenesis.**

(**a,b**) Representative confocal images (**a**) and quantification of average lipid droplets per cell (Lipidtox, red) (**b**) in the indicated genotypes in *Pten*$^{pc-/-}$; *Pdha1*$^{pc-/Y}$ versus *Pten*$^{pc-/-}$ prostate tumours. DAPI, blue. (n=3 mice, Scale bar: 20 µm, 1 tumour per mouse, 5 fields acquired). (**c,d**) Representative confocal images (**c**) and quantification of average lipid droplets per cell (Lipidtox, red) (**d**) in 22Rv1 and PC3 sh*PDHA1* and shRNA xenograft tumours. DAPI, blue. (n=3 mice, Scale bar represents 20 µm, 1 tumour per mouse, 5 fields acquired). (**e,f**) Relative cell number quantification by crystal violet staining (**e**) and quantification of lipid droplets by average lipid droplet per cell (**f**) in 22Rv1 and PC3 cells infected with a sh*PDHA1* and scramble shRNA control and treated with exogenous fatty acids in fatty acid free media; oleate (25 µM), palmitate (25 µM) or a combination of these two were used(n=3, independent cell cultures). Error bars indicate s.e.m. *$P < 0.05$; **$P < 0.01$; ***$P < 0.001$. n.s, not significant.

Chen et al_Fig. 4

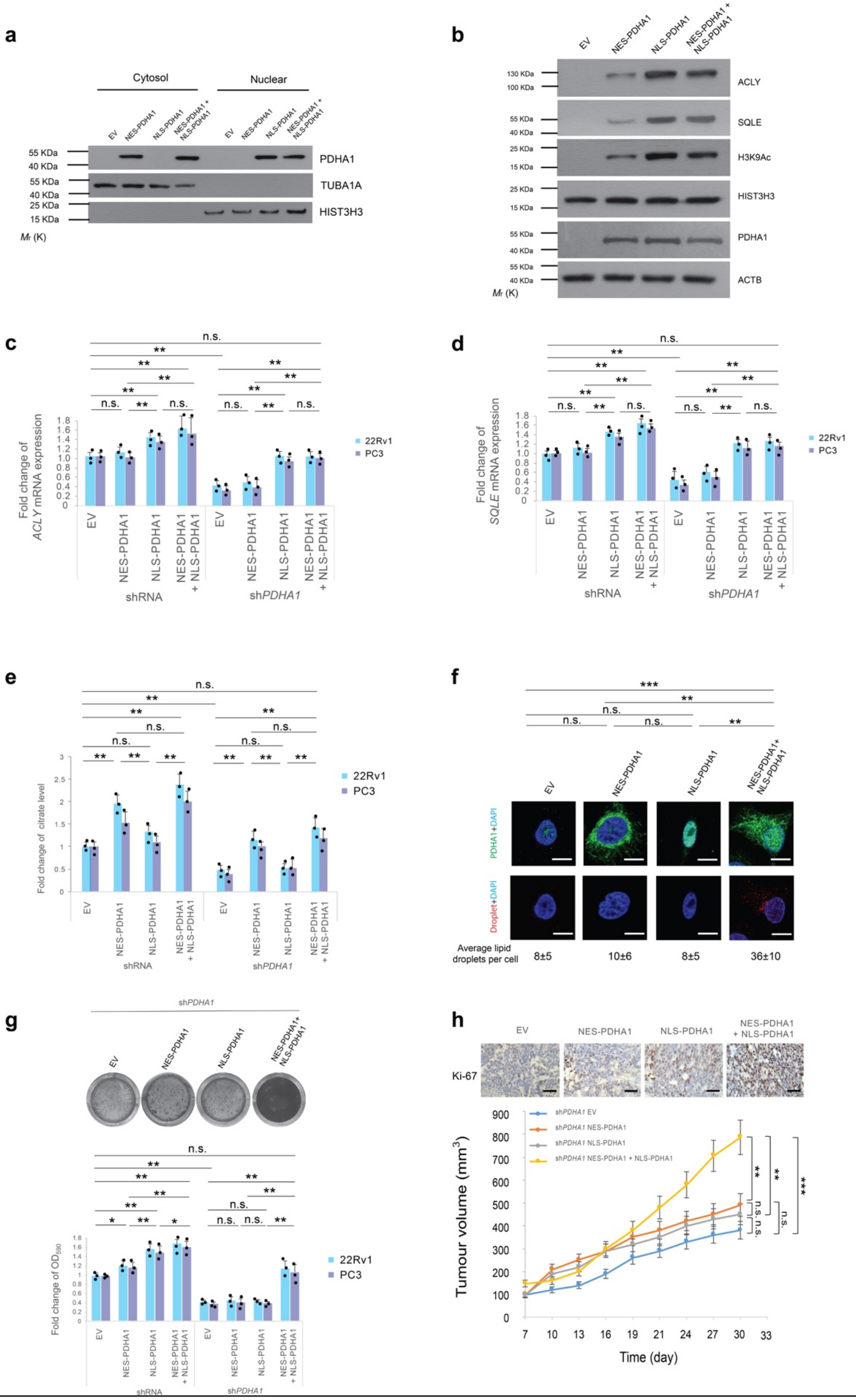

Figure 4

Nuclear PDC regulates the expression of lipid biosynthesis genes independently of mitochondrial PDC.

(**a**) Western blot analysis of indicated proteins in nuclear and cytoplasmic fractions of sh*PDHA1* 22Rv1 cells infected with NES-PDHA1 and NLS-PDHA1 alone or in combination. Uncropped images are in Supplementary Figure 13. (n=3, independent cell cultures). (**b**) Western blot analysis of indicated proteins in sh*PDHA1* 22Rv1 cells infected NES-PDHA1 and NLS-PDHA1 alone or in combination (see full panel in Supplementary Fig. 5b). Uncropped images are in Supplementary Figure 13. (n=3, independent cell cultures). (**c-e**) Quantitative real-time PCR analysis of mRNA expression for *ACLY* (**c**) and *SQLE* (**d**) and determination of citrate levels (**e**) in shRNA control and sh*PDHA1* 22Rv1 and PC3 infected with NES-PDHA1, NLS-PDHA1 alone or in combination (n=3, independent cell cultures). (**f**) Representative confocal images and quantification of lipid droplets (average lipid droplets per cell) in sh*PDHA1* 22Rv1 infected with NES-PDHA1, NLS-PDHA1 alone or in combination (n=3, independent cell cultures, Scale bar represents 10 µm, 5 fields acquired for each group). (**g**) Upper panel, representative images of crystal violet staining of sh*PDHA1* 22Rv1 infected with infected with NES-PDHA1, NLS-PDHA1 alone or in combination (n=3, independent cell cultures). Lower panel, relative cell number quantification by crystal violet staining in shRNA control and sh*PDHA1* 22Rv1 and PC3 infected with NES-PDHA1, NLS-PDHA1 alone or in combination (n=3, independent cell cultures). (**h**) Upper panel, representative micrographs in histopathological analysis of Ki-67 of these xenograft tumours. Lower panel, evaluation of tumour formation in xenotransplantation experiments of sh*PDHA1* 22Rv1 infected with NES-PDHA1, NLS-PDHA1 alone or in combination (n=6 animals; 12 injections, Scale bar represents 50 µm, also see Supplementary Fig. 7d for the full panel). Error bars indicate s.e.m. $*P < 0.05$; $**P < 0.01$; $***P < 0.001$. n.s, not significant.

Chen et al_Fig. 5

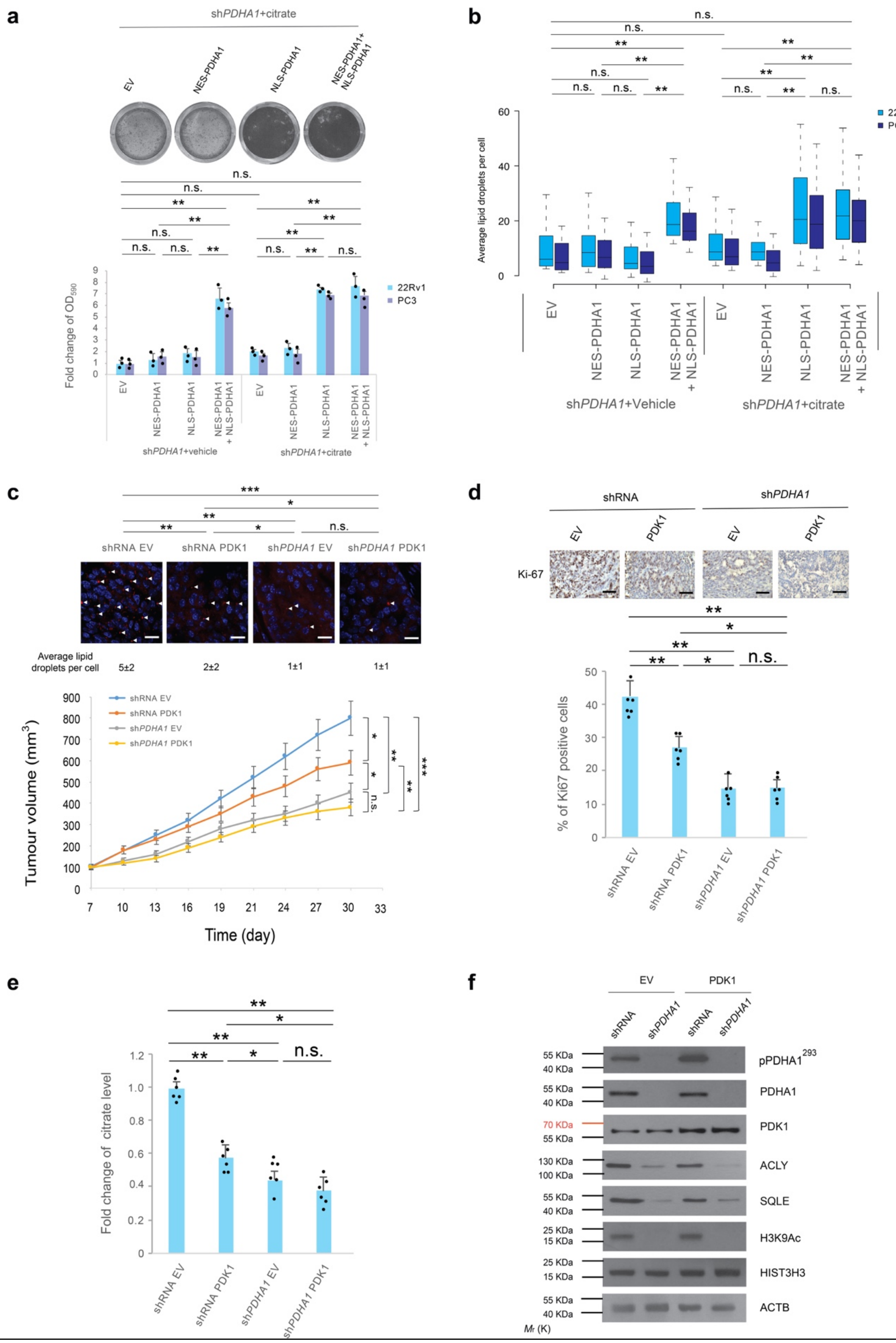

Figure 5

Nuclear PDC regulates fatty acid synthesis in presence of mitochondrial citrate.

(**a,b**) Relative cell number quantification by crystal violet (**a,** also see full panel in Supplementary Fig. 8a) and quantification by confocal microscopy of average lipid droplets per cell (**b**) in sh*PDHA1* 22Rv1 and PC3 cells infected with NES-PDHA1, NLS-PDHA1 alone or in combination and treated with citrate (100 μM) or vehicle for 6 days (n=3, independent cell cultures). (**c**) Upper panel, Representative confocal images, and quantification of average lipid droplets per cell, in xenograft tumours from shRNA control and sh*PDHA1* 22Rv1 cells infected with PDK1 or empty vector. Lower panel, Evaluation of tumour formation in xenotransplantation experiments in shRNA control and sh*PDHA1* 22Rv1 cells infected with PDK1 or empty vector (n=6 animals; 12 injections, 5 fields acquired for each group and Scale Bar represents 20 μm). (**d**) Upper panel, representative immune-histochemistry micrographs for Ki-67 staining in tumours of the indicated genotypes. (n=6 animals; 12 injections, 5 fields acquired for each group and scale bar represents 50 μm). Lower panel, quantification of the percentage of Ki-67 positive cells in different tumour genotypes (n=6 animals; 12 injections, 5 fields acquired for each group). (**e,f**) Determination of citrate levels (**e**) and western blot analysis of indicated proteins (**f**) in xenograft tumours from shRNA control and sh*PDHA1* 22Rv1 cells infected with PDK1 or empty vector. Uncropped images are in Supplementary Figure 13. (n=6, independent tumour samples). Error bars indicate s.e.m. *$P < 0.05$; **$P < 0.01$; ***$P < 0.001$. n.s, not significant.

Supplementary Fig. 1

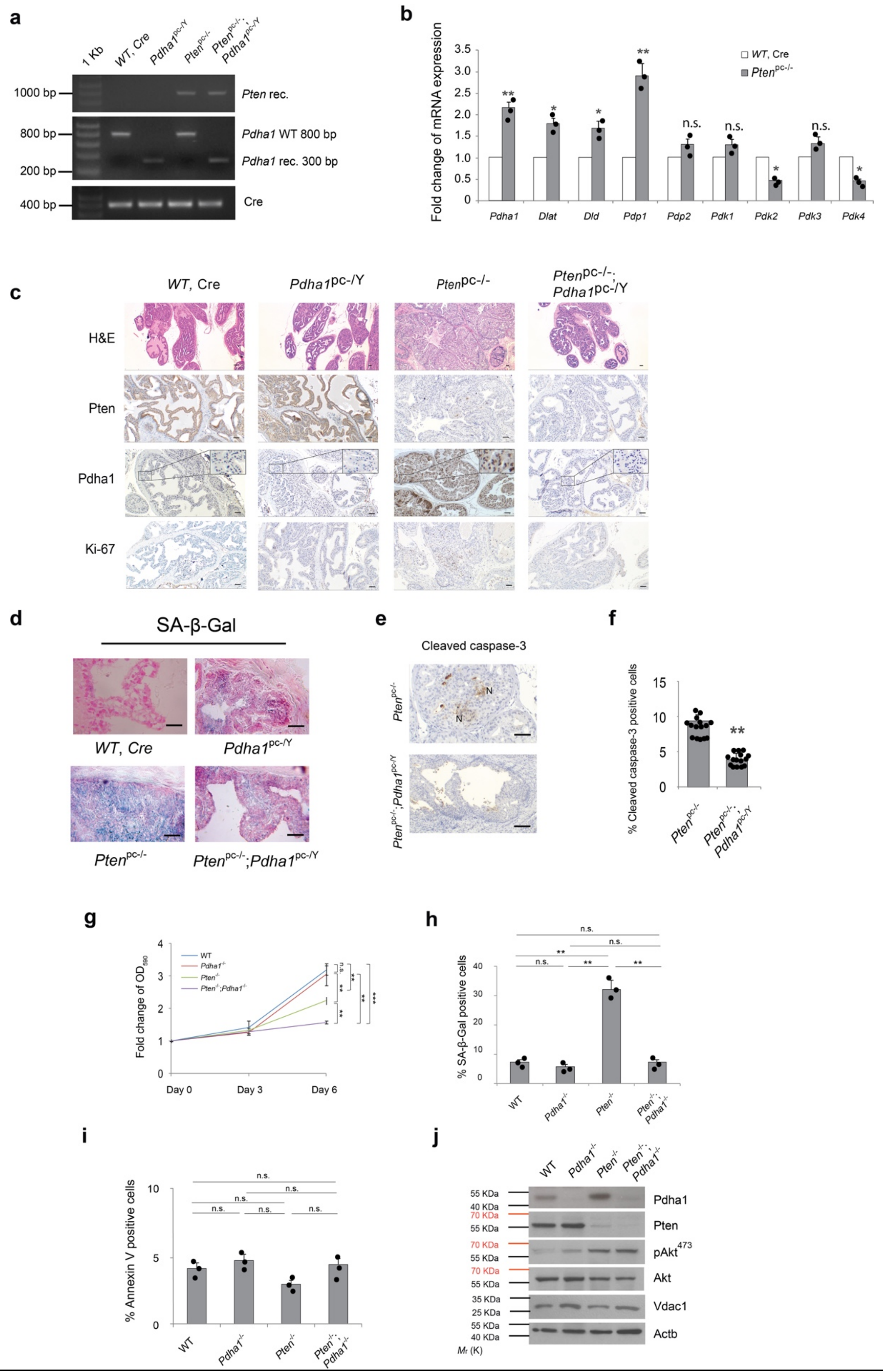

Supplementary Fig. 1

***Pdha1* knockout induces tumour suppression in mice prostate tumours.**

(**a**) The efficiency of *Probasin-Cre4 (Pb-Cre4)* mediated recombination of the *Pten*$^{loxP/loxP}$ and *Pdha1*$^{loxP/Y}$ allele as scored by PCR amplification in wild type, *Pdha1*$^{pc-/Y}$, *Pten*$^{pc-/-}$ and *Pten*$^{pc-/-}$; *Pdha1*$^{pc-/Y}$ prostates and tumours. (n=3, independent prostate samples) (**b**) Quantitative real time-PCR analysis of mRNA expression of *Pdha1, Dlat, Dld* and Pdha1 regulator genes in *Pten*$^{pc-/-}$ prostate tumours versus wild type prostate tissues (n=3, independent prostate samples)**. (c-d**) Representative micrographs in histopathological analysis (haematoxylin/eosin staining and indicated proteins) of anterior prostates (AP) (n=3, independent prostate samples, 5 fields for each group, scale bar represents 50 µm) (**c**) and representative micrographs of senescence associated β-Gal (SA- β-Gal) staining (n=3 independent prostate samples, 5 fields for each group and scale bar represents 50 µm) (**d**) in wild type, *Pdha1*$^{pc-/Y}$, *Pten*$^{pc-/-}$ and *Pten*$^{pc-/-}$; *Pdha1*$^{pc-/Y}$ prostates and tumours. (**e, f**) Apoptosis analysis by cleaved caspase 3 (**e**) and quantification of the percentage of cleaved caspase 3 positive cells (**f**) of anterior prostates (AP) in 12-week-old *Pten*$^{pc-/-}$ and *Pten*$^{pc-/-}$; *Pdha1*$^{pc-/Y}$ tumours (N: small necrotic foci, n=3 mice, 5 fields for each group and scale bar represents 50 µm). (**g-j)** Relative cell number quantification by crystal violet staining (**g**), senescence associated β-Gal (SA-β-Gal) staining (**h**), cellular apoptosis assay by Annexin V staining (**i**) and western blot analysis of indicated proteins (**j**) of wild type, *Pdha1*$^{-/-}$, *Pten*$^{-/-}$ and *Pten*$^{-/-}$; *Pdha1*$^{-/-}$ MEFs on 6th day after retroviral Cre infection and selection. Uncropped images are in Supplementary Figure 13. (n=3, independent cell cultures). Error bars indicate s.e.m. $*P < 0.05$; $**P < 0.01$. n.s, not significant.

Supplementary Fig. 2

a

	Primary vs normal DNA	Primary vs normal mRNA	Metastasis vs primary DNA	Metastasis vs primary mRNA	Metastasis vs normal DNA	Metastasis vs normal mRNA
	Significantly amplified	Significantly overexpressed	Significantly amplified	Significantly overexpressed	Significantly amplified	Significantly overexpressed
PDHA1	1 out of 3 datasets	3 out of 17 datasets	2 out of 3 datasets	7 out of 13 datasets	1 out of 1 datasets	no probe
PDP1	3 out of 3 datasets	9 out of 11 datasets	3 out of 3 datasets	1 out 9 datasets	1 out of 1 datasets	no probe

b

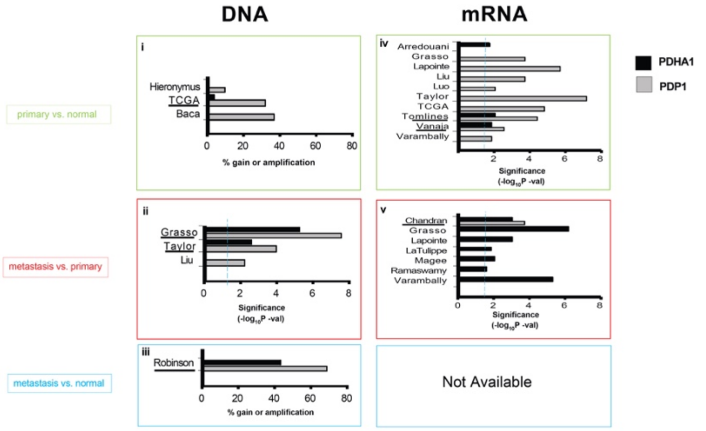

c

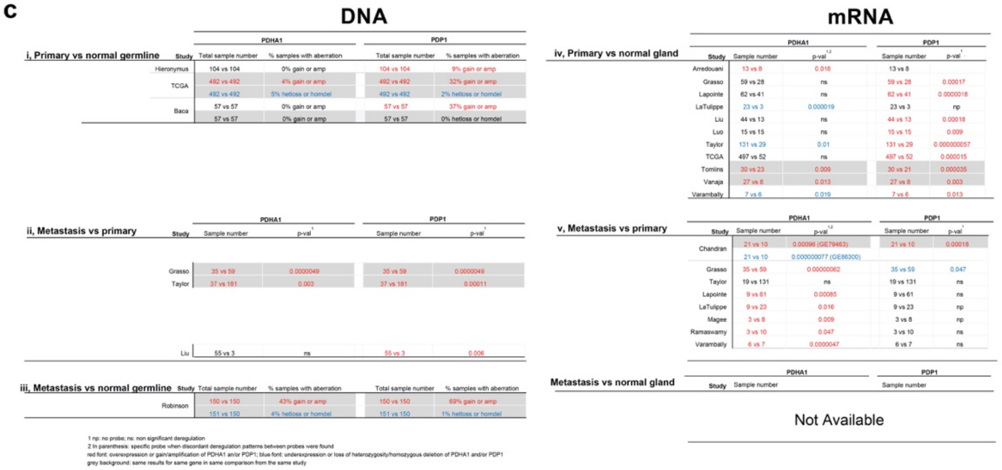

DNA

i, Primary vs normal germline

	PDHA1		PDP1	
Study	Total sample number	% samples with aberration	Total sample number	% samples with aberration
Hieronymus	104 vs 104	0% gain or amp	104 vs 104	9% gain or amp
TCGA	492 vs 492	4% gain or amp	492 vs 492	32% gain or amp
	492 vs 492	5% hetloss or homdel	492 vs 492	2% hetloss or homdel
Baca	57 vs 57	0% gain or amp	57 vs 57	37% gain or amp
	57 vs 57	0% gain or amp	57 vs 57	0% hetloss or homdel

ii, Metastasis vs primary

	PDHA1		PDP1	
Study	Sample number	p-val[1]	Sample number	p-val[1]
Grasso	35 vs 59	0.0000049	35 vs 59	0.0000049
Taylor	37 vs 181	0.003	37 vs 181	0.00011
Liu	55 vs 3	ns	55 vs 3	0.006

iii, Metastasis vs normal germline

	PDHA1		PDP1	
Study	Total sample number	% samples with aberration	Total sample number	% samples with aberration
Robinson	150 vs 150	43% gain or amp	150 vs 150	69% gain or amp
	151 vs 150	4% hetloss or homdel	151 vs 150	1% hetloss or homdel

1 np: no probe; ns: non significant deregulation

2 In parenthesis: specific probe when discordant deregulation patterns between probes were found

red font: overexpression or gain/amplification of PDHA1 an/or PDP1; blue font: underexpression or loss of heterozygosity/homozygous deletion of PDHA1 and/or PDP1

grey background: same results for same gene in same comparison from the same study

mRNA

iv, Primary vs normal gland

	PDHA1		PDP1	
Study	Sample number	p-val[1,2]	Sample number	p-val[1]
Arredouani	13 vs 8	0.018	13 vs 8	
Grasso	59 vs 28	ns	59 vs 28	0.00017
Lapointe	62 vs 41	ns	62 vs 41	0.0000018
LaTulippe	23 vs 3	0.000019	23 vs 3	np
Liu	44 vs 13	ns	44 vs 13	0.00018
Luo	15 vs 15	ns	15 vs 15	0.009
Taylor	131 vs 29	0.01	131 vs 29	0.000000057
TCGA	497 vs 52	ns	497 vs 52	0.000015
Tomlins	30 vs 23	0.009	30 vs 21	0.000035
Vanaja	27 vs 8	0.013	27 vs 8	0.003
Varambally	7 vs 6	0.019	7 vs 6	0.013

v, Metastasis vs primary

	PDHA1		PDP1	
Study	Sample number	p-val[1,2]	Sample number	p-val[1]
Chandran	21 vs 10	0.00096 (GE79463)	21 vs 10	0.00018
	21 vs 10	0.000000077 (GE86300)		
Grasso	35 vs 59	0.00000062	35 vs 59	0.047
Taylor	19 vs 131	ns	19 vs 131	ns
Lapointe	9 vs 61	0.00085	9 vs 61	ns
LaTulippe	9 vs 23	0.016	9 vs 23	np
Magee	3 vs 8	0.009	3 vs 8	np
Ramaswamy	3 vs 10	0.047	3 vs 10	ns
Varambally	6 vs 7	0.0000047	6 vs 7	ns

Metastasis vs normal gland

	PDHA1	PDP1
Study	Sample number	Sample number

Not Available

d

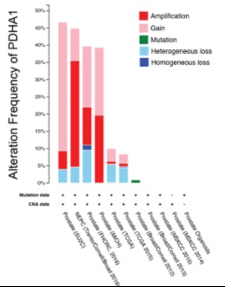

e

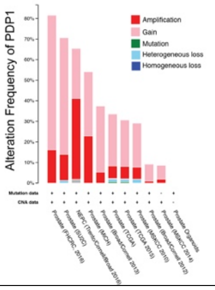

Supplementary Fig. 2

***PDHA1* and *PDP1* get frequently amplified and overexpressed in human prostate cancer.**

(**a-c**) The number of datasets (**a**), bar graph of amplification or overexpression of these datasets and underlined are comparisons (7 out of 24) where both genes are gained/amplified or overexpressed (**b**) and sample number in indicated comparison and *P* value (**c**) from Oncomine or cBioPortal cohorts by which significant copy-number gain or amplifications (DNA) or overexpression (mRNA) exits when the following comparisons are computed: i, DNA, primary versus normal germline; ii, DNA, metastasis versus primary; iii, DNA, metastasis versus normal germline; iv, mRNA, primary versus normal prostate glands and v, mRNA, metastasis versus primary. Significant overexpression or copy number values are computed using T-test (two-tailed, $P<0.05$, in ii, iv and v), or using GISTIC or RAE (in i and iii). (**d,e**) Alteration frequency analysis of *PDHA1* (**d**) and *PDP1* (**e**) from 11 studies on prostate cancers available on cBioPortal.

Supplementary Fig. 3

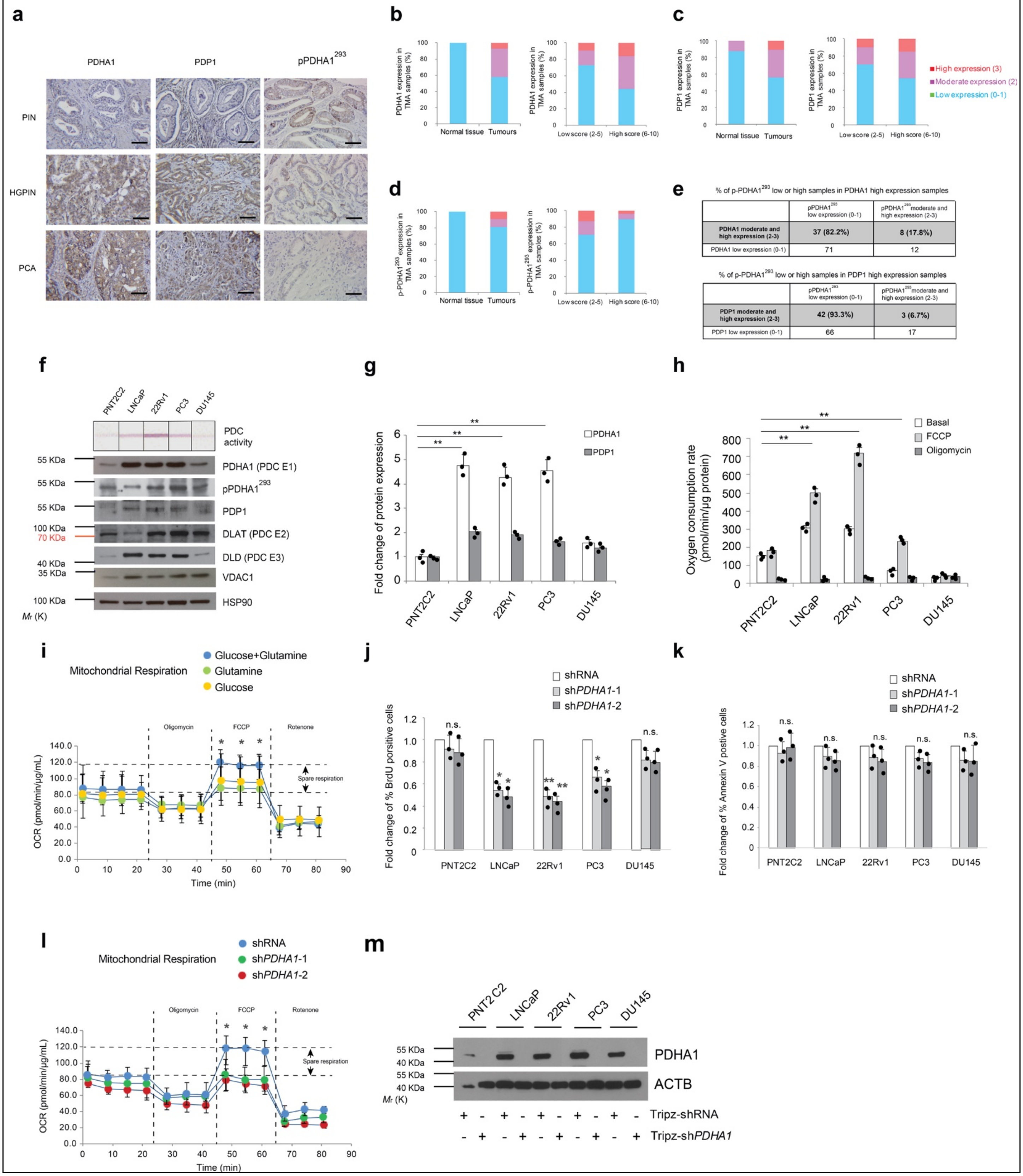

% of p-PDHA1^{293} low or high samples in PDHA1 high expression samples

	pPDHA1^{293} low expression (0-1)	pPDHA1^{293} moderate and high expression (2-3)
PDHA1 moderate and high expression (2-3)	**37 (82.2%)**	**8 (17.8%)**
PDHA1 low expression (0-1)	71	12

% of p-PDHA1^{293} low or high samples in PDP1 high expression samples

	pPDHA1^{293} low expression (0-1)	pPDHA1^{293} moderate and high expression (2-3)
PDP1 moderate and high expression (2-3)	**42 (93.3%)**	**3 (6.7%)**
PDP1 low expression (0-1)	66	17

Supplementary Fig. 3

PDHA1 and PDP1 get overexpressed in human prostate cancer cell lines and tumours.

(**a**) Representative immune-histochemical staining for PDHA1, phospho-PDHA1^{293} and PDP1 in a prostate cancer tissue microarray (TMA) of 128 patients (5 fields acquired for each sample, PIN indicates prostatic intraepithelial neoplasia, HGPIN indicates high-grade prostatic intraepithelial neoplasia, PCA indicates invasive prostate cancer, and scale bar represents 50 μm) (**b-d**) Evaluation and quantification of immune-histochemical staining for PDHA1 (**b**), PDP1 (**c**) and phospho-PDHA1^{293}(**d**) in human tumour samples in panel (**a**). (**e**) Quantification of immune-histochemical staining of phospho-PDHA1^{293} in PDHA1 or PDP1 moderate/high expression samples. The gray frames highlighted the numbers of PDHA1 or PDP1 moderate/high expression samples (**f**) Upper panel, PDC activity measurements in prostate cancer cells using a standard quantitative dipstick assay (n=3, independent cell cultures). Lower panel, western blot analysis of indicated proteins in prostate cancer cell lines. Uncropped images are in Supplementary Figure 14. (n=3, independent cell cultures). (**g**) Quantification of western blots for PDHA1 and PDP1 in panel (**f**) (n=3, independent cell cultures). (**h**) Mitochondrial oxygen consumption rate analysis of the indicated prostate cancer cell lines (n=3, independent cell cultures). (**i**) Mitochondrial oxygen consumption rate analysis of 22Rv1 prostate cancer cell line in the media supplemented with glucose (11 mM), glutamine (2 mM) or a combination of these two (n=3, independent cell cultures). (**j,k**) Cellular proliferation assay by BrdU staining (**j**) and cellular apoptosis assay by Annexin V staining (**k**) in cell lines infected with indicated sh*PDHA1* or scramble shRNA control (n=3, independent cell cultures). (**l**) Mitochondrial oxygen consumption rate analysis of 22Rv1 prostate cancer cell line infected with sh*PDHA1* or scramble control. (n=3, independent cell cultures). (**m**) Western blot analysis of PDHA1 in cell lines infected with doxycycline-induced Tripz-sh*PDHA1* or scramble control in Fig. 1 panel (**h-j**). Uncropped images are in Supplementary Figure 14. (n=3, independent cell cultures). Error bars indicate s.e.m. $*P < 0.05$; $**P < 0.01$. n.s, not significant.

Supplementary Fig. 4

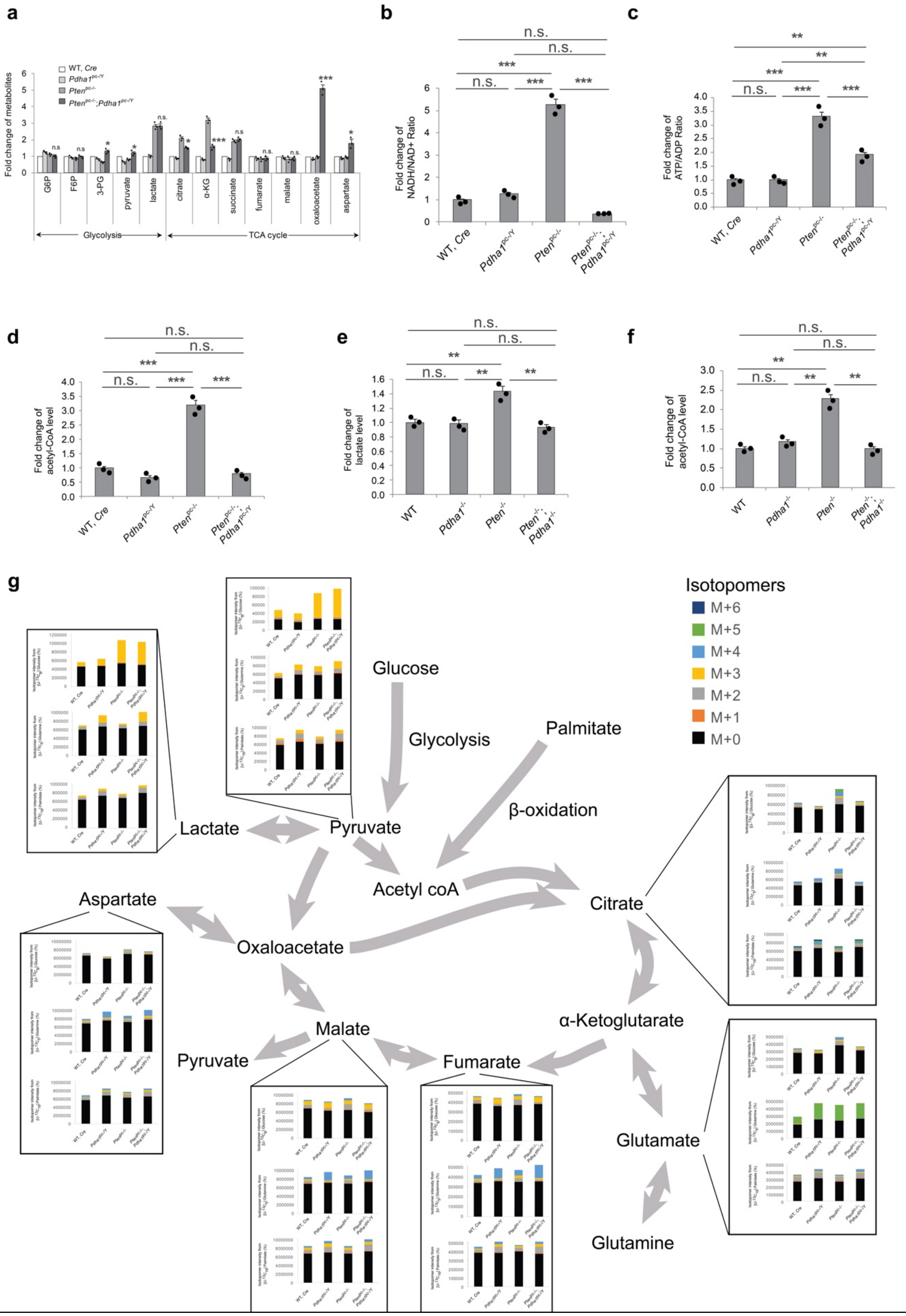

Supplementary Fig. 4

***Pdha1* inactivation decreases mitochondrial intermediates.**

(**a**) Representative intermediates level in glycolysis and tricarboxylic acid (TCA) cycle of wild type, *Pdha1*$^{\text{pc-/Y}}$, *Pten*$^{\text{pc-/-}}$ and *Pten*$^{\text{pc-/-}}$; *Pdha1*$^{\text{pc-/Y}}$ prostates and tumours (n=3, independent prostate samples). (**b-d**) Determination of relative NADH/NAD^{+} ratio (**b**), ATP/ADP ratio (**c**) and acetyl coA levels (**d**) in wild type, *Pdha1*$^{\text{pc-/Y}}$, *Pten*$^{\text{pc-/-}}$ and *Pten*$^{\text{pc-/-}}$; *Pdha1*$^{\text{pc-/Y}}$ prostates and tumours (n=3, independent prostate samples). (**e,f**) Determination of extracellular lactate levels (**e**) and acetyl coA levels (**f**) in wild type, *Pdha1*$^{-/-}$, *Pten*$^{-/-}$ and *Pten*$^{-/-}$; *Pdha1*$^{-/-}$ MEFs (n=3, independent cell cultures). (**g**) Representative data depict abundance of selected labelled metabolites from [U-$^{13}C_6$]-Glucose, [U-$^{13}C_5$]-Glutamine and [U-$^{13}C_{16}$]-palmitate respectively in mouse prostate epithelial cells derived from wild type, *Pdha1*$^{\text{pc-/Y}}$, *Pten*$^{\text{pc-/-}}$ and *Pten*$^{\text{pc-/-}}$; *Pdha1*$^{\text{pc-/Y}}$ prostates and tumours. Glucose, glutamine and Palmitate metabolism profiles were presented as actual intensities. (n=3, independent prostate samples). Error bars indicate s.e.m. *$P < 0.05$; **$P < 0.01$; ***$P < 0.001$. n.s, not significant.

Supplementary Fig. 5

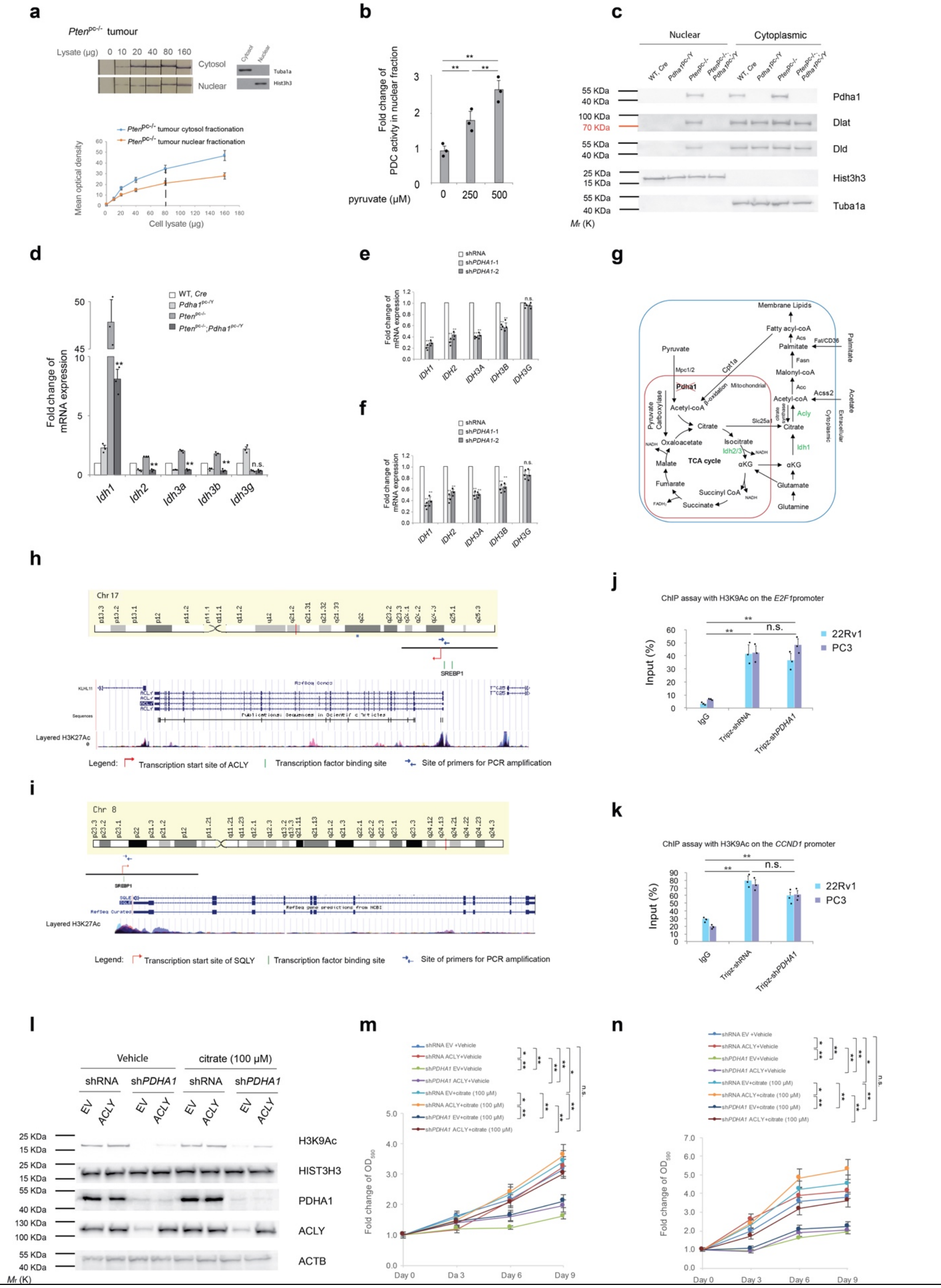

Supplementary Fig. 5

PDC controls histone acetylation and the expression of genes that link reductive carboxylation to lipogenesis.

(**a**) Upper left panel, PDC activity measurements of nuclear and cytoplasmic fractions of *Pten*$^{pc-/-}$ tumours loaded in different amount in standard dipstick assay. Upper right panel, fractionation was validated by western blot analysis for the indicated proteins. Lower panel, quantification of the optical density of dipstick bands from the upper left panel. The dash line represents the amount of lysate (80 µg) used in all the measurements performed in the paper, which fall in the linear range of the assay (n=3, independent prostate samples). Uncropped images are in Supplementary Figure 14. (**b**) PDC activity measurements in nuclear fractions of *Pten*$^{pc-/-}$ tumour cells incubated in presence of pyruvate at the indicated concentration in the activity buffer (n=3, independent prostate samples). (**c**) Western blot analysis of indicated proteins in nuclear and cytoplasmic fractions in wild type, *Pdha1*$^{pc-/Y}$, *Pten*$^{pc-/-}$ and *Pten*$^{pc-/-}$; *Pdha1*$^{pc-/Y}$ prostates and tumours (n=3, independent prostate samples). Uncropped images are in Supplementary Figure 14. (**d-f**) Quantitative real time-PCR analysis of mRNA expression for Isocitrate dehydrogenase isozymes in mouse prostate tissues of indicated genotypes (n=3, independent prostate samples) (**d**) and 22Rv1(**e**) and PC3(**f**) cells infected with sh*PDHA1* or scramble shRNA control (n=3, independent cell cultures). (**g**) Schematic overview of Pyruvate dehydrogenase, tricarboxylic acid cycle, β-oxidation, glutaminolysis and lipogenesis pathways (The green represents down-regulated genes). (**h,i**) Schematic overview of primer sites of for H3K9Ac and the binding of SREBP1 detection on the *ACLY* (**h**) and *SQLE* (**i**) promoters. H3K27Ac profile (UCSC Genome Browser on Human Feb. 2009 (GRCh37/hg19) Assembly) was used for prediction of H3K9Ac status. (**j,k**) Chromatin immunoprecipitation analysis of H3K9Ac levels on the promoter of *E2F1* (**j**) and *CCND1* (**k**) in 22Rv1 and PC3 cells infected with doxycycline-induced Tripz-sh*PDHA1* or scramble control (n=3, independent cell cultures). (**l**) Western blot analysis of indicated proteins in sh*PDHA1* or scramble control 22Rv1 cells infected with ACLY over-expressing lentivirus vector or empty vector control (EV) and treated with 100 µM citrate or vehicle over a 9-day period. Uncropped images are in Supplementary Figure 15. (n=3, independent cell cultures). (**m**,**n**) Relative cell number quantification by crystal violet staining of sh*PDHA1* or scramble control 22Rv1 (**m**) and PC3 (**n**) cells infected with ACLY over-expressing lentivirus vector or empty vector control (EV) and treated with 100 µM citrate or vehicle over a 9-day period (n=3, independent cell cultures). Error bars indicate s.e.m. $^*P < 0.05$; $^{**}P < 0.01$; n.s, not significant.

Supplementary Fig. 6

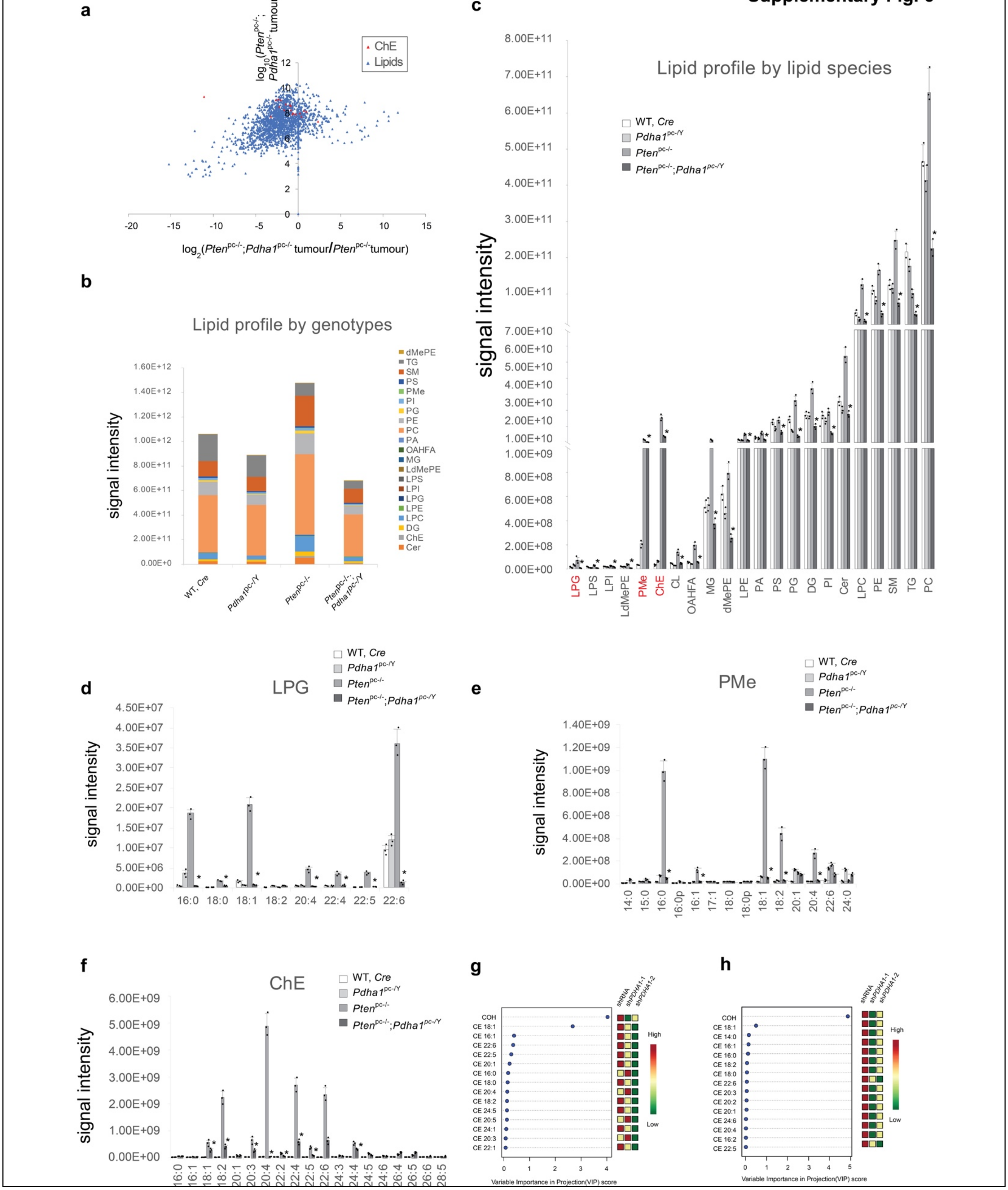

Supplementary Fig. 6

PDC inactivation reduces lipid and cholesterol levels in prostate cancer.

(**a**) A scatterplot Log$_{10}$ intensity of *Pten*$^{\text{pc-/-}}$; *Pdha1*$^{\text{pc-/Y}}$ tumours vs. Log$_2$ Ratio of *Pten*$^{\text{pc-/-}}$; *Pdha1*$^{\text{pc-/Y}}$ tumours versus *Pten*$^{\text{pc-/-}}$ tumours showing the distribution of 2,062 identified lipid ions (blue dots) including cholesterol esters (red dots) via LipidSearch from lipids extracted from three biological replicates of *Pten*$^{\text{pc-/-}}$; *Pdha1*$^{\text{pc-/Y}}$ tumours and *Pten*$^{\text{pc-/-}}$ tumours tissue extracts (~5 mg injected). ChE represents Cholesteryl esters (n=3, independent prostate samples) (**b,c**) The relative abundance of lipid species by intensity in wild type, *Pdha1*$^{\text{pc-/Y}}$, *Pten*$^{\text{pc-/-}}$ and *Pten*$^{\text{pc-/-}}$; *Pdha1*$^{\text{pc-/Y}}$ prostates and tumours (n=3, independent prostate samples). The top three lipids in fold change between *Pten*$^{\text{pc-/-}}$ tumours and wild type prostate were labeled as red. The lipid classes and abbreviations: Ceramide (Cer), Cholesteryl ester (ChE), Diradylglycerolipids (DG), lysophosphatidylcholine (LPC), lysophosphatidylethanolamine (LPE), lysylphosphatidylglycerol (LPG), lysophosphatidylinositol (LPI), lysophosphatidylserine (LPS), lysodimethylphosphatidylethanolamine (LdMeP), Monoradylglycerolipids (MG), (O-acyl)-omega-hydroxy fatty acids (OAHFA), phosphatidic acid (PA), phosphatidylcholine (PC), phosphatidylethanolamine (PE), Phosphatidylglycerol (PG), phosphatidylinositol (PI), phosphomonoesters (PMe), phosphatidylserine (PS), Sphingomyelin (SM), Triglyceride (TG), dimethylphosphatidylethanolamine (dMePE). (**d-f**) The relative abundance of lysylphosphatidylglycerol (LPG) (**d**), phosphomonoesters (PMe) (**e**), Cholesteryl ester (ChE) (**f**) species in wild type, *Pdha1*$^{\text{pc-/Y}}$, *Pten*$^{\text{pc-/-}}$ and *Pten*$^{\text{pc-/-}}$; *Pdha1*$^{\text{pc-/Y}}$ prostates and tumours (n=3, independent prostate samples). (**g,h**) Significantly changed levels of cholesterol (COH) and 14 Cholesteryl esters (CE) in 22Rv1 (**g**) and PC3 (**h**) cells infected with two sh*PDHA1* or a scramble shRNA control (n=3, independent cell cultures). The Variable Importance in Projection (VIP) scores depicting the top-ranked metabolites that contributed to the separation of prostate cancer cells infected with two sh*PDHA1* and a scramble control. A value of VIP score greater than 1 suggests actual contribution of the considered lipid to the group separation. The coloured boxes on the right indicate the relative concentrations of the corresponding metabolite in each group under study. The scale bar depicts the relative metabolite levels (red, high abundance; blue, low abundance). Error bars indicate s.e.m. *$P < 0.05$; n.s, not significant.

Supplementary Fig. 7

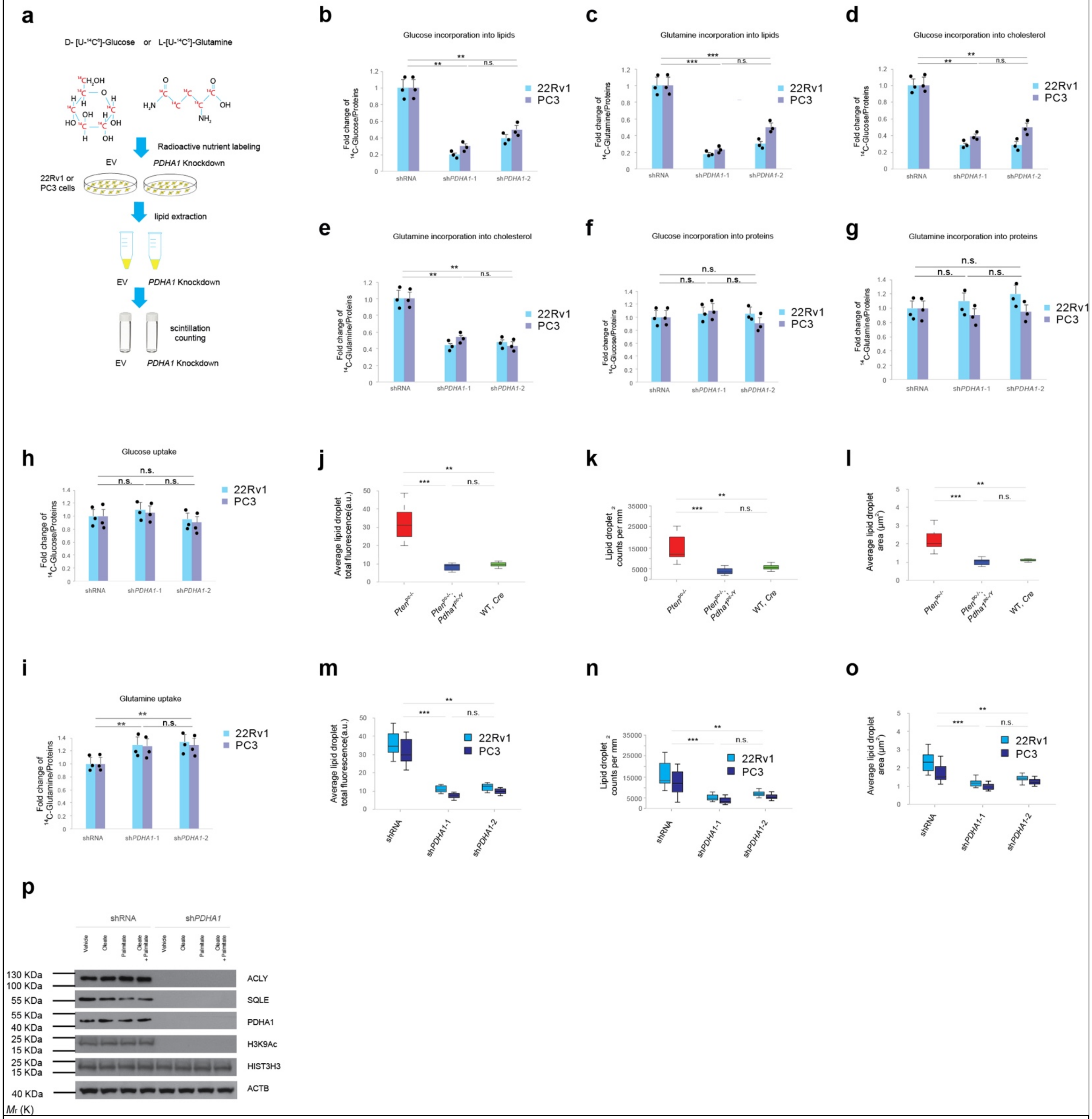

Supplementary Fig. 7

***Pdha1* inactivation mainly affects de novo lipid synthesis in prostate cancer.**

(**a**) Scheme of radioactive ^{14}C tracing using D- [U-$^{14}C_6$]-Glucose (^{14}C-Glucose) and L-[U-$^{14}C_5$]-Glutamine (^{14}C-Glutamine) measuring glucose and glutamine incorporation into lipids. (**b,c**) Radioactive tracing using ^{14}C-glucose (**b**) and ^{14}C-glutamine (**c**) for *de novo* lipogenesis in 22Rv1 and PC3 cells infected with two sh*PDHA1* and scramble shRNA control (n=3, independent cell cultures). (**d,e**) Radioactive tracing using ^{14}C- glucose (**d**) and ^{14}C-glutamine (**e**) for *de novo* cholesterol synthesis in 22Rv1 and PC3 cells infected with two sh*PDHA1* and scramble shRNA control (n=3, independent cell cultures). (**f,g**)Radioactive tracing using ^{14}C- glucose (**d**) and ^{14}C-glutamine (**e**) in protein synthesis in 22Rv1 and PC3 prostate cancer cell line infected with sh*PDHA1* or scramble shRNA control (n=3, independent cell cultures). (**h,i**) Glucose uptake (**h**) and glutamine uptake (**i**) analysis in 22Rv1 and PC3 cells infected with sh*PDHA1* or scramble shRNA control (n=3, independent cell cultures). (**j-l**) Confocal microscopy quantification of intra-tumour lipid droplets by average lipid droplets total fluorescence (a.u.) (**j**) average lipid droplets per mm^2 (**k**) and average lipid droplet area in µm^2 (**l**) in the indicated genotypes (n=3 independent prostate samples, 5 fields acquired for each group) in *Pten*$^{pc-/-}$; *Pdha1*$^{pc-/Y}$ versus *Pten*$^{pc-/-}$ prostate tumours. DAPI, blue. Scale bar: 20 µm (n=3 independent prostate samples, 5 fields acquired). (**m-o**) Confocal microscopy quantification of intra-tumour lipid droplets by average lipid droplet total fluorescence (a.u.) (**m**) average lipid droplets per mm^2 (**n**) and average lipid droplet area in µm^2 (**o**) in 22Rv1 and PC3 sh*PDHA1* and shRNA xenograft tumours. DAPI, blue. (n=3, independent prostate samples, 5 fields acquired and scale bar represents 20 µm). (**p**) Western blot analysis of indicated proteins in 22Rv1 cells infected with sh*PDHA1* or scramble control and treated with exogenous fatty acids in fatty acid-free media; oleate (25µM), palmitate (25 µM) or a combination of these two over a 6-day period. Uncropped images are in Supplementary Figure 15. (n=3, independent cell cultures). Error bars indicate s.e.m. $**P < 0.01$; $***P < 0.001$. n.s, not significant.

Supplementary Fig. 8

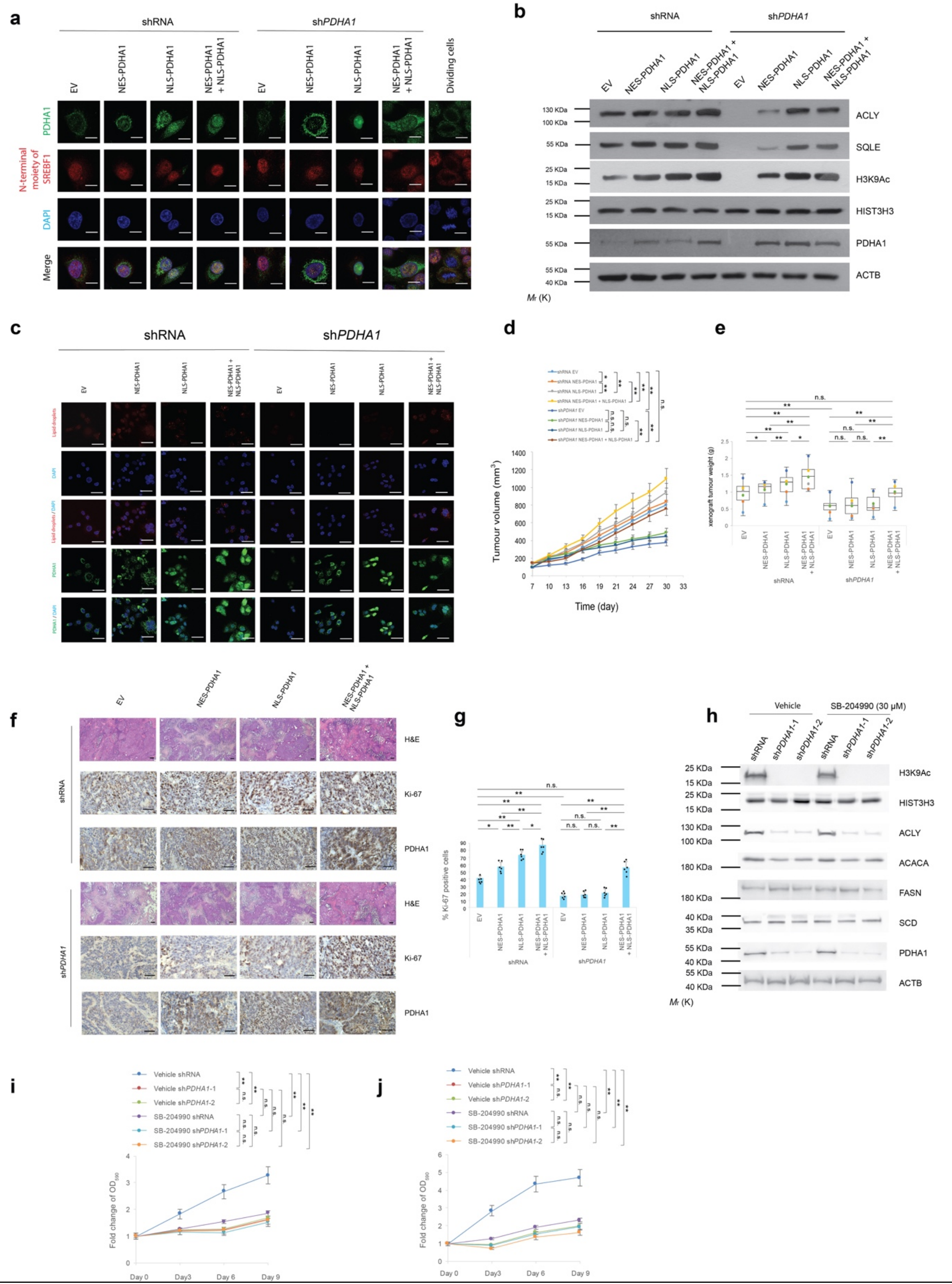

Supplementary Fig. 8

Both nuclear PDC and mitochondrial PDC are required for prostate cancer cell proliferation.

(**a-g**) Representative images of confocal microscopy for PDHA1 and the N-terminus mature form of SREBF1 (n=3, independent cell cultures, 5 fields acquired for each group and scale bar represents 10 μm) (**a**), western blot analysis of indicated proteins (n=3) (**b**), representative images of PDHA1 and lipid droplets in confocal microscopy. Uncropped images are in Supplementary Figure 15. (n=3, independent cell cultures, 5 fields acquired for each group and scale bar represents 50 μm) (**c**), evaluation of tumour formation in xenotransplantation experiments (n=6, independent tumour samples) (**d**), tumour mass in xenotransplantation experiments (n=6, independent tumour samples) (**e**), representative micrographs in histopathological analysis (haematoxylin/eosin staining and indicated proteins) in xenotransplantation experiments (n=6, independent tumour samples, 5 fields acquired for each group and scale bar represents 50 μm) (**f**) and quantification of the percentage of Ki-67 positive cells in xenotransplantation experiments (n=6, independent tumour samples) (**g**) of sh*PDHA1* or shRNA control 22Rv1 cells infected with NES-PDHA1, NLS-PDHA1 alone or in combination. (**h**) Western blot analysis of indicated proteins in the 22Rv1 cells infected with two shPDHA1 and a scramble shRNA control and treated with SB-204990, a selective ACLY inhibitors at the dose of 30 μM which effectively arrest cell growth as shown in panel (**i**) in this figure or vehicle for 9 days (n=3, independent cell cultures). Uncropped images are in Supplementary Figure 15. (**i**,**j**) the relative cell number quantification of the 22Rv1 cells (**i**) and PC3 cells (**j**) infected with two shPDHA1 and a scramble shRNA control and treated with SB-204990, a selective ACLY inhibitors at the dose of 30 μM for 9 days (n=3, independent cell cultures). Error bars indicate s.e.m. $^{*}P < 0.05$; $^{**}P < 0.01$. n.s, not significant.

Supplementary Fig. 9

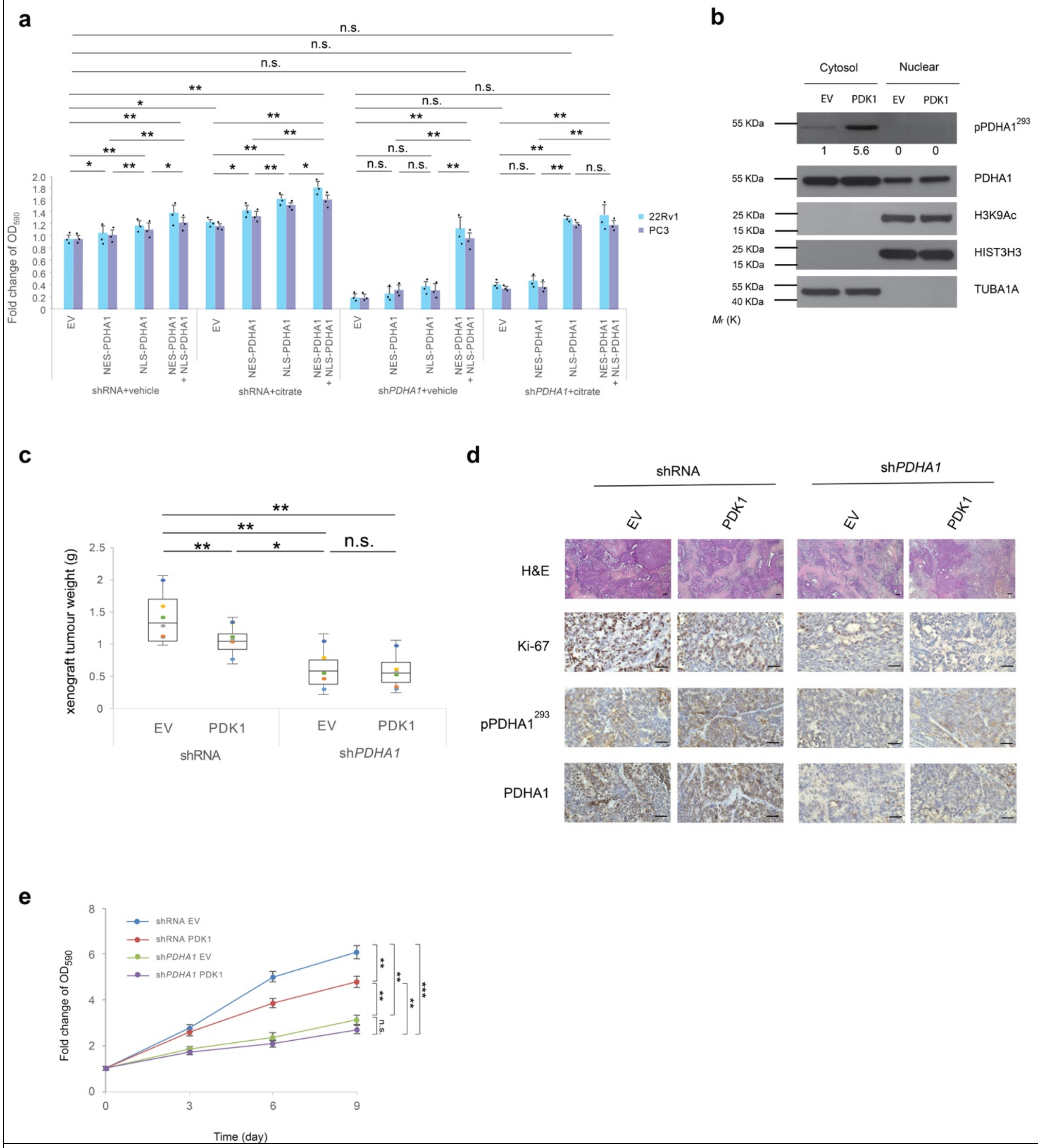

Supplementary Fig. 9

Mitochondrial PDC inhibition compromises prostate cancer cell proliferation by reducing citrate production.

(**a**) Relative cell number quantification by crystal violet staining of sh*PDHA1* or shRNA control 22Rv1 or PC3 cells infected with NES-PDHA1 and NLS-PDHA1 alone or in combination and treated with citrate (100 µM) or vehicle (n=3, independent cell cultures). (**b**) Western blot analysis of indicated proteins in nuclear and cytoplasmic fractions in 22Rv1 cells infected with PDK1 or empty vector control. Uncropped images are in Supplementary Figure 15. (n=3, independent cell cultures) (**c-e**) Tumour mass in xenotransplantation experiments (n=6, independent tumour samples) (**c**), representative micrographs in histopathological analysis (haematoxylin/eosin staining and indicated proteins) (n=6, independent tumour samples and scale bar represents 50 µm) (**d**) and relative cell number quantification by crystal violet (n=3, independent cell cultures) (**e**) of sh*PDHA1* or shRNA control 22Rv1 cells infected with PDK1 or empty vector control. Error bars indicate s.e.m. **P* < 0.05; ***P* < 0.01; ****P* < 0.001. n.s, not significant.

Supplementary Fig. 10

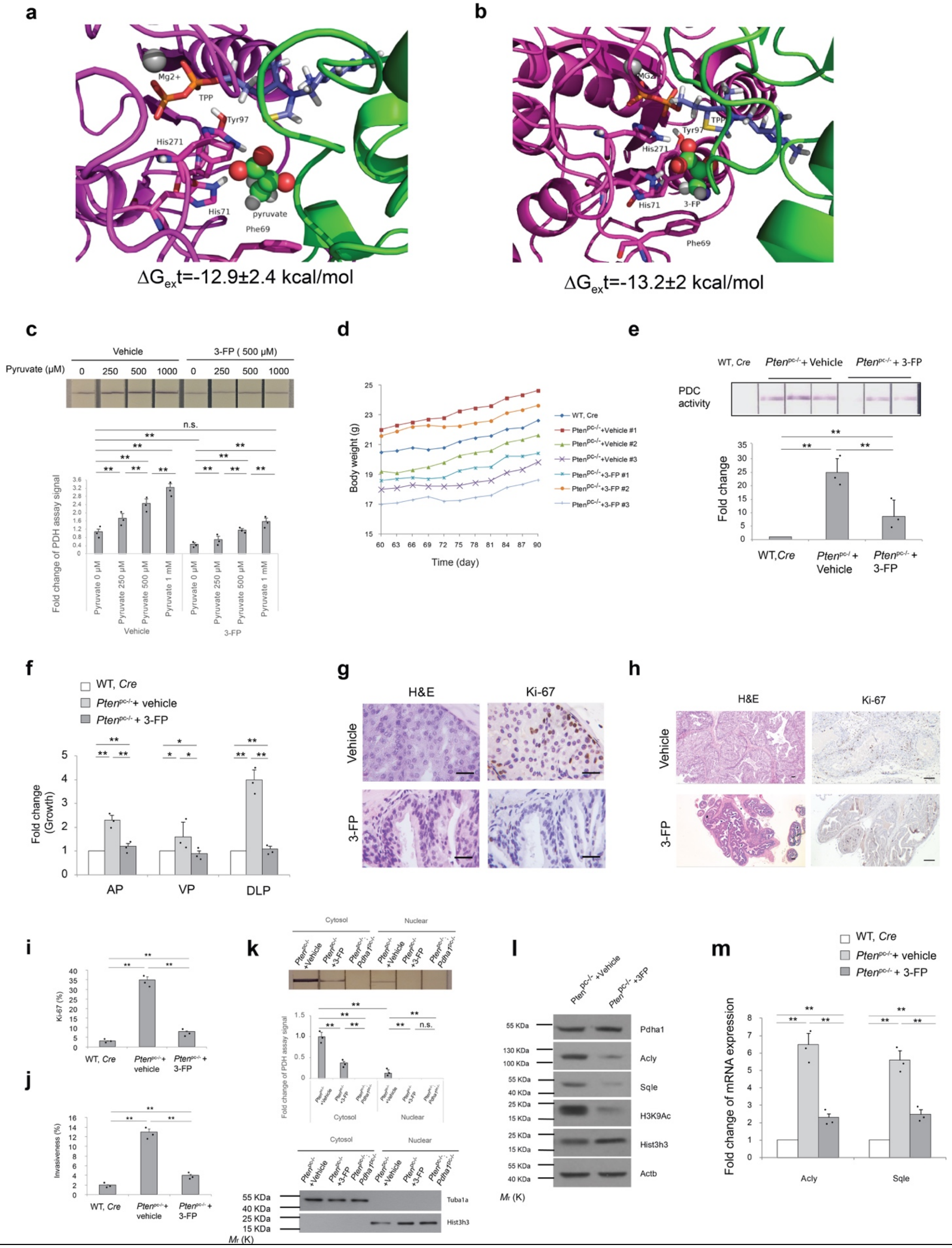

Supplementary Fig. 10

Pharmacological inhibition of PDHA1 arrests mouse and human prostate tumours.

(**a,b**) Representative structures, selected from MD simulations of the PDHA1/pyruvate (**a**) and PDHA1/3-FP (**b**) complexes. The a and b chains are represented as magenta and green ribbons, respectively. In the picture of PDHA1/3-FP complex, the fluorine atom is depicted in violet. Binding Delta G values, estimated by MM-GBSA, are also reported. (**c**) Upper panel, PDC activity measurements in the lysate from 22Rv1 cells treated with 3-FP or vehicle and supplemented with indicated amount of pyruvate in activity buffer of dipstick assay kit (n=3, independent cell cultures). Lower panel, quantification of PDC activity by mean optical density of colored bands shown on dipsticks in upper panel (n=3, independent cell cultures). (**d**) Body weight of mice of the indicated genotypes treated with 3-FP or vehicle from 8 weeks old for one month (n=3, independent mice). (**e**) Upper panel, PDC activity measurements, and quantification in anterior prostate of indicated genotypes from mice treated with 3-FP or vehicle from 8 weeks old for one month (n=3, independent prostate samples). Lower panel, quantification of PDC activity by mean optical density of colored bands shown on dipsticks in upper panel (n=3, independent prostate samples). (**f**) Comparison of prostate lobe volumes from male mice at age of 12 weeks treated with 3-FP or vehicle for one month (mm^3, 2 independent lobes per animal are presented. AP, anterior prostate; VP, ventral prostate; DLP, dorsal and lateral prostate, n=3, independent prostate samples). (**g-j**) Representative micrographs of histopathological analysis (haematoxylin/eosin and Ki-67 staining) of anterior prostates (AP) in *Pten*$^{pc-/-}$ prostate tumours (n=3, independent prostate samples, 5 fields, and scale bar represents 50 μm) (**g,h**), quantification of the percentage of Ki-67 positive cells (n=3 independent prostate samples, 5 fields) (**i**) and quantification of the percentage of invasive prostate cancer glands in *Pten*$^{pc-/-}$ prostate tissue (n=3, independent prostate samples, 5 fields) (**j**) from male mice at age of 8 weeks treated with 3-FP or vehicle for one month. (**k**) Upper panel, PDC activity measurements and quantification in nuclear and cytoplasmic fractions of prostate tumours of indicated genotypes from mice at age of 8 weeks treated with 3-FP or vehicle for one month (n=3, independent prostate samples). Lower panel, fractionation was validated by western blot analysis for the indicated nuclear and cytosolic proteins. Uncropped images are in Supplementary Figure 15. (**l**) Western blot analysis of indicated proteins in prostate tumours from *Pten*$^{pc-/-}$ mice at age of 8 weeks treated with 3-FP or vehicle for one month (n=3, independent prostate samples). (**m**) Quantitative real time-PCR analysis of mRNA expression for *Acly* and *Sqle* from mice of indicated genotypes at age of 8 weeks treated with 3-FP or vehicle for one month (n=3, independent prostate samples). Error bars indicate s.e.m. *$P < 0.05$; **$P < 0.01$. n.s, not significant.

Supplementary Fig. 11

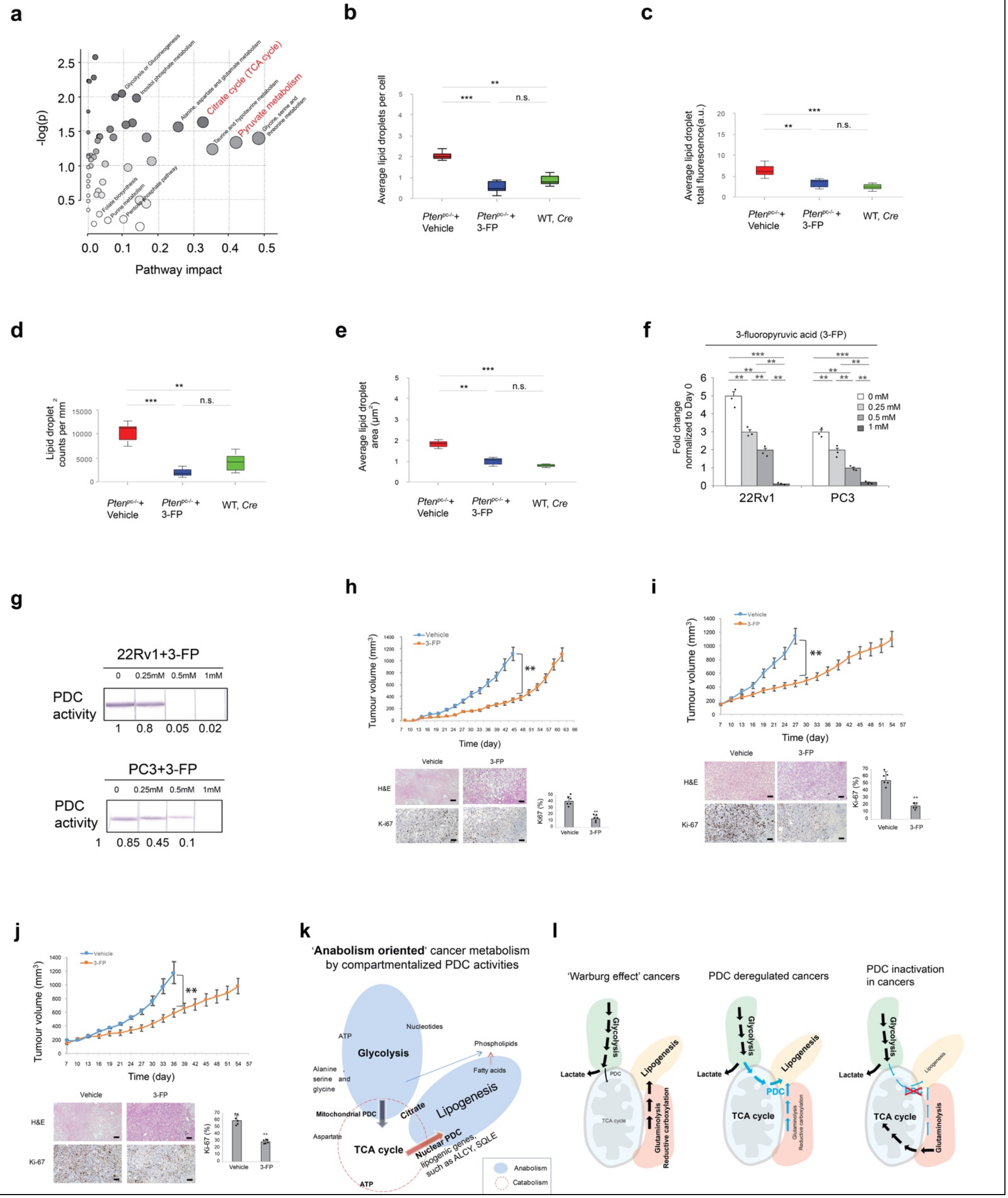

Supplementary Fig. 11

Pharmacological inhibition of PDHA1 arrests mouse and human prostate tumours.

(**a**) Integrating enrichment analysis and pathway topology analysis of metabolic pathways in prostate tumours from *Pten*$^{pc-/-}$ mice at age of 8 weeks treated with or without 3-FP for one month (n=3, independent prostate samples). (**b-e**) Quantification of confocal microscopy for lipid droplets (Lipidtox; red) by lipid droplet counts per cell (**b**), average lipid droplets fluorescence (a.u) (**c**), lipid droplet counts per mm^2 (**d**), average lipid droplets area in µm^2 (**e**) in wild type and *Pten*$^{pc-/-}$ prostate tissues from 8 weeks old male mice treated with 3-FP or vehicle for one month (n=3, independent prostate samples, 5 fields). (**f,g**) Relative cell number quantification by crystal violet staining (**f**) and PDC activity measurements (**g**) in indicated prostate cancer cell lines treated with 3-fluoropyruvic acid (3-FP) at the indicated concentration for 6 days (n=3, independent cell cultures). (**h-j**) Evaluation of tumour formation and quantification of the percentage of Ki-67 positive cells in xenotransplantation experiment in LNCaP (**h**), 22Rv1 (**i**) and PC3 (**j**) cells treated with 3-FP or vehicle for two months (n=6, independent tumour samples, 5 fields and scale bar represents 50 µm). (**k**) Schematic representation of the role of mitochondrial and nuclear PDH complex functions in regulating glucose influx of TCA cycle and controlling the diversion of TCA cycle intermediates (or glutamine derived anaplerosis pathway) into lipogenesis. (**l**) Metabolic landscape describing the functional relevance of PDC complex in regulating non-canonical tumour metabolism. Contrast to classic ‘Warburg effect' where cancers rely predominantly on glycolysis and catabolic TCA cycle gets restrained, tumours could achieve another ‘anabolism oriented' reprogramming/axis by upregulating PDC and promoting PDC nuclear translocation. Nuclear PDC controls the transitory process in TCA cycle by allowing the short-lived entry and exit of carbon pool in mitochondria to fuel citrate synthesis and lipogenesis. Taking advantage of this diversion caused by nuclear PDC, the tumour cells reduce carbon consumption in TCA cycle thereby benefiting proliferation. PDC inactivation arrests nuclear PDC active cancers by abrogating both glucose influx and potential anaplerosis pathways from reductive carboxylation and glutaminolysis. The blue represents the pathways controlled by PDC. Error bars indicate s.e.m. **$P < 0.01$; ***$P < 0.001$. n.s, not significant.

Supplementary Fig. 12

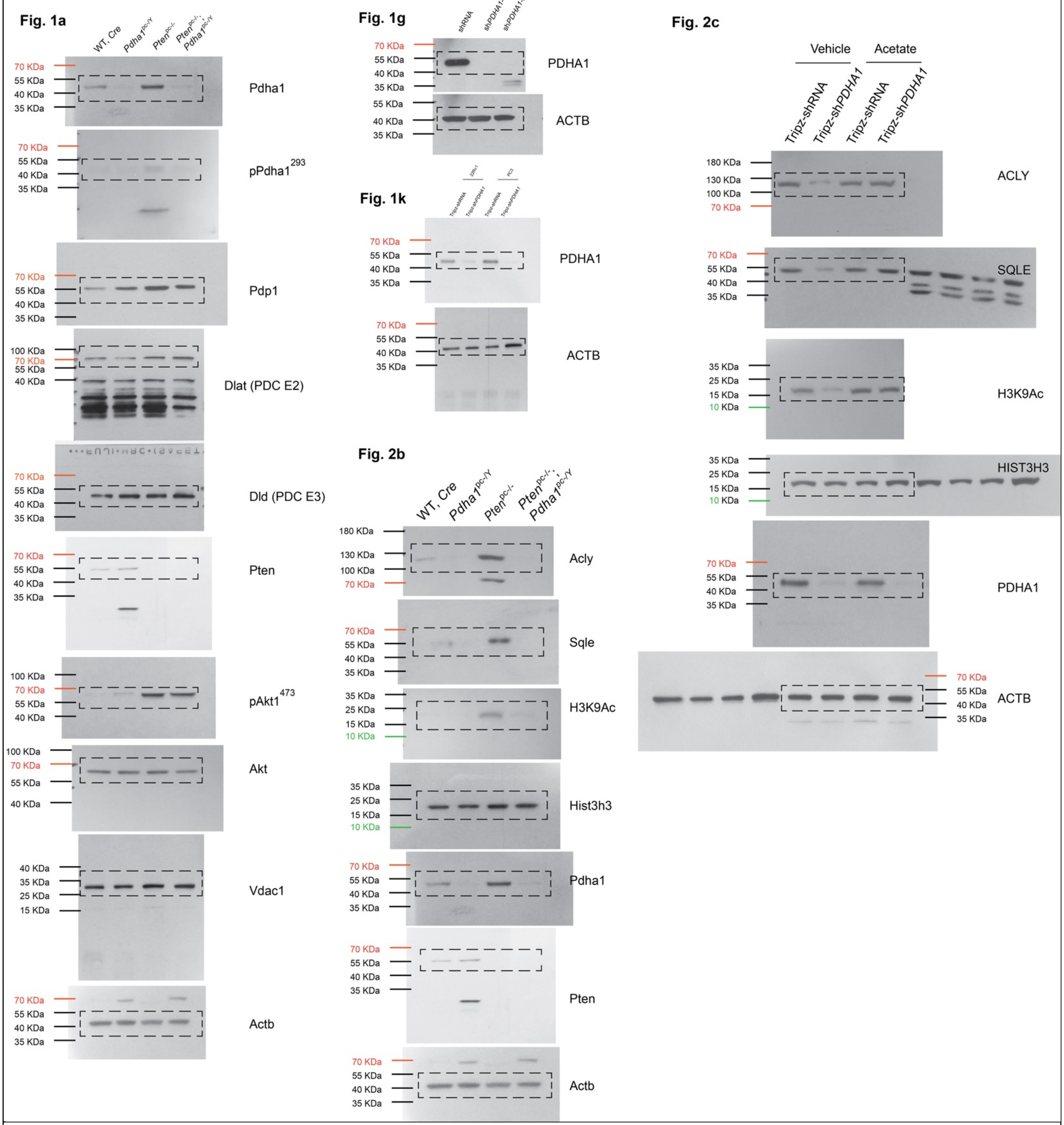

Supplementary Fig. 12

Uncropped full-length pictures of Western blotting membranes presented in the main Fig. 1a, 1g, 1k, 2b and 2c

Membranes were often cut to enable blotting for multiple antibodies

Supplementary Fig. 13

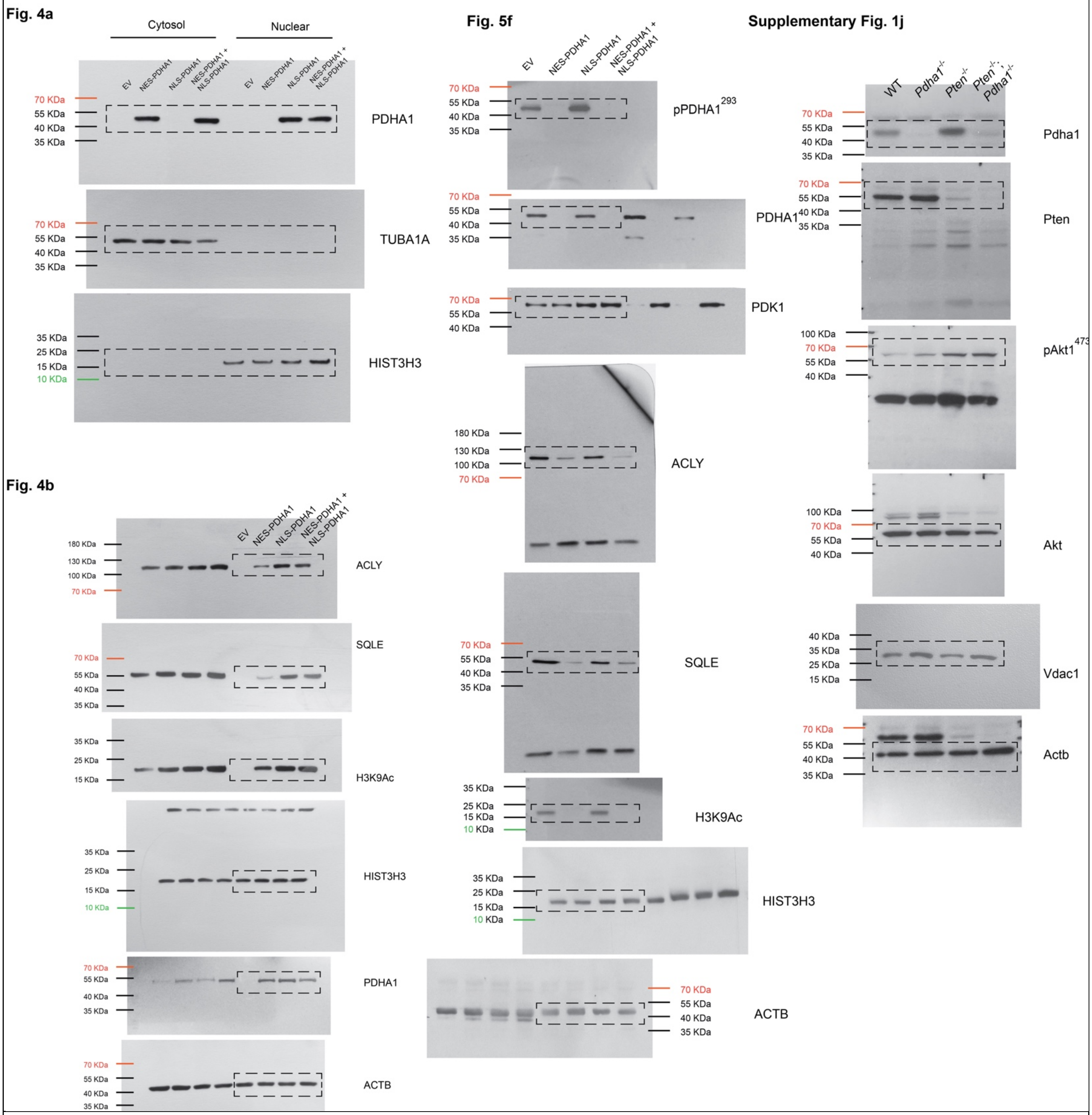

Supplementary Fig. 13

Uncropped full-length pictures of Western blotting membranes presented in the main Fig. 4a, 4b, 5f and Supplementary Fig. 1j
Membranes were often cut to enable blotting for multiple antibodies

Supplementary Fig. 14

Supplementary Fig. 3f

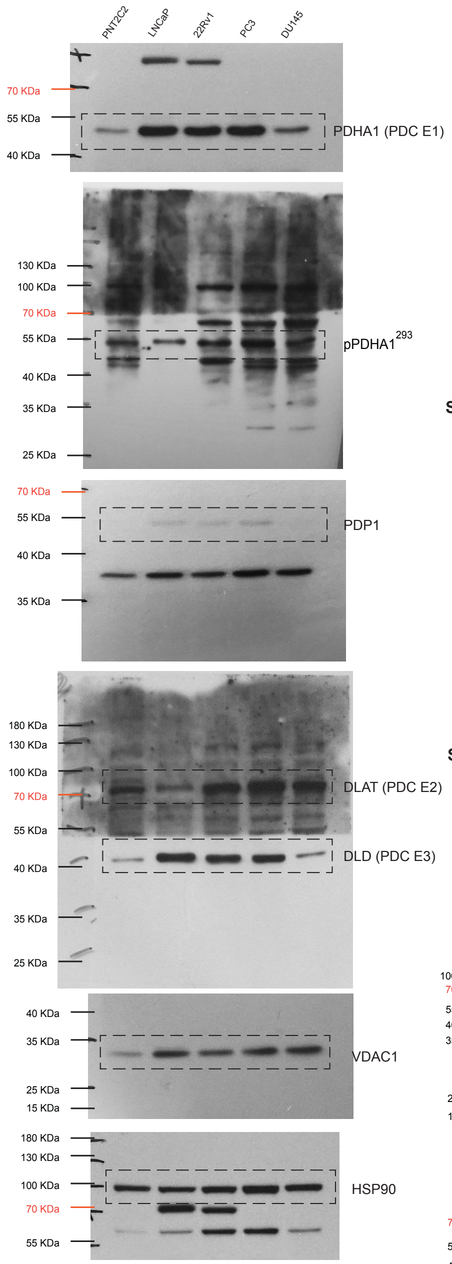

Supplementary Fig. 3m

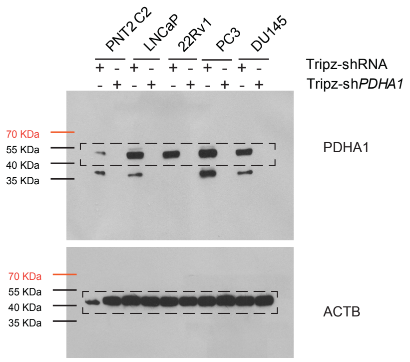

Supplementary Fig. 5a

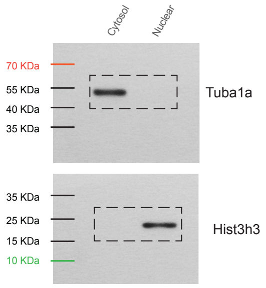

Supplementary Fig. 5c

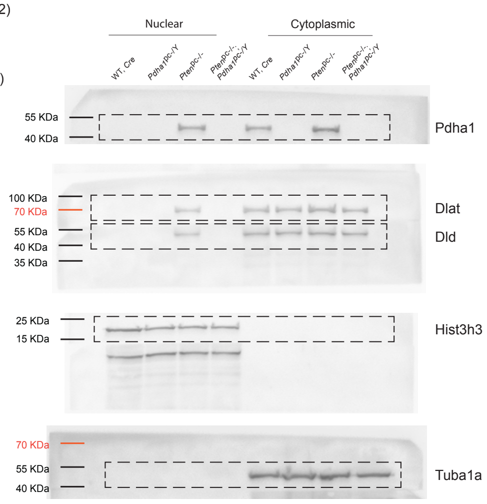

Supplementary Fig. 14
Uncropped full-length pictures of Western blotting membranes presented in the Supplementary Fig. 3f, 3m, 5a and 5c
Membranes were often cut to enable blotting for multiple antibodies

Supplementary Fig. 15

Supplementary Fig. 5l

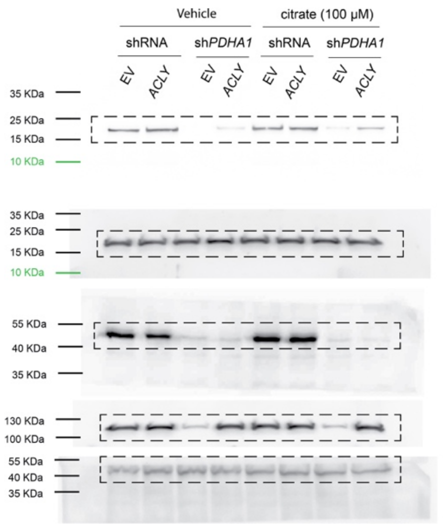

Supplementary Fig. 8b

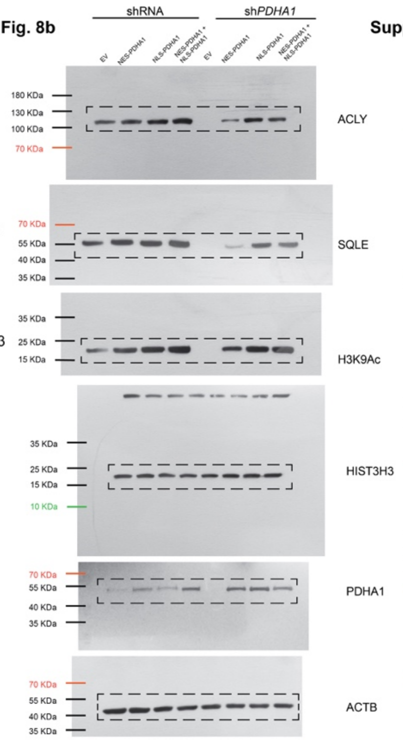

Supplementary Fig. 9b

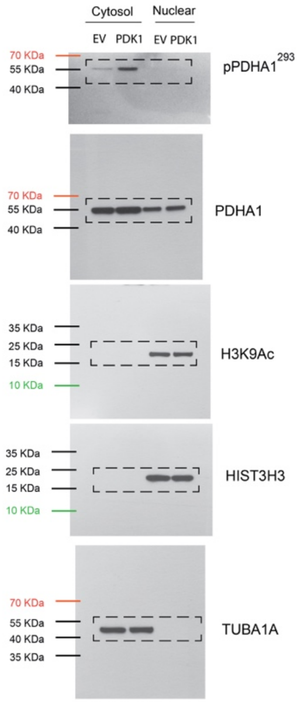

Supplementary Fig. 7p

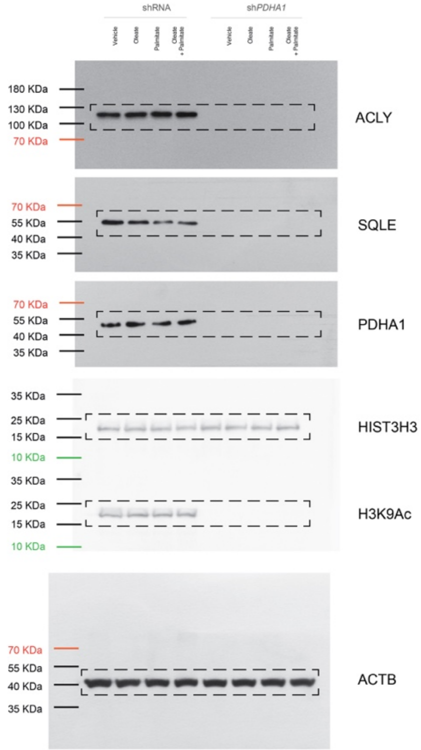

Supplementary Fig. 8h

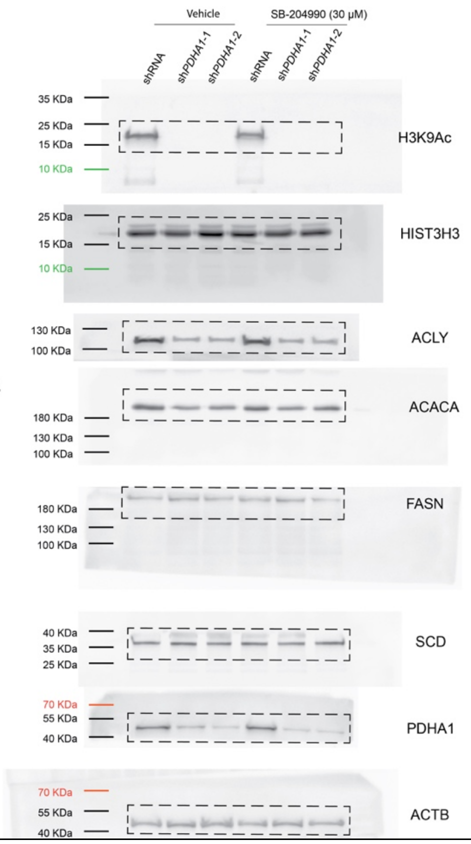

Supplementary Fig. 10k

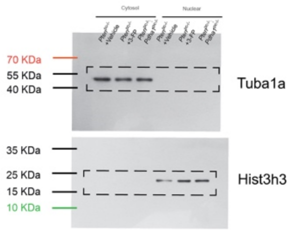

Supplementary Fig. 15
Uncropped full-length pictures of Western blotting membranes presented in the Supplementary Fig. 5l, 7p, 8b, 8h, 9b and 10k
Membranes were often cut to enable blotting for multiple antibodies

6. Materials and Methods

Animals

All mice were maintained under specific-pathogen-free conditions in the animal facilities of the IRB Institute, and experiments were performed according to state guidelines and approved by the local ethics committee. The *Pten*$^{\mathrm{loxP}}$ and *Pdha1*$^{\mathrm{loxP}}$ conditional knockout alleles have been described[15,18]. Female *Pten*$^{loxP/loxP}$; *Pdha1*$^{loxP/Y}$ mice were crossed with male *Probasin-Cre4 (Pb-Cre4)* transgenic mice[14] for the prostate-specific deletion of *Pten* and *Pdha1*. For genotyping, tail DNA was subjected to polymerase chain reaction analysis with the primers listed in Supplementary Table 1. Mice of correct genotypes were randomly chosen and allocated into experimental groups. For the transgenic mice, the experiment was carried on in single blind.

Cell culture and reagents

Human prostate carcinoma cell lines, 22Rv1, LNCaP, PC3, and DU145 were purchased from American Type Culture Collection (ATCC) and human prostate epithelial PNT2C2 cell line[55] was gifted from Prof. Norman James Maitland, University of York and kept in Institute of Oncology Research (IOR) in Bellinzona, Switzerland. The cells were cultured in RPMI medium 1640 (Catalog# 21875034, Thermo Fisher Scientific) with 10% fetal bovine serum (FBS) (Catalog# 10500-064, Thermo Fisher Scientific), 10,000 I.U./mL Penicillin and 10,000 (μg/mL) Streptomycin (Catalog# P4333-20ML, Sigma) under the condition of 37 ℃ and 5% CO_2. Cells were transduced with TRIPZ doxycycline inducible lentiviral construct against human PDHA1 gene (Catalog# V2THS_75677, Dharmacon) and TRIPZ Inducible Lentiviral Empty Vector shRNA Control (Catalog# RHS4750, Dharmacon). Flat bottom ultra low attachment multiple well plates (Catalog# 3473, Corning) were used for sphere formation assay. Cells were transduced with pLKO lentiviral constructs against human *PDHA1* gene (Catalog# SHCLNG-NM_000284, Sigma, clone# sh*PDHA1*-1: TRCN0000028582 and sh*PDHA1*-2: TRCN0000028627) and Lentiviral Empty Vector shRNA Control (Catalog# SHC002, Sigma). PDHA1 was PCR-amplified from complementary DNA of a normal human prostate sample. For the overexpression of cytosol and nuclear-localized PDHA1, nuclear export signal (NES) or nuclear localization signal (NLS) was fused PDHA1 as NES-PDHA1 and NLS-PDHA1. NES-PDHA1 and NLS-PDHA1 constructs were engineered as sh-*PDHA1* (Catalog# SHCLNG-NM_000284, Sigma, clone# sh*PDHA1*-1: TRCN0000028582) resistant vectors. NES-PDHA1 and NLS-PDHA1 were cloned into pLenti CMV Neo (Addgene) and the empty vector was used as a control. Cells were infected shRNA control or sh*PDHA1* and overexpressed PDK1 by pLZRS-PDK1-IRES-puro or FG12-eGFP control[19] (gifted from Prof. Daniel Peeper, The Netherlands Cancer Institute). Lentiviral and retroviral infections were performed using HEK293T cells and Phoenix cells, respectively, as producers of viral supernatants. Primary MEFs were derived from littermate embryos and obtained by crossing *Pdha1*$^{\mathrm{loxP/loxP}}$ or *Pten*$^{\mathrm{loxP/loxP}}$ animals. Embryos were harvested at 13.5 days post coitum, and individual MEFs were produced and cultured as previously described[14-16]. For senescence experiments, MEFs were infected with pMSCV hygro-Cre (Plasmid #34565, Addgene) or empty vector control (pMSCV hygro) retrovirus, selected pharmacologically in hygromycin (50 µg/mL, Catalog# H0654-250MG, Sigma) for 48 hr. After selection, cells were seeded and analyzed for SA-β-gal activity (Catalog #9860, Cell Signaling Technology). Cell number quantification with crystal violet was performed as referenced[15]. The chemicals used for cell and tumour treatments were purchased from Sigma: Doxycycline hyclate (Catalog# D9891-1G, Sigma) and β-Fluoropyruvic acid sodium salt monohydrate (3-Fluoropyruvate, 3-FP, Catalog #F4004, Sigma). SB-204990 (Catalog# 4962, Bio-Techne AG). For the xenograft experiments, 2×10^6 22Rv1 cells infected Tripz-sh*PDHA1* or Tripz-shRNA control were injected subcutaneously (s.c.) into the lower flank of the same nude mouse on different sides. The mice started to be fed with Doxycycline (0.2 g/L) water supplemented with 5% sucrose in another day. Tumour formation from each individual injection was monitored every three days until the 22nd day of experimental termination. 2×10^6 22Rv1 cells infected shRNA control or sh*PDHA1* and overexpressed PDK1 by pLZRS-PDK1-IRES-puro or FG12-eGFP control[19] (gifted from Prof. Daniel Peeper, The Netherlands Cancer Institute) were injected subcutaneously (s.c.) into the lower flank of the same nude mouse on different sides. Tumour formation from each individual injection was monitored every three days until the 30th day of experimental termination. For experiments with xenograft, mice were excluded when the tumour size exceeded the average tumour size at the moment of randomization. The experiments with Xenograft (including tumour measurements) were carried on in single blind. For preclinical treatment on *Pten*$^{pc-/-}$ males, 80 mg/Kg of 3-FP were intraperitoneally injected every three days on mice of ages at 8 weeks to 12 weeks. For the xenograft tumours treated with 3-FP or vehicle control, 2×10^6 LNCaP, PC3, and 22Rv1 cells were injected subcutaneously (s.c.) into the lower flank of the nude mice. The treatment started when tumour size reached 100 mm^3 and the treatment continued for a period of two months. When the mice were sacrificed, tumours were disserted and analyzed. Mice were fasted for 6 h prior to tissue harvest (9 am-3 pm) in order to prevent metabolic alterations due to immediate food intake.

Real-time PCR, western blotting, and immunohistochemistry

RNA was extracted using TRIzol® Plus RNA Purification Kit (Catalog# 12183555, Life technologies). 1 µg of total RNA was used for cDNA synthesis using SuperScript® III Platinum® One-Step qRT-PCR Kit (Catalog# 11732-020, Life technologies). Quantitative Real Time PCR (q-RT PCR) was performed as previously described[15]. Primers employed are detailed in Supplementary Table 2. All qRT-PCR data presented was normalized using β-actin. Tissue and cell lysates were prepared with RIPA buffer (1× PBS, 1% NP-40, 0.5% sodium deoxycholate, 0.1% SDS and protease inhibitor cocktail (Catalog# 78429, Thermo Scientific)). The following antibodies were used for western blotting: rabbit polyclonal anti-Pten antibody (Catalog # 9552, Cell Signaling Technology), mouse monoclonal anti-PDHA1 antibody (Catalog # 459400, Invitrogen), rabbit polyclonal anti-phospho-PDHE1-A type I (Ser293) antibody (Catalog# ABS204, EMD Millipore), goat polyclonal anti-PDC-E2 Antibody (N-20) (Catalog# sc-16890, Santa Cruz Biotechnology), mouse monoclonal anti-DLD Antibody (E-3) (Catalog# sc-376890, Santa Cruz Biotechnology), rabbit polyclonal anti-PDP1 antibody (Catalog# HPA019081, Sigma), rabbit polyclonal anti-Akt antibody (Catalog# 9272, Cell Signaling Technology), rabbit monoclonal anti-p-Akt Ser473 antibody (Catalog# 4060, Cell Signaling Technology), rabbit monoclonal anti-Acetyl-Histone H3 (Lys9) antibody (Catalog# 9649, Cell Signaling Technology), rabbit monoclonal anti-Histone H3 antibody (Catalog# 4499, Cell Signaling Technology), rabbit polyclonal anti-ACLY antibody (Catalog# 4332, Cell Signaling Technology), goat polyclonal anti-SQLE antibody (Catalog# sc-49754, Santa Cruz Technology), rabbit monoclonal anti-VDAC1 (Catalog# 4661, Cell Signaling Technology), rabbit polyclonal anti-α-Tubulin antibody (Catalog# 2144, Cell Signaling Technology) and mouse monoclonal anti-β-actin (Catalog# A5316, Sigma). For immune-histochemistry (IHC), tissues were fixed in 10% formalin and embedded in paraffin in accordance with standard procedures. Sections were stained with Rabbit polyclonal anti-PTEN antibody (Catalog# 51-2400, Thermo Fisher Scientific), mouse monoclonal anti-PDHA1 (Catalog# 459400, Invitrogen), rabbit polyclonal Anti-PDP1 (Catalog# HPA019081, Sigma), anti-Ki-67 (clone SP6, Lab Vision), or anti-cleaved-caspase-3 (Catalog#9661, Cell Signaling Technology) antibodies. Prostate disease spectrum tissue array, including TNM, clinical stage and pathology grade, 80 cases/80 cores were purchased from US Biomax, Inc, (Catalog# PR8011a) and prostate cancer tissue array, including TNM, clinical stage and pathology grade, 48 cases/48 cores was purchased from US Biomax, Inc (Catalog# PR483b). Ki-67 and gland invasiveness assessment was performed by three prostate pathologists independently, in a blinded manner.

Gene Expression Analysis

Gene expression profiling (GEP) was done using the MouseRef-8 v2.0 Expression BeadChip (Illumina, San Diego, CA, USA), following the manufacturer's protocol. Arrays were read on an Illumina HiScanSQ system. Data were first extracted with the Illumina GenomeStudio software and then imported in Genomics Suite 6.4 (Partek Incorporated, Saint Louis, MO USA) and quantile normalized. Transcripts with differences in expression were identified by ANOVA. Enrichment analysis was performed using Gene Set Enrichment Analysis (GSEA) [56]. Raw data have been deposited in National Center for Biotechnology Information's Gene Expression Omnibus (GEO) and are accessible through GEO accession no. GSE74245. GSEA was performed on entire gene list ranked according to fold changes observed between *Pten*$^{pc-/-}$ and *Pten*$^{pc-/-}$; *Pdha1*$^{pc-/Y}$ mice. The GS collection assessed includes all GSs smaller than 10 and larger than 500 (8335 out of 22423 GSs retained) compiled according to[57] the 24.03.15. GSs yielding significance (($FDR < 0.05$; nominal $p\text{-value} < 0.005$; $TAGS \geq 50\%$) were retained and assessed for their role in metabolic processes after visualizing the data as described [58]. For the 3 relevant clusters identified, their GSs' FDR q-values were, together with unaffected metabolic processes log2 transformed and inversed for display in Fig. 2a.

Chromatin immunoprecipitation

ChIP assays were performed with approximately 6×10^6 cells per experiment. Cells were subject to hypotonic lysis and treated with micrococcal nuclease to recover mono- to tri-nucleosomes. Nuclei were lysed by brief sonication and dialysed into N-ChIP buffer (10 mM Tris pH 7.6, 1 mM

EDTA, 0.1% SDS, 0.1% Na-Deoxycholate, 1% Triton X-100) for 2 h at 4 °C. Soluble material was incubated overnight at 4 °C after addition of 0.5–1 μg of antibody bound to 25 μl protein A Dynal magnetic beads (Catalog# 10006D, Invitrogen), with 5% kept as input DNA. Magnetic beads were washed, chromatin was eluted and ChIP DNA was dissolved in 10 mM Tris pH 8 for quantitative PCR reactions (see later). Three separate ChIP experiments were performed on replicate biological samples. The data shown are the average qRT–PCR values (n =3). Primers are listed below. All qPCR was performed using an Applied Biosystems StepOnePlus system and Power SYBR Green PCR master mix. ChIP samples were diluted 1:100 in H_2O and 5 μl was used per reaction. ChIP-qPCR signals were calculated as per cent input. Primers used in ChIP were listed in supplementary table 3.

Subcellular fractionation

Nuclear and cytoplasmic fractionation was performed by centrifugation technique as described previously[59]. Nuclear and cytoplasmic extracts were made using NE-PER Nuclear and Cytoplasmic Extraction Reagent Kit (Catalog# 78833, Pierce Biotechnology). Total cell lysate was prepared in radioimmunoprecipitation assay buffer (RIPA; 25 mmol/L Tris (pH 7.4), 150 mmol/L KCl, 5 mmol/L EDTA, 1% NP40, 0.5% sodium deoxycholate, and 0.1% SDS) with protease inhibitor cocktail (Catalog# 88688, Thermo Scientific). Proteins at the same amount were separated by 10% to 15% SDS-PAGE and transferred onto polyvinylidene difluoride membranes. For each fraction, nuclear protein histone 3 (Catalog# 4499, Cell Signaling Technology) and cytoplasmic protein α-Tubulin (Catalog# 2144, Cell Signaling Technology) were used to show clear isolation between nucleus and cytoplasm during fractionation.

Targeted mass spectrometry analysis

For mouse prostate tissues, 500 µL of 80% LC-MS grade methanol was added to each approximately 15 mg sample and incubated at -80°C for 15 min. Tissue samples collected were centrifuged at 18, 470g for 5 min in a cold room to pellet cell debris and proteins. Supernatants were saved. Pellets were resuspended in 500 µl 80% methanol by vortexing and subsequently centrifuged as before. Supernatants were centrifuged one final time at 18, 470g for 10 min at 4°C. Metabolite extractions were dried to a pellet by SpeedVac with no heat. Samples were re-suspended using 20 µL LC-MS grade water and 10 µL was injected and analyzed using a 5500 QTRAP hybrid triple quadrupole mass spectrometer (AB/SCIEX) coupled to a Prominence UFLC HPLC system (Shimadzu) through selected reaction monitoring (SRM). Two hundred and sixty-one endogenous water-soluble metabolites were targeted for steady-state analyses of samples. Some metabolites were targeted in both the positive and negative ion mode through a positive/negative polarity switching for a total of 296 SRM transitions. The ESI voltage was +4900V in the positive ion mode and -4500V in the negative ion mode. The dwell time was 3ms per SRM transition and the total cycle time was ~1.56 sec. Approximately 10-12 data points were acquired per detected metabolite. Samples were delivered to the MS through normal-phase chromatography using a 4.6mm i.d ×10 cm Amide XBridge HILIC column (Waters Corp.) at 350 µl min^{-1}. Gradients were run starting from 85% buffer B (HPLC grade acetonitrile) to 35% B from 0-3.5 min; 35% B to 2% B from 3.5-11.5 min; 2% B was held from 11.5-16.5 min; 2% B to 85% B from 16.5-17.5 min; 85% B was held for 7 min to re-equilibrate the column. Buffer A was comprised of 20mM ammonium hydroxide/20mM ammonium acetate (pH 9.0) in 95:5 water/acetonitrile. Peak areas from the total ion current for each metabolite SRM transition were integrated using MultiQuant v2.1 software (AB/SCIEX). Metabolomics data analysis was done in part using Metaboanalyst 2.0 software (www.metaboanalyst.ca).

Isotope Labeling and stationary Profiling

Fresh transgenic mouse tumour tissues were mechanically dissociated, enzymatically digested and filtered to obtain a single-cell suspension as described[60]. Single cells were stained with fluorescein isothiocyanate (FITC)-anti-CD34 (Catalog# 560238, BD Biosciences) for stroma cells, FITC-anti-Ter119 (Catalog# 557915, BD Biosciences) for erythrocytes, FITC-anti-CD31(Catalog# 561813, BD Biosciences) for endothelial cells, and FITC-anti-CD45 (Catalog# 553079, BD Bioscience) for leukocytes and incubated 20 min on ice. All antibodies (BD Biosciences) were used at 1:300; cells were then loaded into MS column with Anti-FITC MicroBeads (Catalog# 130-048-701, Miltenyi Biotec) for MACS separation, and unstained epithelial cells were collected in the negative fraction. For steady state metabolomic analysis[5], prostate epithelial cells derived from transgenic mouse tumours were plated to ~80% confluence on 10 cm dishes in biological quadruplicate. cells were plated in RPMI medium (Catalog# 11875093, Thermo Scientific) was supplemented with 10% dialyzed serum and devoid of glucose or glutamine and supplemented with one of the two carbon-13-labelled substrates [U-$^{13}C_6$]-glucose and [U-$^{13}C_5$] glutamine (Catalog# CLM-1396-1 and CLM-1822-H-0.25, Cambridge Isotope Labs) where the remaining substrates were unlabelled (glucose 11 mM and glutamine 2 mM). Fatty acid oxidation studies[20] were conducted using [U-$^{13}C_{16}$] palmitate (Catalog# CLM-6059-1, Cambridge Isotope Labs) noncovalently bound to fatty acid-free BSA. [U-$^{13}C_{16}$] palmitate-BSA was added to culture medium at 5% of the final volume (50 mM final concentration) with 1 mM carnitine in medium formulated with delipidated FBS (Catalog# 12676011, Thermo scientific). Additionally, fresh media containing carbon-13-labelled substrates was exchanged 2 h prior to metabolite extraction for steady state analyses. Considering primary epithelial cells isolated from mouse prostate tissue do not attach and fit for long term culture, we labeled these epithelial cells for 6 h and we did not see the difference compared to the results from labeling for 24 h. After 6 h of incubation with labelled substrates, metabolite extraction of medium was performed by adding 1mL cold (–80 °C) 80% methanol (Catalog#34966-1L and 14263-1L, Sigma), incubated at −80 °C for 30 min followed by centrifugation at 10,000g for 10 min at 4 °C. The resultant supernatant was lyophilized by speedvac and stored at − 80 °C until analysis. Dried metabolite pellets were re-suspended in 20 µL LC–MS grade water, 5 µL was injected onto a Prominence UFLC and separated using a 4.6 mm i.d. Å~ 100 mm Amide XBridge HILIC column at 360 µL per minute starting from 85% buffer B (100% ACN) to 0% B over 16 min. Buffer A: 20 mM NH_4OH/ 20 mM CH_3COONH_4 (pH = 9.0) in 95:5 water/ACN.287 selected reaction monitoring (SRM) transitions were captured using positive/ negative polarity switching by targeted LC-MS/MS using a 5500 QTRAP hybrid triple quadrupole mass spectrometer. As for metabolomics, the quantity of the metabolite fraction analyzed was adjusted to the corresponding protein concentration from a sample processed in parallel. The analysis was performed for each of the three substrates on three independent tumours in biological triplicate.

Lipidomics analysis on transgenic mouse prostate tumours

~ 5 mg of solid tissue was snap frozen in liquid nitrogen (−196°C) as close to the time of resection as possible. Chloroform: methanol (2:1 ratio) was added to a final volume 20 times the volume of the biological sample (100 µL in 2 mL of solvent mixture) in a 12 mL glass vial. The mixture was agitated for 30 min in an orbital shaker at room temperature. 0.2 volume parts of water (400 µL for 2 mL) was added and the mixture was vortexed for 1 min. The mixture was placed still for 10 min and centrifuge at low speed (1000 g) to separate into three phases. The upper aqueous phase was kept (optional) to analyze small organic polar molecules. The middle layer contains protein, DNA, and polar large molecules. The lower phase containing non-polar lipids was collected and evaporated under vacuum using a SpeedVac rotary evaporator or under a nitrogen stream. 10 µL of sample was injected onto LC-MS/MS using a hybrid QExactive Plus Orbitrap mass spectrometer in DDA mode using positive/negative ion polarity switching (Top 8 in both modes). Using a 100 mm x 2.0 mm C18 column at 260 µL/min with a 1100 quaternary HPLC, lipids were eluted over 20 min. from 32% B buffer (90% IPA/10% ACN/10 mM NH_4HCO_2/0.1% FA) to 97% B. A buffer consisted of 59.9% ACN/40% water/10 mM NH_4HCO_2/0.1% FA. Lipid molecules were identified and quantified using LipidSearch 4.1.9 software[61].

Statistics

For each independent *in vitro* experiment, at least three technical replicates were used (exceptions: in western blot analysis technical replicates are presented, in targeted metabolomics three technical replicates were used. For data mining analysis, Analysis of variance (ANOVA) test was used for multi-component comparisons and Student T test for paired-comparisons. In the *in vitro* experiments, data groups were assessed for normal distribution and Student T test was applied for paired-comparison. Data represent mean ± s.e.m. of pooled experiments unless otherwise stated. n values represent the number of experimental samples and all the experiments were repeated at least three times. For *in vivo* experiments, the equal variance could not be assumed and a non-parametric Mann-Whitney test was used. The confidence level used for all the statistical analyses was of 0.95 (alpha value = 0.05). Two-tail statistical analysis was applied for experimental design without predicted result, and one-tail for validation experiments (*$P < 0.05$; **$P < 0.01$; ***$P < 0.001$).

Data availability

The mouse gene expression datasets are available at https://www.ncbi.nlm.nih.gov/geo/query/acc.cgi?acc=GSE74245

For cellular, molecular and metabolic assays, the lipidomics analysis on prostate cancer cell line, fatty acid rescue assay and computer simulations of 3-FP and PDC docking, the methods are available in Supplementary Note.

URLs

Gene Expression Omnibus, https://www.ncbi.nlm.nih.gov/geo/; MetaboAnalyst, http://www.metaboanalyst.ca/; UCSC Genome Browser on Human, https://genome.ucsc.edu/cgi-bin/hgTracks?db=hg38&lastVirtModeType=default&lastVirtModeExtraState=&virtModeType=default&virtMode=0&nonVirtPosition=&position=chr8%3A124998506-125022283&hgsid=641911343_mdAzqHRm9nypyskAklqb2aiYGn1X

Supplementary Methods

Cellular, molecular and metabolic assays

Lactate production was performed according to technical specifications using Lactate colorimetric/ Fluorometric assay kit (Catalog# K607-100, Biovision Incorporated). Acetyl-CoA production was measured using PicoProbe™ Acetyl-CoA Fluorometric Assay Kit (Catalog# K317-100, Biovision Incorporated). NADH/NAD$^+$ ratio measurement was performed using NAD/NADH Quantitation Colorimetric Kit (Catalog# K337-100, Biovision Incorporated). ATP/ADP ratio measurement was performed using ADP/ATP Ratio Bioluminescence Assay Kit (Catalog# K255-200, Biovision Incorporated). PDH activity in cell or tumour lysates were measured using the DipStick assay kit[19,23,48] (Catalog# MSP90, MitoSciences). Cells were lysed in the sample buffer provided by the manufacturer, followed by centrifugation and measurement of the protein concentration with the BioRad Protein Assay. Eighty micrograms of lysates from the whole cell or nuclear fractionation were loaded and PDH activity was measured according to the manufacturer's protocol. Oxygen consumption rate (OCR) was measured with a XFp extracellular flux analyzer (Seahorse Bioscience). Briefly, 45,000 cells per well were seeded in a XFp plate, and OCR measurements were normalized to protein amount analyzed by Pierce BCA Protein Assay Kit (Catalog# 23225). Cells were initially plated in 10% FBS DMEM media for 24 h, and 1h before measurements, media was changed to DMEM serum and bicarbonate free, with glutamine and glucose (10 mM). The mitochondrial stress test was carried out using the following concentrations of the injected compound: Oligomycin (1 μM). LipidTox (Catalog# H34477, Molecular Probes) and DAPI (Catalog# H-1200, Vector Laboratories) were used on prostate cryostat section slide at the concentrations suggested by manufacturer's protocols and images were acquired with a TCS SP5 confocal microscope (Leica). Images of prostate glands tissue sections stained with DAPI and LipiTox were acquired with a Leica TCS SP5 confocal microscope, using a 63X/1.4 N.A. objective (Leica HCX PL APO lambda blue 63.0×1.40 OIL UV); 5 different fields of view of 100 μm × 100 μm were acquired for each genotype. Lipid droplets segmentation and fluorescence analysis were performed using a custom-developed pipeline in CellProfiler (Broad Institute) open-source software[62].

Lipidomics analysis on prostate cancer cell line

~ 4 million adherent cells were harvested and suspended in 450 μL PBS. The cells were pottered for 20 sec, snap frozen in liquid nitrogen and defrozen with 37 °C water. The cell lysate was centrifuged for 15 min at 14000 rpm. 420 μL supernatant of cell lysate was collected and each pellet was suspended in 420 μL PBS. Gas chromatographic runs were performed with helium as carrier gas at 0.6 mL/min. The split inlet temperature was set to 250 °C and the injection volume of 1 μL. A split ratio of 1:50 was used. The GC oven temperature ramp was from 50 °C to 300 °C at 5 °C/min for the longer column and from 35 °C to 300 °C at 25 °C/min for the shorter column.

The data acquisition rate was 10 Hz in both cases. For the TOF-MS, an EI source (70 eV) was used, and full-scan spectra (mass range from 50 to 550 amu) were recorded in the positive ion mode. The ion source and transfer line temperatures were set, respectively, to 200 °C and 250 °C. The web-based metabolomic data processing tool *MetaboAnalyst 3.0* [63]was used to obtain a global metabolic profiling of cholesterol and its esterified derivatives among prostate cancer cells infected with two sh*PDHA1* and a scramble control on mass spectra data. The Partial Least Squares-Discriminant Analysis (PLS-DA), a supervised multivariate statistical analysis method, was used. Variable Importance in Projection (VIP), which is a weighted sum of squares of the PLS loadings, was thereafter calculated and utilized to discriminate among groups.

Radiolabelled Glucose and Glutamine Uptake, Fatty Acid and Cholesterol synthesis

Cells were doxycycline treated for 5 days and then seeded in triplicate 24 hrs prior to the experiment in complete media. For uptake assay, the radioactive substrates were added to the cells in a buffered solution (140 mM NaCl, 20 mM Hepes/Na, 2.5 mM $MgSO_4$, 1 $mMCaCl_2$, and 5 mM KCl, pH 7.4) and incubate for 15 minutes at 37°C. Cells were subsequently washed with cold PBS and lysed with 0.1 M NaOH. The lysates were resuspended and transferred to scintillation vials for counting. For fatty acid synthesis analysis, media were changed to RPMI + 10% or 1% serum supplemented with 2 μCi ^{14}C-glucose or ^{14}C-glutamine at 16 h prior to the end of the experiment. The cells were washed three times in ice cold PBS and then lysed in radioimmunoprecipitation assay (RIPA) buffer. Samples were first resuspended in 4 volumes of a $CHCl_3$: MeOH (1:1) solution and then an additional volume of dH_2O was added. The solution was then centrifuged at 1000 rpm for 5 minutes at room temperature. The lower phase was collected and an equivalent volume of each sample was dried under a nitrogen stream before resuspension in ethanol, transfer to a scintillation vial and counted on the scintillation counter. Data were normalized to protein levels. For cholesterol synthesis analysis, media were changed to RPMI + 10% or 1% serum supplemented with 2 μCi ^{14}C-glucose or ^{14}C-glutamine at 16 h prior to the end of the experiment. Cells were lysed directly in methanol and subject to lipids separation as described above. The lower phase was evaporated and then dissolved in $CHCl_3$:CH_3OH (2:1, vol:vol). Lipids were separated by thin layer chromatography on Aluminum TLC Silica plate (Merck, Germany). Plates were developed sequentially with solvent A (toluene:diethyl ether:ethyl acetate:acetic acid,75:10:13:1.2, by vol) to 8 cm above the level of application and dried under nitrogen. The TLC plates were then developed with solvent B (hexane:diethyl ether:formic acid, 80:20:2, v/v/v) to 14 cm above the level of application[64]. After air-drying of the plates, the samples were made visible by iodine vapor staining. Cholesterol (Sigma) was dissolved in $CHCl_3$:CH_3OH (2:1, vol:vol) and 20 μg were developed in parallel to the samples to determine the exact migration front and the bands to cut for the quantification. The aluminum plates were cut in correspondence to the cholesterol band and the radioactivity was counted using a Beckman LS1000 β-Counter.

Fatty acid rescue assay

For fatty-acid rescue, palmitate and oleate were dissolved in ethanol and complexed to 5% (w/v) fatty acid-free bovine serum albumin (Catalog# A8806-1G, Sigma) in PBS. The fatty acid mixture was directly added to RPMI media (Catalog# 21875034, Thermo Fisher Scientific) containing delipidated serum (Catalog# 12676011, Thermo scientific) to make the fatty-acid free medium. Cells were supplemented with either fatty acids conjugated to BSA or BSA alone for 6 days[30].

Computer simulations

The X-ray structure of human PDHA1 (PDB code 1NI4 [65]) was used as starting model for molecular dynamics (MD) simulations. The exact positions of the pyruvate and of the catalytically relevant waters, not present in the 1NI4 crystal structure, were obtained by structural superposition with the PDH structure from Geobacillus stearothermophilus (pdb code 3DV0 [66]). Furthermore, the structure of the 3-FP/PDHA1 complex was obtained by replacing a hydrogen in the pyruvate methyl group with a fluorine atom. The two molecular complexes were fully solvated in a TIP3P water box[67] with a minimum distance of 10 Å from the protein surface and the charge neutrality of the systems was restored by adding a proper number of counter-ions. The protein and the water molecules were parameterized using the ff14SB force field[68], while pyruvate, 3-FP, and Thiamine pyrophosphate (TPP) using the general amber force field (GAFF) parameters and atomic charges computed with the Am1-bcc scheme implemented in the AMBERTOOLS15[69]. Finally, monovalent ions were modeled with parameters proposed by Cheatham and coworkers[70] and Mg^{2+} with the parameterization of Li et al[71]. Energy minimizations and MD simulations were carried out with a van der Waals and short-range electrostatic cut-off of 8 Å, whereas the long-range electrostatic forces were taken into account with the Particle Mesh Ewald method[72].

The initial structures of the two complexes were energy minimized for 1000 steps to remove possible steric clashes. Then, the temperature was slowly increased to 300K in 30 ps. Subsequently, an MD simulation of 20 ns in the NPT ensemble (1atm, 300 K) was carried out with the pmemd.cuda code available in AMBER14[73], to sample structures for the calculation of the binding free energy. 125 snapshots were extracted from the last 10ns of the MD simulations and the binding free energy for both pyruvate and 3-FP was estimated with the MM-GBSA method[74]. In particular, GB calculations were performed using the Hawkins, Cramer, Truhlar model[75] and the Surface area (SA) was computed by the Connolly algorithm as implemented in MOLSURF[76].

Supplementary Table 1 Primers for mouse or mouse prostate genotyping

Genomic mutation	Forward primer sequence	Reverse primer sequence	Product length (bp)
Pten$^{\text{loxP/loxP}}$	5′-AAAGTTCCCCTGCTGATGATTTGT-3′	5′-TGTTTTTGACCAATTAAAGTAGGCTGTG-3′	loxP allele=480, Wild type allele=350
Pten$^{\text{pc-/-}}$	5′-AAAGTTCCCCTGCTGATGATTTGT-3′	5′-TTCTCTTGAGCACTGTTTCACAGGC-3′	Mutant allele=~1000, Wild type allele=N/A
Pdha1$^{\text{loxP/loxP}}$	5′-CGTTGTTGAGAGAGCAGCA-3′	5′-CGCACAAGATATCCATTCCA-3′	loxP allele=380, Wild type allele=303
Pdha1$^{\text{pc-/Y}}$	5′-CGTTGTTGAGAGAGCAGCA-3′	5′-CGCACAAGATATCCATTCCA-3′	Mutant allele=~300, Wild type allele =~800
Probasin-Cre4	5′-CTTCTGTGGTGTGACATAATTGG-3′	5′-GATGAGTTTGGACAAACCACAAC-3′	Tg(Pbsn-cre)4Prb=393

Supplementary Table 2 Primers for real-time PCR

Gene (accession number)	Forward primer sequence	Reverse primer sequence	Product length (bp)
Pdha1 (NM_008810)	5′-GAAATGTGACCTTCATCGGCT-3′	5′-TGATCCGCCTTTAGCTCCATC-3′	123
Dlat (NM_145614)	5′-CTTTAGCCTCCAAAGCGAGAG-3′	5′-AGATTGTAAATGTTCCACCCTGG-3′	69
Dld (NM_007861)	5′-GAGCTGGAGTCGTGTGTACC-3′	5′-CCTATCACTGTCACGTCAGCC-3′	138
Pdp1 (NM_001098231)	5′-GCACCCATAGAGGACCGGA-3′	5′-CCTGCATGACCATCAAAAACCC-3′	83
Pdp2 (NM_001024606)	5′-CTGTGTCCTACTGGATCTTCAA-3′	5′-CAGGTTCCTACTCGTGGCA-3′	99
Pdk1 (NM_172665)	5′-GGACTTCGGGTCAGTGAATGC-3′	5′-TCCTGAGAAGATTGTCGGGGA-3′	122
Pdk2 (NM_133667)	5′-AGGGGCACCCAAGTACATC-3′	5′-TGCCGGAGGAAAGTGAATGAC-3′	123
Pdk3 (NM_145630)	5′-TCCTGGACTTCGGAAGGGATA-3′	5′-GAAGGGCGGTTCAACAAGTTA-3′	133
PDK4 (NM_013743)	5′-AGGGAGGTCGAGCTGTTCTC-3′	5′-GGAGTGTTCACTAAGCGGTCA-3′	185
Srebf1 (NM_011480)	5′- TGACCCGGCTATTCCGTGA -3′	5′-CTGGGCTGAGCAATACAGTTC-3′	61
Srebf2 (NM_033218)	5′-GCAGCAACGGGACCATTCT-3′	5′-CCCCATGACTAAGTCCTTCAACT-3′	200
Sqle (NM_009270)	5′-ATAAGAAATGCGGGGATGTCAC-3′	5′- ATATCCGAGAAGGCAGCGAAC -3′	163
Acly (NM_134037)	5′-ACCCTTTCACTGGGGATCACA-3′	5′-GACAGGGATCAGGATTTCCTTG-3′	65
Acaca (NM_133360)	5′-GATGAACCATCTCCGTTGGC-3′	5′-GACCCAATTATGAATCGGGAGTG-3′	65
Acacb (NM_133904)	5′-CCTTTGGCAACAAGCAAGGTA-3′	5′-AGTCGTACACATAGGTGGTCC-3′	123
Fasn (NM_007988)	5′-GGAGGTGGTGATAGCCGGTAT-3′	5′-TGGGTAATCCATAGAGCCCAG-3′	140
Scd1 (NM_009127.4)	5′-TTCTTGCGATACACTCTGGTGC-3′	5′-CGGGATTGAATGTTCTTGTCGT-3′	98
Acss1 (NM_080575)	5′-GTTTGGGACACTCCTTACCATAC-3′	5′-AGGCAGTTGACAGACACATTC-3′	101
Acss2 (NM_019811)	5′-AAACACGCTCAGTAGCACCAC-3′	5′-AGCCAAGTAGGAAGCTCTCTC-3′	109
Cpt1a (NM_013495)	5′-CTCCGCCTGAGCCATGAAG-3′	5′-CACCAGTGATGATGCCATTCT-3′	100
Cpt2 (NM_009949)	5′-CAGCACAGCATCGTACCCA-3′	5′-TCCCAATGCCGTTCTCAAAAT-3′	172
Cd36 (NM_001159556)	5′-ATGGGCTGTGATCGGAACTG-3′	5′-GTCTTCCCAATAAGCATGTCTCC-3′	110
Idh1 (NM_010497)	5′-ATGCAAGGAGATGAAATGACACG-3′	5′-GCATCACGATTCTCTATGCCTAA-3′	116
Idh2 (NM_173011)	5′-GGAGAAGCCGGTAGTGGAGAT-3′	5′-GGTCTGGTCACGGTTTGGAA-3′	139
Idh3a (NM_029573)	5′-TGGGTGTCCAAGGTCTCTC-3′	5′-CTCCCACTGAATAGGTGCTTTG-3′	177
Idh3b (NM_130884)	5′-TGGAGAGGTCTCGGAACATCT-3′	5′-AGCCTTGAACACTTCCTTGAC-3′	150

Idh3g (NM_008323)	5′-GGTGCTGCAAAGGCAATGC-3′	5′-TATGCCGCCCACCATACTTAG-3′	136
Actb (NM_007393)	5′-GGCTGTATTCCCCTCCATCG-3′	5′-CCAGTTGGTAACAATGCCATGT-3′	154
SREBF1 (NM_001005291)	5′-CGGAACCATCTTGGCAACAGT-3′	5′-CGCTTCTCAATGGCGTTGT-3′	141
SREBF2 (NM_004599)	5′-AACGGTCATTCACCCAGGTC-3′	5′-GGCTGAAGAATAGGAGTTGCC-3′	133
SQLE (NM_003129)	5′-GATGATGCAGCTATTTTCGAGGC-3′	5′-CCTGAGCAAGGATATTCACGACA-3′	88
ACLY (NM_198830)	5′-TCGGCCAAGGCAATTTCAGAG-3′	5′-CGAGCATACTTGAACCGATTCT-3′	95
ACACA (NM_198838)	5′-ATGTCTGGCTTGCACCTAGTA-3′	5′-CCCCAAAGCGAGTAACAAATTCT-3′	106
ACACB (NM_001093)	5′-AGAAGACAAGAAGCAGGCAAAC-3′	5′-GTAGACTCACGAGATGAGCCA-3′	117
FASN (NM_004104)	5′-AAGGACCTGTCTAGGTTTGATGC-3′	5′-TGGCTTCATAGGTGACTTCCA-3′	106
SCD (NM_005063)	5′-TTCCTACCTGCAAGTTCTACACC-3′	5′-CCGAGCTTTGTAAGAGCGGT-3′	116
ACSS1 (NM_001252676)	5′-CGTCCTTTTTGAGAGCACCC-3′	5′-GCATCACCGTATTTCAGCAACA-3′	129
ACSS2 (NM_001242393)	5′-TTGGGGCTTTGCACTCCATT-3′	5′-AGGCATCTGTAGTGATGAGAAGA-3′	102
CPT1A (NM_001876)	5′-ATCAATCGGACTCTGGAAACGG-3′	5′-TCAGGGAGTAGCGCATGGT-3′	121
CPT2 (NM_000098)	5′-CTGGAGCCAGAAGTGTTCCAC-3′	5′-AGGCACAAAGCGTATGAGTCT-3′	78
CD36 (NM_000072)	5′-CTTTGGCTTAATGAGACTGGGAC-3′	5′-GCAACAAACATCACCACACCA-3′	134
IDH1 (NM_005896)	5′-CACCAAATGGCACCATACGAA-3′	5′-CCCCATAAGCATGACGACCTAT-3′	129
IDH2 (NM_002168)	5′-CCCGTATTATCTGGCAGTTCATC-3′	5′-ATCAGTCTGGTCACGGTTTGG-3′	104
IDH3A (NM_005530)	5′-CCCGCGTGGATCTCTAAGG-3′	5′-AATTTCTGGGCCAATACCATCTC-3′	129
IDH3B (NM_006899)	5′-TAGTGCAGAATACGCAGTCTTTG-3′	5′-CAGCATGTTGGAAGCCGAC-3′	112
IDH3G (NM_174869)	5′-GACCCGGCACAAGGACATAG-3′	5′-GCTTGAAGGCATACTCGGCAA-3′	155
ACTB (NM_001101)	5′-CATGTACGTTGCTATCCAGGC-3′	5′-CTCCTTAATGTCACGCACGAT-3′	250

Supplementary Table 3 Primers for Chromatin immunoprecipitation analysis

Gene (Gene ID)	Forward primer sequence	Reverse primer sequence
SQLE (6713)	5′-CTGATTCCTCTTTCGGACTCCC-3′	5′-ACCGCAGCAGCCCCAGCTCCTG-3′
ACLY (47)	5′-TTTCAAGGCTTATCCCTACTCC-3′	5′-TGCGTCAATCCTTCACTGTCCT-3′
E2F1 (1869)	5′-GTGTGGCGAAGAGCAGCAGGTC-3′	5′-CCGTGAGCGTCATGGCCTTGGC-3′
CCND1 (595)	5′-TGGCGTTCTTGGAAATGCGCCC-3′	5′-GTGGAGGTGGCTCTGCAGTAGG-3′

7. Reference

Reference for introduction

1. Koppenol, W. H.; Bounds, P. L.; Dang, C. V., Otto Warburg's contributions to current concepts of cancer metabolism. Nat Rev Cancer 2011, 11 (5), 325-37.

2. Martin, G. S., The hunting of the Src. Nat Rev Mol Cell Biol 2001, 2 (6), 467-75.

3. Martincorena, I.; Campbell, P. J., Somatic mutation in cancer and normal cells. Science 2015, 349 (6255), 1483-9.

4. Pavlova, N. N.; Thompson, C. B., The Emerging Hallmarks of Cancer Metabolism. Cell Metab 2016, 23 (1), 27-47.

5. Chen, M.; Zhang, J.; Sampieri, K.; Clohessy, J. G.; Mendez, L.; Gonzalez-Billalabeitia, E.; Liu, X. S.; Lee, Y. R.; Fung, J.; Katon, J. M.; Menon, A. V.; Webster, K. A.; Ng, C.; Palumbieri, M. D.; Diolombi, M. S.; Breitkopf, S. B.; Teruya-Feldstein, J.; Signoretti, S.; Bronson, R. T.; Asara, J. M.; Castillo-Martin, M.; Cordon-Cardo, C.; Pandolfi, P. P., An aberrant SREBP-dependent lipogenic program promotes metastatic prostate cancer. Nat Genet 2018, 50 (2), 206-218.

6. Chen, J.; Guccini, I.; Mitri, D. D.; Brina, D.; Revandkar, A.; Sarti, M.; Pasquini, E.; Alajati, A.; Pinton, S.; Losa, M.; Civenni, G.; Catapano, C. V.; Sgrignani, J.; Cavalli, A.; D'Antuono, R.; Asara, J. M.; Morandi, A.; Chiarugi, P.; Crotti, S.; Agostini, M.; Montopoli, M.; Masgras, I.; Rasola, A.; Garcia-Escudero, R.; Delaleu, N.; Rinaldi, A.; Bertoni, F.; Bono, J.; Carracedo, A.; Alimonti, A., Compartmentalized activities of the pyruvate dehydrogenase complex sustain lipogenesis in prostate cancer. Nat Genet 2018, 50 (2), 219-228.

7. Poulose, N.; Amoroso, F.; Steele, R. E.; Singh, R.; Ong, C. W.; Mills, I. G., Genetics of lipid metabolism in prostate cancer. Nat Genet 2018, 50 (2), 169-171.

8. Knott, S. R. V.; Wagenblast, E.; Khan, S.; Kim, S. Y.; Soto, M.; Wagner, M.; Turgeon, M. O.; Fish, L.; Erard, N.; Gable, A. L.; Maceli, A. R.; Dickopf, S.; Papachristou, E. K.; D'Santos, C. S.; Carey, L. A.; Wilkinson, J. E.; Harrell, J. C.; Perou, C. M.; Goodarzi, H.; Poulogiannis, G.; Hannon, G. J., Asparagine bioavailability governs metastasis in a model of breast cancer. Nature 2018.

9. Cairns, R. A.; Harris, I. S.; Mak, T. W., Regulation of cancer cell metabolism. Nat Rev Cancer 2011, 11 (2), 85-95.

10. Hanahan, D.; Weinberg, R. A., Hallmarks of cancer: the next generation. Cell 2011, 144 (5), 646-74.

11. Curi, R.; Newsholme, P.; Newsholme, E. A., Metabolism of Pyruvate by Isolated Rat Mesenteric Lymphocytes, Lymphocyte Mitochondria and Isolated Mouse Macrophages. Biochemical Journal 1988, 250 (2), 383-388.

12. DeBerardinis, R. J.; Mancuso, A.; Daikhin, E.; Nissim, I.; Yudkoff, M.; Wehrli, S.; Thompson, C. B., Beyond aerobic glycolysis: Transformed cells can engage in glutamine metabolism that exceeds the requirement for protein and nucleotide synthesis. P Natl Acad Sci USA 2007, 104 (49), 19345-19350.

13. Altman, B. J.; Stine, Z. E.; Dang, C. V., From Krebs to clinic: glutamine metabolism to cancer therapy. Nature Reviews Cancer 2016, 16 (10), 619-634.

14. DeBerardinis, R. J.; Chandel, N. S., Fundamentals of cancer metabolism. Sci Adv 2016, 2 (5).

15. White, E., Exploiting the bad eating habits of Ras-driven cancers. Gene Dev 2013, 27 (19), 2065-2071.

16. Li, B.; Qiu, B.; Lee, D. S. M.; Walton, Z. E.; Ochocki, J. D.; Mathew, L. K.; Mancuso, A.; Gade, T. P. F.; Keith, B.; Nissim, I.; Simon, M. C., Fructose-1,6-bisphosphatase opposes renal carcinoma progression. Nature 2014, 513 (7517), 251-+.

17. Locasale, J. W.; Grassian, A. R.; Melman, T.; Lyssiotis, C. A.; Mattaini, K. R.; Bass, A. J.; Heffron, G.; Metallo, C. M.; Muranen, T.; Sharfi, H.; Sasaki, A. T.; Anastasiou, D.; Mullarky, E.; Vokes, N. I.; Sasaki, M.; Beroukhim, R.; Stephanopoulos, G.; Ligon, A. H.; Meyerson, M.; Richardson, A. L.; Chin, L.; Wagner, G.; Asara, J. M.; Brugge, J. S.; Cantley, L. C.; Vander Heiden, M. G., Phosphoglycerate dehydrogenase diverts glycolytic flux and contributes to oncogenesis. Nature Genetics 2011, 43 (9), 869-U79.

18. Possemato, R.; Marks, K. M.; Shaul, Y. D.; Pacold, M. E.; Kim, D.; Birsoy, K.; Sethumadhavan, S.; Woo, H. K.; Jang, H. G.; Jha, A. K.; Chen, W. W.; Barrett, F. G.; Stransky, N.; Tsun, Z. Y.; Cowley, G. S.; Barretina, J.; Kalaany, N. Y.; Hsu, P. P.; Ottina, K.; Chan, A. M.; Yuan, B.; Garraway, L. A.; Root, D. E.; Mino-Kenudson, M.; Brachtel, E. F.; Driggers, E. M.; Sabatini, D. M., Functional genomics reveal that the serine synthesis pathway is essential in breast cancer. Nature 2011, 476 (7360), 346-U119.

19. Marin-Valencia, I.; Yang, C.; Mashimo, T.; Cho, S.; Baek, H.; Yang, X. L.; Rajagopalan, K. N.; Maddie, M.; Vemireddy, V.; Zhao, Z.; Cai, L.; Good, L.; Tu, B. P.; Hatanpaa, K. J.; Mickey, B. E.; Mates, J. M.; Pascual, J. M.; Maher, E. A.; Malloy, C. R.; Deberardinis, R. J.; Bachoo, R. M., Analysis of tumor metabolism reveals mitochondrial glucose oxidation in genetically diverse human glioblastomas in the mouse brain in vivo. Cell Metab 2012, 15 (6), 827-37.

20. Viale, A.; Pettazzoni, P.; Lyssiotis, C. A.; Ying, H.; Sanchez, N.; Marchesini, M.; Carugo, A.; Green, T.; Seth, S.; Giuliani, V.; Kost-Alimova, M.; Muller, F.; Colla, S.; Nezi, L.;

Genovese, G.; Deem, A. K.; Kapoor, A.; Yao, W.; Brunetto, E.; Kang, Y.; Yuan, M.; Asara, J. M.; Wang, Y. A.; Heffernan, T. P.; Kimmelman, A. C.; Wang, H.; Fleming, J. B.; Cantley, L. C.; DePinho, R. A.; Draetta, G. F., Oncogene ablation-resistant pancreatic cancer cells depend on mitochondrial function. Nature 2014, 514 (7524), 628-32.

21. LeBleu, V. S.; O'Connell, J. T.; Gonzalez Herrera, K. N.; Wikman, H.; Pantel, K.; Haigis, M. C.; de Carvalho, F. M.; Damascena, A.; Domingos Chinen, L. T.; Rocha, R. M.; Asara, J. M.; Kalluri, R., PGC-1alpha mediates mitochondrial biogenesis and oxidative phosphorylation in cancer cells to promote metastasis. Nat Cell Biol 2014, 16 (10), 992-1003, 1-15.

22. Davidson, S. M.; Papagiannakopoulos, T.; Olenchock, B. A.; Heyman, J. E.; Keibler, M. A.; Luengo, A.; Bauer, M. R.; Jha, A. K.; O'Brien, J. P.; Pierce, K. A.; Gui, D. Y.; Sullivan, L. B.; Wasylenko, T. M.; Subbaraj, L.; Chin, C. R.; Stephanopolous, G.; Mott, B. T.; Jacks, T.; Clish, C. B.; Vander Heiden, M. G., Environment Impacts the Metabolic Dependencies of Ras-Driven Non-Small Cell Lung Cancer. Cell Metab 2016, 23 (3), 517-28.

23. Hensley, C. T.; Faubert, B.; Yuan, Q.; Lev-Cohain, N.; Jin, E.; Kim, J.; Jiang, L.; Ko, B.; Skelton, R.; Loudat, L.; Wodzak, M.; Klimko, C.; McMillan, E.; Butt, Y.; Ni, M.; Oliver, D.; Torrealba, J.; Malloy, C. R.; Kernstine, K.; Lenkinski, R. E.; DeBerardinis, R. J., Metabolic Heterogeneity in Human Lung Tumors. Cell 2016, 164 (4), 681-94.

24. Maher, E. A.; Marin-Valencia, I.; Bachoo, R. M.; Mashimo, T.; Raisanen, J.; Hatanpaa, K. J.; Jindal, A.; Jeffrey, F. M.; Choi, C.; Madden, C.; Mathews, D.; Pascual, J. M.; Mickey, B. E.; Malloy, C. R.; DeBerardinis, R. J., Metabolism of [U-13 C]glucose in human brain tumors in vivo. NMR Biomed 2012, 25 (11), 1234-44.

25. Sellers, K.; Fox, M. P.; Bousamra, M.; Slone, S. P.; Higashi, R. M.; Miller, D. M.; Wang, Y. L.; Yan, J.; Yuneva, M. O.; Deshpande, R.; Lane, A. N.; Fan, T. W. M., Pyruvate carboxylase is critical for non-small-cell lung cancer proliferation. J Clin Invest 2015, 125 (2), 687-698.

26. Wheaton, W. W.; Weinberg, S. E.; Hamanaka, R. B.; Soberanes, S.; Sullivan, L. B.; Anso, E.; Glasauer, A.; Dufour, E.; Mutlu, G. M.; Budigner, G. R. S.; Chandel, N. S., Metformin inhibits mitochondrial complex I of cancer cells to reduce tumorigenesis. Elife 2014, 3.

27. Gui, D. Y.; Sullivan, L. B.; Luengo, A.; Hosios, A. M.; Bush, L. N.; Gitego, N.; Davidson, S. M.; Freinkman, E.; Thomas, C. J.; Vander Heiden, M. G., Environment Dictates Dependence on Mitochondrial Complex I for NAD plus and Aspartate Production and Determines Cancer Cell Sensitivity to Metformin. Cell Metabolism 2016, 24 (5), 716-727.

28. Svensson, R. U.; Parker, S. J.; Eichner, L. J.; Kolar, M. J.; Wallace, M.; Brun, S. N.; Lombardo, P. S.; Van Nostrand, J. L.; Hutchins, A.; Vera, L.; Gerken, L.; Greenwood, J.; Bhat, S.; Harriman, G.; Westlin, W. F.; Harwood, H. J.; Saghatelian, A.; Kapeller, R.; Metallo, C. M.; Shaw, R. J., Inhibition of acetyl-CoA carboxylase suppresses fatty acid synthesis and tumor growth of non-small-cell lung cancer in preclinical models. Nat Med 2016, 22 (10), 1108-1119.

29. Coloff, J. L.; Murphy, J. P.; Braun, C. R.; Harris, I. S.; Shelton, L. M.; Kami, K.; Gygi, S. P.; Selfors, L. M.; Brugge, J. S., Differential Glutamate Metabolism in Proliferating and Quiescent Mammary Epithelial Cells. Cell Metabolism 2016, 23 (5), 867-880.

30. Vazquez, F.; Lim, J. H.; Chim, H.; Bhalla, K.; Girnun, G.; Pierce, K.; Clish, C. B.; Granter, S. R.; Widlund, H. R.; Spiegelman, B. M.; Puigserver, P., PGC1alpha expression defines a subset of human melanoma tumors with increased mitochondrial capacity and resistance to oxidative stress. Cancer Cell 2013, 23 (3), 287-301.

31. Ahn, C. S.; Metallo, C. M., Mitochondria as biosynthetic factories for cancer proliferation. Cancer Metab 2015, 3 (1), 1.

32. Weinberg, S. E.; Chandel, N. S., Targeting mitochondria metabolism for cancer therapy. Nat Chem Biol 2015, 11 (1), 9-15.

33. Vyas, S.; Zaganjor, E.; Haigis, M. C., Mitochondria and Cancer. Cell 2016, 166 (3), 555-66.

34. Sullivan, L. B.; Gui, D. Y.; Heiden, M. G. V., Altered metabolite levels in cancer: implications for tumour biology and cancer therapy. Nat Rev Cancer 2016, 16 (11), 680-693.

35. Mullen, A. R.; Hu, Z.; Shi, X.; Jiang, L.; Boroughs, L. K.; Kovacs, Z.; Boriack, R.; Rakheja, D.; Sullivan, L. B.; Linehan, W. M.; Chandel, N. S.; DeBerardinis, R. J., Oxidation of Alpha-Ketoglutarate Is Required for Reductive Carboxylation in Cancer Cells with Mitochondrial Defects. Cell Reports 2014, 7 (5), 1679-1690.

36. Mullen, A. R.; Wheaton, W. W.; Jin, E. S.; Chen, P. H.; Sullivan, L. B.; Cheng, T.; Yang, Y.; Linehan, W. M.; Chandel, N. S.; DeBerardinis, R. J., Reductive carboxylation supports growth in tumour cells with defective mitochondria. Nature 2011, 481 (7381), 385-8.

37. Costello, L. C.; Franklin, R. B., Aconitase activity, citrate oxidation, and zinc inhibition in rat ventral prostate. Enzyme 1981, 26 (6), 281-7.

38. Costello, L. C.; Liu, Y.; Franklin, R. B.; Kennedy, M. C., Zinc inhibition of mitochondrial aconitase and its importance in citrate metabolism of prostate epithelial cells. J Biol Chem 1997, 272 (46), 28875-81.

39. Costello, L. C.; Liu, Y.; Zou, J.; Franklin, R. B., The pyruvate dehydrogenase E1 alpha gene is testosterone and prolactin regulated in prostate epithelial cells. Endocr Res 2000, 26 (1), 23-39.

40. Sutendra, G.; Kinnaird, A.; Dromparis, P.; Paulin, R.; Stenson, T. H.; Haromy, A.; Hashimoto, K.; Zhang, N.; Flaim, E.; Michelakis, E. D., A nuclear pyruvate dehydrogenase complex is important for the generation of acetyl-CoA and histone acetylation. Cell 2014, 158 (1), 84-97.

41. Chueh, F. Y.; Leong, K. F.; Cronk, R. J.; Venkitachalam, S.; Pabich, S.; Yu, C. L., Nuclear localization of pyruvate dehydrogenase complex-E2 (PDC-E2), a mitochondrial enzyme, and its role in signal transducer and activator of transcription 5 (STAT5)-dependent gene transcription. Cell Signal 2011, 23 (7), 1170-8.

42. Patel, M. S.; Nemeria, N. S.; Furey, W.; Jordan, F., The pyruvate dehydrogenase complexes: structure-based function and regulation. J Biol Chem 2014, 289 (24), 16615-23.

43. Kinnaird, A.; Zhao, S.; Wellen, K. E.; Michelakis, E. D., Metabolic control of epigenetics in cancer. Nat Rev Cancer 2016, 16 (11), 694-707.

44. Yang, W.; Xia, Y.; Ji, H.; Zheng, Y.; Liang, J.; Huang, W.; Gao, X.; Aldape, K.; Lu, Z., Nuclear PKM2 regulates beta-catenin transactivation upon EGFR activation. Nature 2011, 480 (7375), 118-22.

45. Nagaraj, R.; Sharpley, M. S.; Chi, F.; Braas, D.; Zhou, Y.; Kim, R.; Clark, A. T.; Banerjee, U., Nuclear Localization of Mitochondrial TCA Cycle Enzymes as a Critical Step in Mammalian Zygotic Genome Activation. Cell 2017, 168 (1-2), 210-223 e11.

46. Papandreou, I.; Cairns, R. A.; Fontana, L.; Lim, A. L.; Denko, N. C., HIF-1 mediates adaptation to hypoxia by actively downregulating mitochondrial oxygen consumption. Cell Metab 2006, 3 (3), 187-97.

47. Kim, J. W.; Tchernyshyov, I.; Semenza, G. L.; Dang, C. V., HIF-1-mediated expression of pyruvate dehydrogenase kinase: a metabolic switch required for cellular adaptation to hypoxia. Cell Metab 2006, 3 (3), 177-85.

References of results

1 Zong, W. X., Rabinowitz, J. D. & White, E. Mitochondria and Cancer. *Mol Cell* **61**, 667-676, doi:10.1016/j.molcel.2016.02.011 (2016).

2 LeBleu, V. S. *et al.* PGC-1alpha mediates mitochondrial biogenesis and oxidative phosphorylation in cancer cells to promote metastasis. *Nat Cell Biol* **16**, 992-1003, 1001-1015, doi:10.1038/ncb3039 (2014).

3 Marin-Valencia, I. *et al.* Analysis of tumor metabolism reveals mitochondrial glucose oxidation in genetically diverse human glioblastomas in the mouse brain in vivo. *Cell Metab* **15**, 827-837, doi:10.1016/j.cmet.2012.05.001 (2012).

4 Vazquez, F. *et al.* PGC1alpha expression defines a subset of human melanoma tumors with increased mitochondrial capacity and resistance to oxidative stress. *Cancer Cell* **23**, 287-301, doi:10.1016/j.ccr.2012.11.020 (2013).

5 Viale, A. *et al.* Oncogene ablation-resistant pancreatic cancer cells depend on mitochondrial function. *Nature* **514**, 628-632, doi:10.1038/nature13611 (2014).

6 Ahn, C. S. & Metallo, C. M. Mitochondria as biosynthetic factories for cancer proliferation. *Cancer Metab* **3**, 1, doi:10.1186/s40170-015-0128-2 (2015).

7 Weinberg, S. E. & Chandel, N. S. Targeting mitochondria metabolism for cancer therapy. *Nat Chem Biol* **11**, 9-15, doi:10.1038/nchembio.1712 (2015).

8 Vyas, S., Zaganjor, E. & Haigis, M. C. Mitochondria and Cancer. *Cell* **166**, 555-566, doi:10.1016/j.cell.2016.07.002 (2016).

9 Hensley, C. T. *et al.* Metabolic Heterogeneity in Human Lung Tumors. *Cell* **164**, 681-694, doi:10.1016/j.cell.2015.12.034 (2016).

10 Davidson, S. M. *et al.* Environment Impacts the Metabolic Dependencies of Ras-Driven Non-Small Cell Lung Cancer. *Cell Metab* **23**, 517-528, doi:10.1016/j.cmet.2016.01.007 (2016).

11 Wieland, O. H. The mammalian pyruvate dehydrogenase complex: structure and regulation. *Rev Physiol Biochem Pharmacol* **96**, 123-170 (1983).

12 Kolobova, E., Tuganova, A., Boulatnikov, I. & Popov, K. M. Regulation of pyruvate dehydrogenase activity through phosphorylation at multiple sites. *Biochem J* **358**, 69-77 (2001).

13 Roche, T. E. *et al.* Distinct regulatory properties of pyruvate dehydrogenase kinase and phosphatase isoforms. *Prog Nucleic Acid Res Mol Biol* **70**, 33-75 (2001).

14 Trotman, L. C. *et al.* Pten dose dictates cancer progression in the prostate. *PLoS Biol* **1**, E59, doi:10.1371/journal.pbio.0000059 (2003).

15 Chen, Z. *et al.* Crucial role of p53-dependent cellular senescence in suppression of Pten-deficient tumorigenesis. *Nature* **436**, 725-730, doi:10.1038/nature03918 (2005).

16 Alimonti, A. *et al.* Subtle variations in Pten dose determine cancer susceptibility. *Nat Genet* **42**, 454-458, doi:10.1038/ng.556 (2010).

17 Wu, X. *et al.* Generation of a prostate epithelial cell-specific Cre transgenic mouse model for tissue-specific gene ablation. *Mech Dev* **101**, 61-69 (2001).

18 Johnson, M. T. *et al.* Inactivation of the murine pyruvate dehydrogenase (Pdha1) gene and its effect on early embryonic development. *Mol Genet Metab* **74**, 293-302, doi:10.1006/mgme.2001.3249 (2001).

19 Kaplon, J. *et al.* A key role for mitochondrial gatekeeper pyruvate dehydrogenase in oncogene-induced senescence. *Nature* **498**, 109-112, doi:10.1038/nature12154 (2013).

20 Vacanti, N. M. *et al.* Regulation of substrate utilization by the mitochondrial pyruvate carrier. *Mol Cell* **56**, 425-435, doi:10.1016/j.molcel.2014.09.024 (2014).

21 Yang, C. *et al.* Glutamine oxidation maintains the TCA cycle and cell survival during impaired mitochondrial pyruvate transport. *Mol Cell* **56**, 414-424, doi:10.1016/j.molcel.2014.09.025 (2014).

22 Rajagopalan, K. N. *et al.* Metabolic plasticity maintains proliferation in pyruvate dehydrogenase deficient cells. *Cancer Metab* **3**, 7, doi:10.1186/s40170-015-0134-4 (2015).

23 Sutendra, G. *et al.* A nuclear pyruvate dehydrogenase complex is important for the generation of acetyl-CoA and histone acetylation. *Cell* **158**, 84-97, doi:10.1016/j.cell.2014.04.046 (2014).

24 Nagaraj, R. *et al.* Nuclear Localization of Mitochondrial TCA Cycle Enzymes as a Critical Step in Mammalian Zygotic Genome Activation. *Cell* **168**, 210-223 e211, doi:10.1016/j.cell.2016.12.026 (2017).

25 Briggs, M. R., Yokoyama, C., Wang, X., Brown, M. S. & Goldstein, J. L. Nuclear protein that binds sterol regulatory element of low density lipoprotein receptor promoter. I. Identification of the protein and delineation of its target nucleotide sequence. *J Biol Chem* **268**, 14490-14496 (1993).

26 Wang, X. *et al.* Nuclear protein that binds sterol regulatory element of low density lipoprotein receptor promoter. II. Purification and characterization. *J Biol Chem* **268**, 14497-14504 (1993).

27 Porstmann, T. *et al.* SREBP activity is regulated by mTORC1 and contributes to Akt-dependent cell growth. *Cell Metab* **8**, 224-236, doi:10.1016/j.cmet.2008.07.007 (2008).

28 Han, J. *et al.* The CREB coactivator CRTC2 controls hepatic lipid metabolism by regulating SREBP1. *Nature* **524**, 243-246, doi:10.1038/nature14557 (2015).

29 Hatzivassiliou, G. *et al.* ATP citrate lyase inhibition can suppress tumor cell growth. *Cancer Cell* **8**, 311-321, doi:10.1016/j.ccr.2005.09.008 (2005).

30 Wellen, K. E. *et al.* ATP-citrate lyase links cellular metabolism to histone acetylation. *Science* **324**, 1076-1080, doi:10.1126/science.1164097 (2009).

31 Helms, M. W. *et al.* Squalene epoxidase, located on chromosome 8q24.1, is upregulated in 8q+ breast cancer and indicates poor clinical outcome in stage I and II disease. *Br J Cancer* **99**, 774-780, doi:10.1038/sj.bjc.6604556 (2008).

32 Stevenson, J., Luu, W., Kristiana, I. & Brown, A. J. Squalene mono-oxygenase, a key enzyme in cholesterol synthesis, is stabilized by unsaturated fatty acids. *Biochem J* **461**, 435-442, doi:10.1042/BJ20131404 (2014).

33 Zhao, S. *et al.* ATP-Citrate Lyase Controls a Glucose-to-Acetate Metabolic Switch. *Cell Rep* **17**, 1037-1052, doi:10.1016/j.celrep.2016.09.069 (2016).

34 Bulusu, V. *et al.* Acetate Recapturing by Nuclear Acetyl-CoA Synthetase 2 Prevents Loss of Histone Acetylation during Oxygen and Serum Limitation. *Cell Rep* **18**, 647-658, doi:10.1016/j.celrep.2016.12.055 (2017).

35 Metallo, C. M. *et al.* Reductive glutamine metabolism by IDH1 mediates lipogenesis under hypoxia. *Nature* **481**, 380-384, doi:10.1038/nature10602 (2012).

36 Mullen, A. R. *et al.* Reductive carboxylation supports growth in tumour cells with defective mitochondria. *Nature* **481**, 385-388, doi:10.1038/nature10642 (2012).

37 Currie, E., Schulze, A., Zechner, R., Walther, T. C. & Farese, R. V., Jr. Cellular fatty acid metabolism and cancer. *Cell Metab* **18**, 153-161, doi:10.1016/j.cmet.2013.05.017 (2013).

38 Aguzzi, A. & Altmeyer, M. Phase Separation: Linking Cellular Compartmentalization to Disease. *Trends Cell Biol* **26**, 547-558, doi:10.1016/j.tcb.2016.03.004 (2016).

39 Kim, J. W., Tchernyshyov, I., Semenza, G. L. & Dang, C. V. HIF-1-mediated expression of pyruvate dehydrogenase kinase: a metabolic switch required for cellular adaptation to hypoxia. *Cell Metab* **3**, 177-185, doi:10.1016/j.cmet.2006.02.002 (2006).

40 Papandreou, I., Cairns, R. A., Fontana, L., Lim, A. L. & Denko, N. C. HIF-1 mediates adaptation to hypoxia by actively downregulating mitochondrial oxygen consumption. *Cell Metab* **3**, 187-197, doi:10.1016/j.cmet.2006.01.012 (2006).

41 Dupuy, F. *et al.* PDK1-Dependent Metabolic Reprogramming Dictates Metastatic Potential in Breast Cancer. *Cell Metab* **22**, 577-589, doi:10.1016/j.cmet.2015.08.007 (2015).

42 Mager, J. & Blank, I. Synthesis of fluoropyruvic acid and some of its biological properties. *Nature* **173**, 126-127 (1954).

43 Avi-Dor, Y. & Mager, J. The effect of fluoropyruvate on the respiration of animal-tissue preparations. *Biochem J* **63**, 613-618 (1956).

44 Chari-Bitron, A. & Avi-Dor, Y. Effect of fluoropyruvate on the swelling, phosphorylative activity and respiration of guinea-pig liver mitochondria. *Biochem J* **71**, 572-578 (1959).

45 Du, J. *et al.* Inhibition of mitochondrial pyruvate transport by zaprinast causes massive accumulation of aspartate at the expense of glutamate in the retina. *J Biol Chem* **288**, 36129-36140, doi:10.1074/jbc.M113.507285 (2013).

46 Yuan, M., Breitkopf, S. B., Yang, X. & Asara, J. M. A positive/negative ion-switching, targeted mass spectrometry-based metabolomics platform for bodily fluids, cells, and fresh and fixed tissue. *Nat Protoc* **7**, 872-881, doi:10.1038/nprot.2012.024 (2012).

47 Hitosugi, T. *et al.* Tyrosine phosphorylation of mitochondrial pyruvate dehydrogenase kinase 1 is important for cancer metabolism. *Mol Cell* **44**, 864-877, doi:10.1016/j.molcel.2011.10.015 (2011).

48 Kerr, E. M., Gaude, E., Turrell, F. K., Frezza, C. & Martins, C. P. Mutant Kras copy number defines metabolic reprogramming and therapeutic susceptibilities. *Nature* **531**, 110-113, doi:10.1038/nature16967 (2016).

49 Bonnet, S. *et al.* A mitochondria-K+ channel axis is suppressed in cancer and its normalization promotes apoptosis and inhibits cancer growth. *Cancer Cell* **11**, 37-51, doi:10.1016/j.ccr.2006.10.020 (2007).

50 Vander Heiden, M. G., Cantley, L. C. & Thompson, C. B. Understanding the Warburg effect: the metabolic requirements of cell proliferation. *Science* **324**, 1029-1033, doi:10.1126/science.1160809 (2009).

51 Costello, L. C. & Franklin, R. B. Aconitase activity, citrate oxidation, and zinc inhibition in rat ventral prostate. *Enzyme* **26**, 281-287 (1981).

52 Costello, L. C., Liu, Y., Franklin, R. B. & Kennedy, M. C. Zinc inhibition of mitochondrial aconitase and its importance in citrate metabolism of prostate epithelial cells. *J Biol Chem* **272**, 28875-28881 (1997).

53 Costello, L. C., Liu, Y., Zou, J. & Franklin, R. B. The pyruvate dehydrogenase E1 alpha gene is testosterone and prolactin regulated in prostate epithelial cells. *Endocr Res* **26**, 23-39 (2000).

54 Torrano, V. *et al.* The metabolic co-regulator PGC1alpha suppresses prostate cancer metastasis. *Nat Cell Biol* **18**, 645-656, doi:10.1038/ncb3357 (2016).

Methods-only References

5 Viale, A. *et al.* Oncogene ablation-resistant pancreatic cancer cells depend on mitochondrial function. *Nature* **514**, 628-632, doi:10.1038/nature13611 (2014).

14 Trotman, L. C. *et al.* Pten dose dictates cancer progression in the prostate. *PLoS Biol* **1**, E59, doi:10.1371/journal.pbio.0000059 (2003).

15 Chen, Z. *et al.* Crucial role of p53-dependent cellular senescence in suppression of Pten-deficient tumorigenesis. *Nature* **436**, 725-730, doi:10.1038/nature03918 (2005).

16 Alimonti, A. *et al.* Subtle variations in Pten dose determine cancer susceptibility. *Nat Genet* **42**, 454-458, doi:10.1038/ng.556 (2010).

18 Johnson, M. T. *et al.* Inactivation of the murine pyruvate dehydrogenase (Pdha1) gene and its effect on early embryonic development. *Mol Genet Metab* **74**, 293-302, doi:10.1006/mgme.2001.3249 (2001).

19 Kaplon, J. *et al.* A key role for mitochondrial gatekeeper pyruvate dehydrogenase in oncogene-induced senescence. *Nature* **498**, 109-112, doi:10.1038/nature12154 (2013).

20 Vacanti, N. M. *et al.* Regulation of substrate utilization by the mitochondrial pyruvate carrier. *Mol Cell* **56**, 425-435, doi:10.1016/j.molcel.2014.09.024 (2014).

56 Subramanian, A. *et al.* Gene set enrichment analysis: a knowledge-based approach for interpreting genome-wide expression profiles. *Proc Natl Acad Sci U S A* **102**, 15545-15550, doi:10.1073/pnas.0506580102 (2005).

57 Merico, D., Isserlin, R., Stueker, O., Emili, A. & Bader, G. D. Enrichment map: a network-based method for gene-set enrichment visualization and interpretation. *PLoS One* **5**, e13984, doi:10.1371/journal.pone.0013984 (2010).

58 Delaleu, N., Nguyen, C. Q., Tekle, K. M., Jonsson, R. & Peck, A. B. Transcriptional landscapes of emerging autoimmunity: transient aberrations in the targeted tissue's extracellular milieu precede immune responses in Sjogren's syndrome. *Arthritis Res Ther* **15**, R174, doi:10.1186/ar4362 (2013).

59 Zhao, J. *et al.* TIP30 induces apoptosis under oxidative stress through stabilization of p53 messenger RNA in human hepatocellular carcinoma. *Cancer Res* **68**, 4133-4141, doi:10.1158/0008-5472.CAN-08-0432 (2008).

60 Lukacs, R. U., Goldstein, A. S., Lawson, D. A., Cheng, D. & Witte, O. N. Isolation, cultivation and characterization of adult murine prostate stem cells. *Nat Protoc* **5**, 702-713, doi:10.1038/nprot.2010.11 (2010).

61 Breitkopf, S. B. *et al.* A relative quantitative positive/negative ion switching method for untargeted lipidomics via high resolution LC-MS/MS from any biological source. *Metabolomics* **13**, doi:10.1007/s11306-016-1157-8 (2017).

Supplementary References

19 Kaplon, J. et al. A key role for mitochondrial gatekeeper pyruvate dehydrogenase in oncogene-induced senescence. Nature 498, 109-112, doi:10.1038/nature12154 (2013).

23 Sutendra, G. et al. A nuclear pyruvate dehydrogenase complex is important for the generation of acetyl-CoA and histone acetylation. Cell 158, 84-97, doi:10.1016/j.cell.2014.04.046 (2014).

30 Wellen, K. E. et al. ATP-citrate lyase links cellular metabolism to histone acetylation. Science 324, 1076-1080, doi:10.1126/science.1164097 (2009).

48 Kerr, E. M., Gaude, E., Turrell, F. K., Frezza, C. & Martins, C. P. Mutant Kras copy number defines metabolic reprogramming and therapeutic susceptibilities. Nature 531, 110-113, doi:10.1038/nature16967 (2016).

62 Carpenter, A. E. et al. CellProfiler: image analysis software for identifying and quantifying cell phenotypes. Genome Biol 7, R100, doi:10.1186/gb-2006-7-10-r100 (2006).

63 Xia, J. & Wishart, D. S. Using MetaboAnalyst 3.0 for Comprehensive Metabolomics Data Analysis. Curr Protoc Bioinformatics 55, 14 10 11-14 10 91, doi:10.1002/cpbi.11 (2016).

64 Bilyk, A., Piazza, G. J., Bistline, R. G. & Haas, M. J. Separation of Cholesterol, and Fatty Acylglycerols, Acids and Amides by Thin-Layer Chromatography. Lipids 26, 405-406, doi:Doi 10.1007/Bf02537208 (1991).

65 Ciszak, E. M., Korotchkina, L. G., Dominiak, P. M., Sidhu, S. & Patel, M. S. Structural basis for flip-flop action of thiamin pyrophosphate-dependent enzymes revealed by human pyruvate dehydrogenase. J Biol Chem 278, 21240-21246, doi:10.1074/jbc.M300339200 (2003).

66 Pei, X. Y., Titman, C. M., Frank, R. A., Leeper, F. J. & Luisi, B. F. Snapshots of catalysis in the E1 subunit of the pyruvate dehydrogenase multienzyme complex. Structure 16, 1860-1872, doi:10.1016/j.str.2008.10.009 (2008).

67 Jorgensen, W. L., Chandrasekhar, J., Madura, J. D., Impey, R. W. & Klein, L. M. Comparison of simple potential functions for simulating liquid water. J Chem Phys 79, 926-935 (1983).

68 Maier, J. A. et al. ff14SB: Improving the Accuracy of Protein Side Chain and Backbone Parameters from ff99SB. Journal of Chemical Theory and Computation, doi:10.1021/acs.jctc.5b00255 (2015).

69 Wang, J., Wolf, R. M., Caldwell, J. W., Kollman, P. A. & Case, D. A. Development and testing of a general amber force field. J Comput Chem 25, 1157-1174 (2004).

70 Joung, I. S. & Cheatham, T. E., 3rd. Determination of alkali and halide monovalent ion parameters for use in explicitly solvated biomolecular simulations. J Phys Chem B 112, 9020-9041, doi:10.1021/jp8001614 (2008).

71 Li, P. & Merz, K. M. Taking into Account the Ion-Induced Dipole Interaction in the Nonbonded Model of Ions. Journal of Chemical Theory and Computation 10, 289-297, doi:10.1021/ct400751u (2014).

72 Essmann, U. et al. A smooth particle mesh Ewald method. The Journal of Chemical Physics 103, 8577-8593 (1995).

73 Le Grand, S., Götz, A. W. & Walker, R. C. SPFP: Speed without compromise—A mixed precision model for GPU accelerated molecular dynamics simulations. Computer Physics Communications 184, 374-380, doi:http://dx.doi.org/10.1016/j.cpc.2012.09.022 (2013).

74 Miller, B. R. et al. MMPBSA.py: An Efficient Program for End-State Free Energy Calculations. Journal of Chemical Theory and Computation 8, 3314-3321, doi:10.1021/ct300418h (2012).

75 Hawkins, G. D., Cramer, C. J. & Truhlar, D. G. Parametrized Models of Aqueous Free Energies of Solvation Based on Pairwise Descreening of Solute Atomic Charges from a Dielectric Medium. The Journal of Physical Chemistry 100, 19824-19839, doi:10.1021/jp961710n (1996).

76 Connolly, M. Analytical molecular surface calculation. Journal of Applied Crystallography 16, 548-558, doi:doi:10.1107/S0021889883010985 (1983).